Superradiance and its Decoherence due to Long-Range Rydberg Atom Pair-Interactions

Dissertation

der Mathematisch-Naturwissenschaftlichen Fakultät
der Eberhard Karls Universität Tübingen
zur Erlangung des Grades eines
Doktors der Naturwissenschaften
(Dr. rer. nat.)

vorgelegt von
Elmer Suarez
aus Lima, Peru

Tübingen
2023

Gedruckt mit Genehmigung der Mathematisch-Naturwissenschaftlichen Fakultät der Eberhard Karls Universität Tübingen.

Tag der mündlichen Qualifikation:	17.05.2023
Dekan:	Prof. Dr. Thilo Stehle
1. Berichterstatter:	apl. Prof. Dr. Sebastian Slama
2. Berichterstatter:	Prof. Dr. Claus Zimmermann

Abstract

This work reports on the real-time detection of internal-state dynamics of cold ^{87}Rb atoms being excited to the $30D_{5/2}$ Rydberg state via two-photon excitation. A mesoscopic cloud of atoms is overlapped with the mode volume of a confocal optical cavity and optically pumped by two laser beams transverse to the cavity axis. The excitation to Rydberg states changes the collective atom-cavity coupling, which is detected by monitoring the light transmitted through the cavity while being weakly driven. In addition to the damped coherent excitation dynamics and the decay back to the ground state, the data shows a superradiant enhancement of the black-body radiation induced transitions from the $30D_{5/2}$ state to neighboring Rydberg states. Furthermore, they show a density dependent mitigation of the superradiant decay which is attributed to long range dipole-dipole interactions between atoms in the involved Rydberg states. These results contribute to solving a recent controversy on the interplay between BBR-induced superradiance and Rydberg atom interactions.

Zusammenfassung

In dieser Arbeit wird über die Echtzeitdetektion der internen Zustandsdynamik von kalten ^{87}Rb-Atomen berichtet, die durch Zwei-Photonen-Anregung zum $30D_{5/2}$-Rydberg-Zustand angeregt werden. Eine mesoskopische Atomwolke wird mit dem Modenvolumen eines konfokalen optischen Resonators überlagert und durch zwei Laserstrahlen quer zur Resonatorachse optisch gepumpt. Die Anregung in Rydberg-Zustände verändert die kollektive Atom-Resonator-Kopplung, die durch Beobachtung des durch den Resonator transmittierten Lichts nachgewiesen wird. Neben der gedämpften kohärenten Anregungsdynamik und dem Zerfall zurück in den Grundzustand zeigen die Daten eine superradiante Verstärkung der durch die Schwarzkörperstrahlung induzierten Übergänge vom $30D_{5/2}$-Zustand in benachbarte Rydberg-Zustände. Darüber hinaus zeigen sie eine dichteabhängige Abschwächung des superradianten Zerfalls, die auf langreichweitige Dipol-Dipol-Wechselwirkungen zwischen den Atomen in den beteiligten Rydberg-Zuständen zurückgeführt wird. Diese Ergebnisse tragen zur Lösung einer aktuellen Kontroverse über das Zusammenspiel zwischen BBR-induzierter Superradianz und Rydberg-Atom-Wechselwirkungen bei.

Contents

1. Introduction

Quoting Richard Feynman: nature has, at the atomic scale, "a peculiar behavior impossible to explain in any classical way." [1] Consequently, quantum theory complements classical physics by giving a physical system the ability to form a new kind of state: one where different possible states coexist through interference, like waves on a pond. Now, how can one experience the quantum realm? The idea that measuring a system brings it back to our classical experience is the main concept behind decoherence [2]. Take for instance the tracks left behind by a particle on a cloud chamber: the constant measurement of its position by collisions to other environmental particles allows us, in a sense, to observe the particles trajectories.

In fact, the avenue of quantum theory into physics finally fueled the technological development from which our modern technology is built upon. At present, the development of quantum technologies, that is, the exploitation of this "peculiar behavior" as a resource is thriving. In fact, the most recent Nobel prize has been awarded to A. Aspect, J. F. Clauser and A. Zeilinger for studying entangled states on their connection to classical experience and their introduction to quantum information. In addition, a key step towards state of the art quantum technologies was the control of quantum systems. At the front page of this achievement are Serge Haroche and David Wineland as they were both awarded the Nobel prize in 2012. While Wineland studied the interaction between two degrees of freedom (i.e. internal states and motion) of single ions in a harmonic trap [3], Haroche focused on the interaction between single atoms and photons inside a cavity or resonator: cavity QED [4]. In particular, the latter used atoms with high principal quantum number (circular Rydberg states) as they are extremely sensitive to microwave radiation which is, in turn, contained inside a cavity.

The quantized nature of an atom or of electromagnetic radiation was demonstrated in both cases. Remarkably, a superposition of coherent or Glauber states was engineered in order to show the creation of a Schrödinger cat state. The role of

the cat as macroscopic object was played by the coherent state: a particular superposition of the infinite photon number states which exhibits classical trajectories in phase space. Then, the wave character, i.e. the ability for a macroscopic state to exist in a superposition was observed to dissapear over time in a process known as decoherence. In a sense, Wineland and Haroche were exploring the border between classical and quantum physics.

In parallel to these achievements, decoherence has a story on its own and it has found a place in all areas of quantum theory. Because it describes the loss of quantumness on a system, the study of decoherence is of technological importance for areas such as quantum information processing [5]. At the same time, since decoherence deals with the concept of measurement (i.e. the channel of communication with the quantum realm) it rises questions about the interpretation of quantum mechanics [6]. Even though the study of decoherence has a strong theoretical character there are a number of experiments which have helped to understand the nature of this process [7]. In particular, the work done by Sonnentag and Hasselbach [8] from the university of Tübingen has explored the action of decoherence on interfering electrons. It is indeed in Tübingen that electron diffraction was pioneered by Jönsson [9]. In addition, the work with electron interferometers was continued by Stibor [10, 11].

Early on their research about microwave cavities and Rydberg atoms, the Paris group led by Haroche explored the spontaneous decay of initially excited atoms inside the cavity. By observing atom number statistics they revealed a shorter emission time from the upper Rydberg state than expected for a single atom; thus, demonstrating the first observation of superradiant decay [12, 13]. Superradiance was predicted by Dicke years before [14] and further studied by Bonifacio [15]. Nevertheless, in contrast to Dicke's original proposal, in those experiments it is the emission rate of thermal photons (black body radiation) and not the spontaneous decay rate that was enhanced. Still in the microwave domain, superradiance has been observed in other atom-like systems such as semiconductors [16], color centers in diamond [17], vibrational transitions in molecules [18] and has even been proposed in astrophysics [19].

Importantly, inside a cavity, superradiance has shown to be of technological importance. Indeed, in order to achieve greater accuracy on the ticking rate of atomic clocks, lasers with very small uncertainty on their frequency are required. This is

because atoms used for this matter have states with linewidths on the order of mHz (e.g. 1 mHz for ^{87}Sr). Recently, in [20], a superradiant laser was demonstrated: light is taken from ^{87}Sr and a useful brightness is reached by superradiant enhancement of the spontaneous decay into the cavity. Furthermore, this is possible when the system is in the so-called bad cavity regime where the cavity leaks out photons much faster than the energy exchange rate with the atoms. Consequently, the cavity frequency does not play a key role meaning that the effects of typical noise sources of conventional lasers are highly supressed. However, there is still one enemy to fight: decoherence.

Superradiance is the result of constructive interference between a collection of synchronized or phase-correlated scatterers. As such, any type of environment that is inhomogeneously coupled to the ensemble will be a dephasing or decoherence source. Diffusion of the momentum state (i.e. heating) has been recognized to reduce or even completely suppress superradiance. For a thermal atomic cloud, this effect is observed due to Doppler broadening [21, 22]; however, subradiance (the decay into long-lived many-body states) shows the opposite effect on thermal dephasing [23]. In addition, similar effects are observed for a BEC inside an optical ring cavity [24]. Finally, in a circuit QED context, the different atomic positions relative to the resonator makes their coupling to be position dependent. This inhomogeneous coupling reduces the superradiant decay rate but also increases it under certain conditions [25].

Another decoherence source of particular importance to this thesis is due to dipole-dipole interactions. This type of interaction is described by a Hamiltonian $\hat{\mathcal{H}}_{\mathrm{dd}} = \sum_{j,j'}^{N} \Omega_{jj'} \hat{\sigma}_j^{\dagger} \hat{\sigma}_{j'}$ between two atoms j and j' which can be translated as the exchange of a virtual photon by a pair of atoms. The potential energy $\Omega_{jj'}$ of this interaction depends on the interatomic distance and is greater the smaller the ratio is between this distance and the transition wavelength. The negative effect of this type of interaction on superradiance has been recognized since the early experiments by the Paris group [26]. However, it has been only until recently that numerical simulations have been able to describe superradiance in an ensemble of interacting atoms [27]. On the other hand, experiments with ultracold atomic clouds show unclear results: whereas in [28] evidence is shown of an atomic lifetime reduction argued to be due to superradiance, in [29] no superradiant decay rate is observed under similar experimental conditions. It is the objective of this work to contribute on this debate.

In this regard, one must recognize that the large dipole moment of atoms excited to Rydberg states also facilitates the energy exchange between an atom pair on the micrometer scale. For this, since the usually achieved atomic densities in magneto-optical traps are on the order of $10^9 - 10^{11}$ cm^{-3} they are a suitable platform to study dipole-dipole interactions between Rydberg atoms. Furthermore, since the transition wavelength between Rydberg states is in the order of a few milimeters, the condition for superradiance can also be fulfilled.

This thesis starts by introducing the theoretical background from which the physical concepts most important for this work lie upon: First, in chapter 2 the optical Bloch equations necessary to describe the interaction of light with two and three level atoms are shown when both classical and quantum (cavity QED) fields are present. The steady-state solutions for the atomic variables as well as the intracavity field (i.e. cavity transmission) are then presented under the low saturation approximation. In particular, for a three-level atom, special attention is payed to electromagnetically induced transparency (EIT), a coherent phenomena where an atom becomes transparent with the aid of an extra powerful laser. At the end of this chapter the collective coupling of an atomic ensemble to the same electromagnetic modes is explained to be the cause of superradiant decay and dipole-dipole interaction. The shape factor or cooperativity parameter that gauges superradiance for an extended ensemble is also introduced. Chapter 3 is dedicated to atoms in Rydberg states: how their decay into several other states is described including their interaction with black body radiation. Finally, dipole-dipole interactions are introduced in the context of Rydberg states and, in particular, the model used to describe the decoherence of superradiance is explained. In chapter 4 all optical setups are described together with the measurements that show how superradiance is diminished as Rydberg density is increased. In addition, the observation of optical pumping due to the intracavity field in the cavity transmission is explained. In appendix A the Bloch equations are extended to include the multilevel structure due to the Zeemann states in order to describe our observations.

2. Atom-Light Interaction

All physical effects to be studied in this thesis orbit around the interaction between matter (in the form of individual, ultracold atoms) and light. The present chapter starts describing the atom as effectively consisting of only two energy states which can be treated as a dipole. The interaction between this dipole and the electromagnetic field is then introduced in a semiclassical context. When a third level is included the complexity of the problem is increased. However, approximations are justified in order to reveal the physical effects most relevant for this thesis like two-photon excitation and Electromagnetically Induced Transparency. Furthermore, the interaction between an optical cavity and an atomic ensemble is studied using the mean-field approximation where quantum correlations between atoms and cavity photons are neglected. The mean-field equations for the atom-cavity system are used to arrive to an expression of the cavity transmission that is then used for the different experimental conditions of this thesis. Finally, superradiance, a collective effect where atoms that are very close to each other radiate at a much faster rate than when they are far apart is introduced.

2.1. Interaction of light with a Two-Level Atom

It is known that any atom, even Hydrogen, exhibits a complex energy structure. In fact, an atom internal energy structure consists of an infinite number of discrete values which get closer the more they approach the ionization energy. However, it is customary to consider only two energy states. This is specially done when describing an atom interacting with light that is monochromatic and has a frequency ω such that $\hbar\omega$ is nearly equal to the energy difference between both states considered [30, 31].

Following this argument and neglecting atomic motion, the quantum states $|g\rangle$ and $|e\rangle$ are defined as eigenstates of the atomic Hamiltonian $\hat{\mathcal{H}}_a$ with eigenvalues E_g

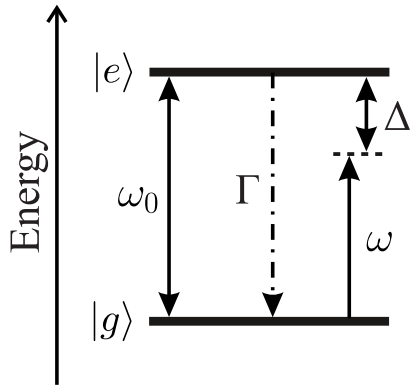

Figure 2.1.: Energy scheme (with $\hbar = 1$) of a two-level atom with "ground" and "excited" state labeled $|g\rangle$ and $|e\rangle$, respectively. The excited state spontaneously decays with a rate Γ to the ground state. The atom is driven by a light field of frequency ω, with a detuning $\Delta = \omega - \omega_0$ such that ω_0 is the frequency corresponding to the energy difference between the states: $E_e - E_g = \hbar\omega_0$.

and E_e such that $E_e - E_g = \hbar\omega_0$. This allows to define the eigenvalues relative to some arbitrary energy E_0: choosing $E_0 = (E_g + E_e)/2$ results in $E_{e,g} = E_0 \pm \frac{1}{2}\hbar\omega_0$. On the other hand, the set $\{|e\rangle, |g\rangle\}$ is defined as the orthonormal basis of the Hilbert space used to describe the two-level atom. Consequently, the common term E_0 only adds to $\hat{\mathcal{H}}_a$ an extra term proportional to the unity operator ($E_0\mathbb{1}$). This means that E_0 can be ignored as it does not influence the atom dynamics (see eq. (2.20)). $\hat{\mathcal{H}}_a$ can then be defined such that

$$\hat{\mathcal{H}}_a |e\rangle = \frac{1}{2}\hbar\omega_0 |e\rangle \tag{2.1}$$

and

$$\hat{\mathcal{H}}_a |g\rangle = -\frac{1}{2}\hbar\omega_0 |g\rangle . \tag{2.2}$$

Under the dipole approximation [31], the interaction Hamiltonian is

$$\hat{\mathcal{H}}_{int} = -\hat{\mathbf{d}} \cdot \mathcal{E}. \tag{2.3}$$

Where $\hat{\mathbf{d}}$ is the atomic dipole moment operator and $\mathcal{E}$ is the electric field vector evaluated at the dipole's position. Since $\hat{\mathbf{d}} = e\hat{\mathbf{r}}$ where e is the electron's charge and $\hat{\mathbf{r}}$ is the position operator, the dipole operator has odd parity. Therefore, its matrix

form will have null diagonal elements (expectation values) whereas its non-diagonal elements will be denoted as

$$\mathbf{d}_{ge} = \langle g| \hat{\mathbf{d}} |e\rangle \qquad\qquad \mathbf{d}_{eg} = \mathbf{d}^*_{ge} = \langle e| \hat{\mathbf{d}} |g\rangle . \tag{2.4}$$

The complex vector $\mathbf{d}_{ge}$ can then be calculated by expanding $\hat{\mathbf{r}}$:

$$\mathbf{d}_{ge} = e \int \Psi^*_g(\mathbf{r}) \mathbf{r} \Psi_e(\mathbf{r})\, d^3r. \tag{2.5}$$

Here, $\Psi_g(\mathbf{r}) = \langle r|g\rangle$ and $\Psi_e(\mathbf{r}) = \langle r|e\rangle$ are the wavefunctions of the ground and excited states; respectively.

By further defining the ladder operators $\hat{\sigma}^+ = |e\rangle\langle g|$ and $\hat{\sigma}^- = |g\rangle\langle e|$, the dipole operator can be written as

$$\hat{\mathbf{d}} = \mathbf{d}_{ge}\hat{\sigma}^- + \mathbf{d}_{eg}\hat{\sigma}^+. \tag{2.6}$$

Alternatively, the introduction of the Pauli operators

$$\hat{\sigma}_x \equiv \begin{pmatrix} 0 & 1 \\ 1 & 0 \end{pmatrix} \qquad \hat{\sigma}_y \equiv \begin{pmatrix} 0 & -i \\ i & 0 \end{pmatrix} \qquad \hat{\sigma}_z \equiv \begin{pmatrix} 1 & 0 \\ 0 & -1 \end{pmatrix} \tag{2.7}$$

results in $\hat{\sigma}^\pm = (\hat{\sigma}_x \pm i\hat{\sigma}_y)/2$. Consequently, the dipole operator $\hat{\mathbf{d}}$ and the atomic Hamiltonian $\hat{\mathcal{H}}_a$ can be written as

$$\hat{\mathbf{d}} = \mathrm{Re}(\mathbf{d}_{ge})\hat{\sigma}_x + \mathrm{Im}(\mathbf{d}_{ge})\hat{\sigma}_y, \tag{2.8}$$

and

$$\hat{\mathcal{H}}_a = \frac{1}{2}\hbar\omega_0\hat{\sigma}_z. \tag{2.9}$$

On the other hand, inserting the electric field $\mathcal{E} = \left(\boldsymbol{\mathcal{E}_0} e^{i\omega t} + \boldsymbol{\mathcal{E}_0} e^{-i\omega t}\right)/2$ into eq. (2.3) and using eq. (2.6) results in

$$\hat{\mathcal{H}}_{int} = \frac{\Omega}{2}\hat{\sigma}^- e^{-i\omega t} + \frac{\Omega^*}{2}\hat{\sigma}^+ e^{i\omega t} + \frac{\Omega}{2}\hat{\sigma}^- e^{i\omega t} + \frac{\Omega^*}{2}\hat{\sigma}^+ e^{-i\omega t}. \tag{2.10}$$

Where $\Omega = -\mathbf{d}_{ge} \cdot \boldsymbol{\mathcal{E}_0}$ is the so called Rabi frequency. At this point, it is customary to perform the Rotating Wave Approximation (RWA). It consists in eliminating the fast oscillating terms after changing the frame of reference to one rotating at the

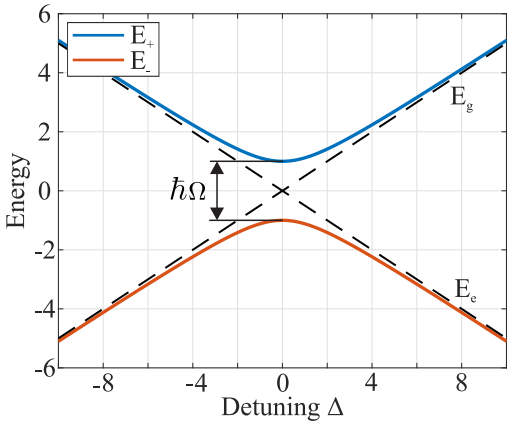

Figure 2.2.: Eigenvalues of a two-level atom driven by a light field with Rabi frequency $\Omega = 2$ as a function of detuning $\Delta = \omega - \omega_0$. The avoided crossing is manifested by the minimum separation Ω between the eigenvalues $E_\pm$. In comparison, the free atom eigenvalues $E_{g,e}$ (dashed lines) cross at $\Delta = 0$. In the dispersive regime ($\Delta \gg \Omega$), $E_{g,e}$ and $E_\pm$ almost coincide; the difference being given by the Stark shift.

laser frequency which results in

$$\hat{\mathcal{H}}_{int} = \frac{\Omega}{2}\hat{\sigma}^- + \frac{\Omega^*}{2}\hat{\sigma}^+. \tag{2.11}$$

Finally the full Hamiltonian reads

$$\hat{\mathcal{H}} = \hat{\mathcal{H}}_a + \hat{\mathcal{H}}_{int} = -\frac{1}{2}\hbar\Delta\hat{\sigma}_z + \frac{\hbar}{2}(\Omega\hat{\sigma}^- + \Omega^*\hat{\sigma}^+). \tag{2.12}$$

Where $\Delta = \omega - \omega_0$ is the detuning of the laser frequency relative to the atomic transition frequency.

The atomic energies are modified by the interaction with the light field. This is manifested by the eigenvalues of Eq. (2.12):

$$E_\pm = \pm\frac{\hbar}{2}\sqrt{|\Omega|^2 + \Delta^2}. \tag{2.13}$$

Turning off the interaction ($\Omega = 0$) gives the atomic energies in the rotating frame: $E_e = -\frac{\hbar}{2}\Delta$ and $E_g = \frac{\hbar}{2}\Delta$. The modified energies are plotted in Fig. 2.2 as a function of Δ. They show what is called an avoided crossing, in comparison to the free atomic

energies (dashed lines) which intersect at the origin. In the dispersive regime, when $\Omega \ll \Delta$, the frequency shift induced by the light field equals

$$E_{\pm} - E_{g,e} = \pm\hbar\frac{|\Omega|^2}{4\Delta} \tag{2.14}$$

which is the AC Stark shift for a two-level atom. On the other hand, the eigenstates can be written as function of a mixing angle θ such that $\tan(\theta) = |\Omega|/\Delta$:

$$|D_+\rangle = \cos(\theta/2)\,|e\rangle + \sin(\theta/2)\,|g\rangle \tag{2.15}$$

$$|D_-\rangle = -\sin(\theta/2)\,|e\rangle + \cos(\theta/2)\,|g\rangle\,. \tag{2.16}$$

2.1.1. Bloch Equations

In the present thesis it is convenient to describe the atomic system with a density operator $\hat{\rho}$. This operator is defined such that [32]:

$$\hat{\rho}^\dagger = \hat{\rho} \qquad\qquad \hat{\rho} \geq 0 \qquad\qquad \mathrm{Tr}\,(\hat{\rho}) = 1. \tag{2.17}$$

As a consequence, for a two-level atom, the corresponding density matrix

$$\hat{\rho} \equiv \begin{pmatrix} \rho_{ee} & \rho_{eg} \\ \rho_{ge} & \rho_{gg} \end{pmatrix} \tag{2.18}$$

has its elements $\rho_{ij} = \mathrm{Tr}\,(\hat{\rho}\,|j\rangle\langle i|)$ (with $i,\, j = e,\, g$) constrained by

$$\rho_{ge} = \rho_{eg}^* \qquad\qquad \rho_{ee},\, \rho_{gg} \geq 0 \qquad\qquad \rho_{ee} + \rho_{gg} = 1. \tag{2.19}$$

In particular, ρ_{ee} and ρ_{gg} are termed populations as they represent the probability for the atom to be in state $|e\rangle$ or $|g\rangle$, respectively. On the other hand, ρ_{eg} and ρ_{ge} are termed coherences.

The Hamiltonian of eq. (2.12) changes the atomic system following the Von Neumann equation:

$$\frac{d\hat{\rho}}{dt} = -i\left[\hat{\mathcal{H}}/\hbar,\, \hat{\rho}\right]. \tag{2.20}$$

It can be seen that the role of $\hbar$ is to scale the time evolution of $\hat{\rho}$; thus, from now on, $\hbar = 1$ is assumed for convenience. It is also remarked that the interaction of

an atom to its environment or a reservoir (e.g. quantum electromagnetic vacuum, photon bath) is not included in eq. (2.20).

The modification of the Von Neumann equation to account for a reservoir is not trivial [32]. However, in the present thesis, it is well justified to consider the master equation

$$\frac{d\hat{\rho}}{dt} = -i\left[\hat{H},\,\hat{\rho}\right] + \sum_k \gamma_k \left(\hat{\mathrm{L}}_k \hat{\rho} \hat{\mathrm{L}}_k^\dagger - \frac{1}{2}\left\{\hat{\mathrm{L}}_k^\dagger \hat{\mathrm{L}}_k,\,\hat{\rho}\right\}\right) \tag{2.21}$$

as the one governing the time dynamics of $\hat{\rho}$ including the coupling of the atom to its environment [1]. The most notable change is the last term (usually denoted as $\mathcal{D}\left[\hat{\rho}\right]$) called dissipator or Lindblad superoperator which describes irreversible lost of energy (or information [33]) into the environment. Here, it has been written in the standard diagonal Lindblad form with jump or Lindblad operators $\hat{\mathrm{L}}_k$ and their corresponding eigenvalues γ_k.

Spontaneous decay is a consequence of the interaction of the atom with the electromagnetic quantum vacuum modes. In this case, only the dissipator has to be added which is, in turn, described by a single eigenvalue $\gamma_1 = \Gamma$ and Lindblad operator $\hat{\mathrm{L}}_1 = \hat{\sigma}^-$:

$$\frac{d\hat{\rho}}{dt} = -i\left[\hat{\mathcal{H}},\,\hat{\rho}\right] + \Gamma\left(\hat{\sigma}^-\hat{\rho}\hat{\sigma}^+ - \frac{1}{2}\left\{\hat{\sigma}^+\hat{\sigma}^-,\,\hat{\rho}\right\}\right). \tag{2.22}$$

Furthermore, the spontaneous decay rate Γ is given by

$$\Gamma = \frac{1}{\tau} = 2\pi\mathrm{FWHM} = \frac{\omega_0^3 \left|\mathbf{d}_{ge}\right|^2}{3\pi\epsilon_0\hbar c^3}. \tag{2.23}$$

Where τ and FWHM are the lifetime and the Full Width at Half Maximum of the excited state, respectively.

After some algebra, using $\dot{\rho}_{ij} = \mathrm{Tr}\left(\dot{\hat{\rho}}\left|j\right\rangle\!\left\langle i\right|\right)$, the optical Bloch equations (OBE)

[1] In the Heisenberg picture, eq. 2.21 is slightly modified to describe the time evolution of some operator $\hat{A}$ [32]:

$$\frac{d\hat{A}}{dt} = i\left[\hat{H},\,\hat{A}\right] + \sum_k \gamma_k \left(\hat{\mathrm{L}}_k^\dagger \hat{A} \hat{\mathrm{L}}_k - \frac{1}{2}\left\{\hat{\mathrm{L}}_k^\dagger \hat{\mathrm{L}}_k,\,\hat{A}\right\}\right)$$

are derived from eq. (2.22):

$$\dot{\rho}_{ee} = -\gamma_{\parallel}\rho_{ee} - i\frac{\Omega}{2}(\rho_{ge} - \rho_{eg}) \tag{2.24}$$

$$\dot{\rho}_{gg} = \gamma_{\parallel}\rho_{ee} + i\frac{\Omega}{2}(\rho_{ge} - \rho_{eg}) \tag{2.25}$$

$$\dot{\rho}_{eg} = -(\gamma_{\perp} - i\Delta)\rho_{eg} + i\frac{\Omega}{2}(\rho_{ee} - \rho_{gg}) \tag{2.26}$$

$$\dot{\rho}_{ge} = -(\gamma_{\perp} + i\Delta)\rho_{ge} - i\frac{\Omega}{2}(\rho_{ee} - \rho_{gg}). \tag{2.27}$$

There, it has been assumed that Ω is real. Also, notation makes explicit that the decay rate of the coherences ($\gamma_{\perp}$) and the populations ($\gamma_{\parallel}$) are different. This distinction becomes more important when, for example, homogeneous broadening must be included[2]. However, when spontaneous decay is the only source of decoherence (as in eq. 2.22): $\gamma_{\perp} = \Gamma/2$ and $\gamma_{\parallel} = \Gamma$.

For the present work, the steady-state solution ($\dot{\rho}_{ij} = 0$) of the OBE is more important than the time-dependence. Then, the relevant equations are

$$\rho_{ee}^{\mathrm{ss}} = \frac{s_0/2}{1 + s_0 + (\Delta/\gamma_{\perp})^2} \tag{2.28}$$

$$\rho_{eg}^{\mathrm{ss}} = \frac{\Omega/2\gamma_{\perp}}{1 + s_0 + (\Delta/\gamma_{\perp})^2}\left(-i + \Delta/\gamma_{\perp}\right), \tag{2.29}$$

where the on-resonance saturation parameter $s_0 = \Omega^2/\gamma_{\perp}\gamma_{\parallel} = 2\Omega^2/\Gamma^2$ is introduced. Fig. 2.3a shows the behavior of ρ_{ee}^{ss}: the atom is more likely to be in the excited state as s_0 is increased until the saturation limit ($\rho_{ee}^{\mathrm{ss}} = 0.5$ at $s_0 \to \infty$) is asymptotically reached. However, the excitation efficiency is reduced for any s_0 as Δ goes away from 0.

Equally important for this work are the dispersive and absorptive characteristics of a two-level atomic medium of density ζ. These are calculated from the real and imaginary parts of the refractive index $\eta = k/k_0 = \sqrt{1+\chi}$ [34]. The complex susceptibility χ is obtained following the classical definition of the dipole moment together with eq. (2.6). Assuming a complex dipole moment $\mathbf{p}$ such that $\mathbf{d} =$

[2]This type of broadening could be included into eq. (2.22) by considering an extra Lindblad operator $\mathrm{L}_2 = |e\rangle\langle e|$ with eigenvalue $\gamma_2 = \gamma_d$. As a result, the coherences decay at a rate $\gamma_{\perp} = (\Gamma + \gamma_d)/2$.

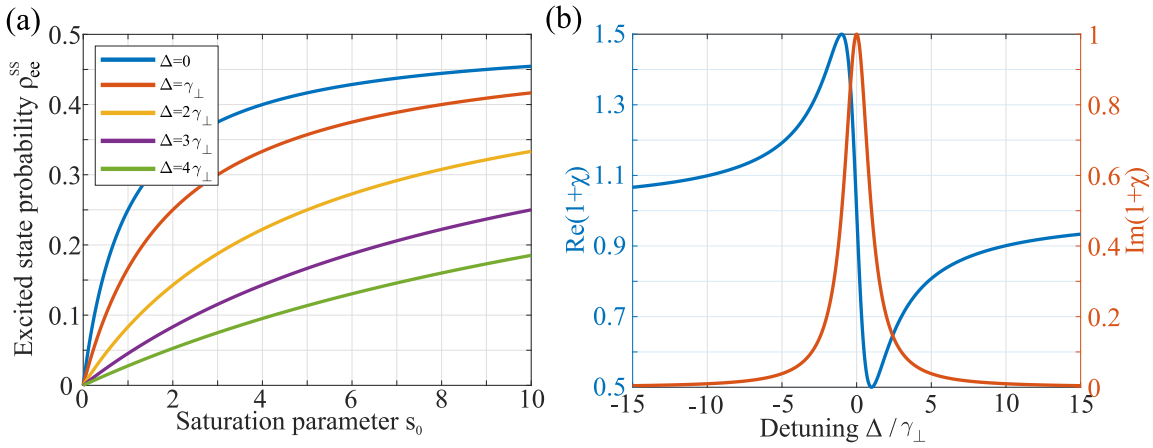

Figure 2.3.: (a) Excitation probability for a two-level atom as a function of the saturation parameter s_0. For $s_0 \lll 1$ the excitation probability is linear with respect to s_0 and the proportionality constant follows a Lorentzian profile dependent on $\Delta/\gamma_\perp$. (b) Real (dispersive) and imaginary (absorptive) parts of the dielectric constant for a two-level atom. Anomalous dispersion occurs for detunings within the FWHM, where absorption is greatest.

$\mathrm{Tr}\left(\hat{\rho}\hat{\mathbf{d}}\right) = \mathbf{p} + \mathbf{p}^*$, we thus have $\zeta\mathbf{p} = -\frac{1}{2}\epsilon_0\chi\boldsymbol{\mathcal{E}_0}$ [35]. Therefore, in steady-state, one finally obtains

$$\chi = -\frac{3\pi\zeta}{k^3}\frac{\gamma_\parallel/\gamma_\perp}{1+s_0+(\Delta/\gamma_\perp)^2}(-i+\Delta/\gamma_\perp). \tag{2.30}$$

This can be further simplified by considering $2\gamma_\perp = \gamma_\parallel = \Gamma$, eq. 2.23 and assuming $\Omega \ll \gamma_\parallel, \gamma_\perp$:

$$\chi = \frac{6\pi\zeta}{k^3}\frac{i}{1-i2\Delta/\Gamma}. \tag{2.31}$$

The adimensional prefactor $6\pi\zeta/k^3$ is a gauge for the density of the atomic medium. When small (< 1), one can approximate $\eta \approx 1 + \chi/2$. Consequently, the intensity absorption coefficient is given by $\alpha = k_0\mathrm{Im}(\chi)$ and the dispersion coefficient is given by $\beta = k_0\mathrm{Re}(\chi/2)$ [35]. In fig. 2.3b the real and imaginary parts of the dielectric constant $1+\chi$, for unity prefactor, are plotted as a function of detuning. Note how the absorption of the atom is greater within the FWHM, when anomalous dispersion occurs.

The absorption of a two-level atomic medium as a function of Δ follows a Lorentzian lineshape. Indeed, at low saturation, the imaginary component of the refractive in-

dex reduces the field intensity as $I(z) \propto e^{-\alpha z}$ where α was introduced above and z is the propagation coordinate. Then, the fraction of transmitted light (i.e. the transmission) through an atomic medium of width ℓ is given by $T_\ell = e^{-\alpha\ell}$ which at first order on α can be linearized as

$$T_\ell \sim 1 - \alpha\ell = 1 - \frac{6\pi\zeta\ell}{k^2}\frac{1}{1+(2\Delta/\Gamma)^2}. \tag{2.32}$$

The FWHM is then given by the spontaneous decay rate Γ. Furthermore, at resonance, the optical density is defined as $OD = \sigma_0\zeta\ell$ where $\sigma_0 = 6\pi/k^2$ is the resonant cross section.

2.2. Interaction of light with a three-level atom

Adding a third level to the system leads to the three different possible energy schemes shown in Fig. 2.4(a). In this thesis, however, the ladder type system is used: the frequencies $\omega_{ge} = E_e - E_g$ and $\omega_{er} = E_r - E_e$ correspond to the lower and upper transition, respectively. At the same time, the Hilbert space basis is extended to $\{|e\rangle, |g\rangle, |r\rangle\}$; then, by choosing the energy reference $E_0 = E_g$, the atomic Hamiltonian $\hat{\mathcal{H}}_a$ is defined such that

$$\hat{\mathcal{H}}_a |e\rangle = \omega_{ge} |e\rangle, \tag{2.33}$$

$$\hat{\mathcal{H}}_a |r\rangle = (\omega_{ge} + \omega_{er}) |r\rangle \tag{2.34}$$

and

$$\hat{\mathcal{H}}_a |g\rangle = 0. \tag{2.35}$$

As shown in Fig. 2.4(b), each atomic transition is nearly resonant to a light field of frequency $\omega_{1,2}$. The interaction Hamiltonian is then given by

$$\hat{\mathcal{H}}_{int} = -\hat{\mathbf{d}}_{ge} \cdot \boldsymbol{\mathcal{E}}_\mathbf{1} - \hat{\mathbf{d}}_{er} \cdot \boldsymbol{\mathcal{E}}_\mathbf{2} \tag{2.36}$$

where $\hat{\mathbf{d}}_{ge}$ and $\hat{\mathbf{d}}_{er}$ are the dipole operators for the lower and upper transition, respectively. By introducing the ladder operators for each atomic transition (i.e. $\hat{\sigma}_1^{\pm}$ and $\hat{\sigma}_2^{\pm}$), the RWA is applied after changing the reference frame with the unitary operator $U = e^{i\omega_1 t} |e\rangle\langle e| + |g\rangle\langle g| + e^{i(\omega_1+\omega_2)t} |r\rangle\langle r|$. Then, the Hamiltonian $\hat{\mathcal{H}}_{int}$ is

written as

$$\hat{\mathcal{H}}_{int} = \frac{\Omega_1}{2}\hat{\sigma}_1^- e^{-i\omega_1 t} + \frac{\Omega_1^*}{2}\hat{\sigma}_1^+ e^{i\omega_1 t} + \frac{\Omega_2}{2}\hat{\sigma}_2^- e^{-i\omega_2 t} + \frac{\Omega_2^*}{2}\hat{\sigma}_2^+ e^{i\omega_2 t} \tag{2.37}$$

with corresponding Rabi frequencies $\Omega_1 = -\mathbf{d}_{ge} \cdot \mathcal{E}_1$ and $\Omega_2 = -\mathbf{d}_{er} \cdot \mathcal{E}_2$. Finally, the total Hamiltonian $\hat{\mathcal{H}}$ reads

$$\hat{\mathcal{H}} = \hat{\mathcal{H}}_a + \hat{\mathcal{H}}_{int} = -\delta_1 \left|e\right\rangle\!\left\langle e\right| - \delta \left|r\right\rangle\!\left\langle r\right| + \frac{\Omega_1}{2}(\hat{\sigma}_1^+ + \hat{\sigma}_1^-) + \frac{\Omega_2}{2}(\hat{\sigma}_2^+ + \hat{\sigma}_2^-). \tag{2.38}$$

Here, $\Omega_{1,2}$ is assumed real and the two-photon detuning $\delta = \delta_1 + \delta_2 = (\omega_1 - \omega_{ge}) + (\omega_2 - \omega_{er})$ is introduced.

The intermediate ($|e\rangle$) and upper ($|r\rangle$) state spontaneously decay at rates Γ_e and Γ_r. Furthermore, it is assumed that homogeneous broadening, accounted for by the decoherence rate γ_d, only affects the upper state. Therefore, following Eqs. (2.21) and (2.38), the OBE are derived:

$$\dot{\rho}_{ee} = -\Gamma_e\rho_{ee} + \Gamma_r\rho_{rr} - \Omega_1\mathrm{Im}(\rho_{eg}) + \Omega_2\mathrm{Im}(\rho_{re}) \tag{2.39}$$

$$\dot{\rho}_{gg} = \Gamma_e\rho_{ee} + \Omega_1\mathrm{Im}(\rho_{eg}) \tag{2.40}$$

$$\dot{\rho}_{rr} = -\Gamma_r\rho_{rr} - \Omega_2\mathrm{Im}(\rho_{re}) \tag{2.41}$$

$$\dot{\rho}_{eg} = -(\Gamma_e/2 - i\delta_1)\rho_{eg} + i\frac{\Omega_1}{2}(\rho_{ee} - \rho_{gg}) - i\frac{\Omega_2}{2}\rho_{rg} \tag{2.42}$$

$$\dot{\rho}_{rg} = -((\Gamma_r + \gamma_d)/2 - i\delta)\rho_{rg} + i\frac{\Omega_1}{2}\rho_{re} - i\frac{\Omega_2}{2}\rho_{eg} \tag{2.43}$$

$$\dot{\rho}_{re} = -((\Gamma_r + \Gamma_e + \gamma_d)/2 - i\delta_2)\rho_{re} + i\frac{\Omega_1}{2}\rho_{rg} + i\frac{\Omega_2}{2}(\rho_{rr} - \rho_{ee}). \tag{2.44}$$

The equations for $\rho_{ge} = \rho_{eg}^*$, $\rho_{gr} = \rho_{rg}^*$, and $\rho_{re} = \rho_{er}^*$ have been omitted. This set of equations is solved numerically; however, different approximations can be used to derive analytical solutions in order to gain a better physical understanding.

2.2.1. Effective two-level model

The time dynamics of a three-level atom approximates that of a two-level atom when $|\delta_1 - \delta_2| \gg |\delta|, \Omega_1, \Omega_2$ [36]. In this case the intermediate state is adiabatically eliminated as it remains mostly unpopulated, assuming the initial state does not contain $|e\rangle$. The resulting Hamiltonian has the form of Eq. 2.12 parametrised by

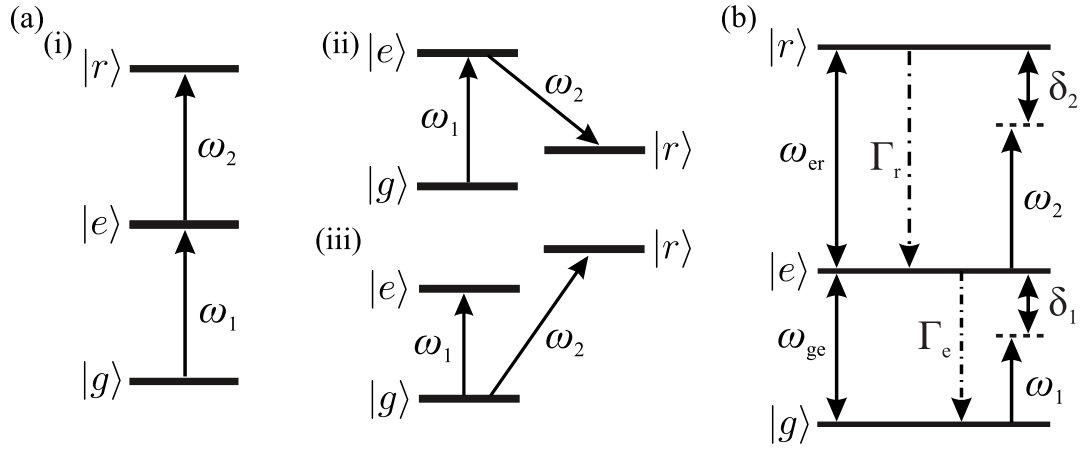

Figure 2.4.: (a) The different possible energy schemes for a driven three-level atom: (i) Ladder type system, (ii) Λ type system and (iii) V type system. (b) Detailed scheme for the ladder type system used in this thesis.

an effective detuning and Rabi frequency:

$$\Delta_{eff} = \delta + \frac{\Omega_1^2 - \Omega_2^2}{2(\delta_1 - \delta_2)}, \qquad \Omega_{eff} = \frac{\Omega_1 \Omega_2}{\delta_1 - \delta_2}. \tag{2.45}$$

Then, everything applicable to a two-level atom is valid in this approximation as long as the replacements $\Delta \to \Delta_{eff}$ and $\Omega \to \Omega_{eff}$ are performed. Note that at two-photon resonance $\delta_1 = -\delta_2 = \Theta$ Eqs. (2.45) result in $\Delta_{eff} = (\Omega_1^2 - \Omega_2^2)/4\Theta$ which is just the difference between the Stark shifts of both transitions and $\Omega_{eff} = \frac{\Omega_1 \omega_2}{2\Theta}$.

2.2.2. Low excitation regime

When an arbitrary value of Δ must be considered, another useful approximation is to consider the driving field for the lower transition to be weak (i.e. low saturation: $2\Omega_1^2/\Gamma_e^2 \ll 1$). Though, similar to the two-level effective model the intermediate level can be eliminated since the populations ρ_{ee} and ρ_{rr} can be considered negligible. This, in turn, results in $\rho_{re} \approx 0$ [35]. Then, after some algebra, the steady-state

equations for a three-level system are derived:

$$\rho_{eg}^{\mathrm{ss}} = \frac{-i\Omega_1/\Gamma_e}{1 - i2\delta_1/\Gamma_e + \frac{\Omega_2^2/\Gamma_e\gamma_r}{1-i2\delta/\gamma_r}} \tag{2.46}$$

$$\rho_{rg}^{\mathrm{ss}} = \rho_{eg}^{\mathrm{ss}} \frac{-i\Omega_2/\gamma_r}{1 - i2\delta/\gamma_r}. \tag{2.47}$$

Where $\gamma_r = \Gamma_r + \gamma_d$ is the broadened linewidth of the upper state.

The linear susceptibility for the lower transition χ introduced in Eq. (2.31) is then modified by the introduction of a third level. Indeed, the coupling of a two-level atom to a third level by a Rabi frequency Ω_2, using Eq. 2.46, results in

$$\chi = \frac{6\pi\zeta}{k^3} \frac{i}{1 - i2\delta_1/\Gamma_e + \frac{\Omega_2^2/\Gamma_e\gamma_r}{1-i2\delta/\gamma_r}} \tag{2.48}$$

with the wavenumber of the lower transition k. It is remarkable that an apparently simple modification in the denominator results in many different new phenomena such as Electromagnetically Induced Transparency (EIT), Autler-Townes splitting and dark states. These effects can be quantitatively well described in a semiclassical context; in particular, by analyzing Eq. (2.48).

2.2.3. Electromagnetically Induced Transparency (EIT)

At two-photon resonance ($\Delta = \delta_1 = -\delta_2$) the three eigenstates of Eq. (2.38) are denoted as $|a_0\rangle$ and $|a_\pm\rangle$:

$$|a_0\rangle = \cos\theta\,|g\rangle - \sin\theta\,|r\rangle \tag{2.49}$$

$$|a_+\rangle = \sin\theta\sin\phi\,|g\rangle + \cos\phi\,|e\rangle + \cos\theta\sin\phi\,|r\rangle \tag{2.50}$$

$$|a_-\rangle = \sin\theta\cos\phi\,|g\rangle - \sin\phi\,|e\rangle + \cos\theta\cos\phi\,|r\rangle\,, \tag{2.51}$$

where the coefficients θ and ϕ are defined such that $\tan\theta = \Omega_1/\Omega_2$ and $\tan 2\phi = \sqrt{\Omega_1^2 + \Omega_2^2}/\Delta$. In Fig. 2.5 the energy distribution according to their respective eigenvalues $E_\pm = 1/2(\Delta \pm \sqrt{\Delta^2 + \Omega_1^2 + \Omega_2^2})$ and $E_0 = 0$ is shown for the resonant ($\Delta = 0$) and dispersive ($\Delta \gg \Omega_2$) case in the low excitation regime (i.e. $|a_0\rangle \to |g\rangle$).

In this context the dressed atom picture is very useful to qualitatively understand EIT. At resonance, a probe photon excites the atom from state $|g\rangle$ up to $|e\rangle$. In the

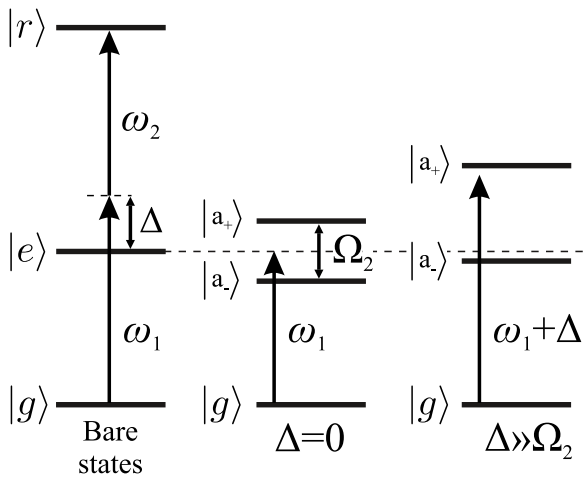

Figure 2.5.: Left: level scheme of the bare states of a three-level atom. In the weak probe limit and at two-photon resonance ($\delta_1 = -\delta_2 = \Delta$) the dressed states $|a_\pm\rangle$ are introduced. When $\Delta = 0$ these states symmetrically split around $|e\rangle$ resulting in destructive interference for the $|g\rangle \rightarrow |e\rangle$ transition. When $\Delta \gg \Omega_2$ the system behaves like a driven two-level atom consisting of states $|g\rangle$ and $|r\rangle$ with an effective detuning $\Omega_2^2/4\Delta$.

dressed atom picture, however, this photon absorption can only be done via $|a_+\rangle$ or $|a_-\rangle$ as virtual states. Furthermore, since $|e\rangle = \frac{1}{\sqrt{2}}|a_+\rangle - \frac{1}{\sqrt{2}}|a_-\rangle$, the transition probability amplitudes must be summed up meaning that they may interfere. In fact, whenever the two-photon resonance condition is met (i.e. $\delta_1 = -\delta_2$) they interfere destructively. As a result, the atom does not scatter probe photons (i.e. it becomes transparent) since the probability of photon absorption is zero. In general, the physical concept behind EIT is that of interference between different atomic transition paths [37, 38].

Another consequence of this type of interference is the appearance of dark states. An atom is in a dark state when it does not interact with light (i.e. it cannot absorb or emit photons). This is always the case for $|a_0\rangle$ since it has a zero eigenvalue. It is nice to realize that in the weak probe limit $|a_0\rangle \rightarrow |g\rangle$ confirming the result from the discussion above: an atom will remain in the ground state without scattering photons. Also, notice that Eq. (2.50) does not have a contribution from state $|e\rangle$ meaning that, by spontaneous decay from $|e\rangle$, atoms can populate $|a_0\rangle$ and stay trapped there. This effect is called Coherent Population Trapping (CPT) [39] and, ideally, $|r\rangle$ must be metastable. This explains why EIT was first observed in $\Lambda-$type

systems which appear more naturally in hyperfine ground states [40]. Furthermore, CPT can then be used as a tool to control the population on $|r\rangle$ by a method called Stimulated Rapid Adiabatic Passage (STIRAP) [41] which, in contrast to a two-photon π-pulse, relies on incoherent processes.

Fig. 2.6 shows the absorption profiles (i.e. the imaginary part of Eq. (2.48) for a unity prefactor) for different values of δ_2 and Ω_2 as a function of the probe detuning δ_1. In the ideal case when $\gamma_r = 0$ full transparency is achieved for any (δ_2, Ω_2) pair at $\delta_1 = -\delta_2$. Otherwise, Ω_2 needs to be increased in order to approach full transparency. However, when $\Omega_2 \gg \Gamma_e$ the absorption profile carries the signature of an Autler-Townes (AT) doublet and no longer shows the sharp transparency window with a linewidth smaller than Γ_e [3]. Therefore, one can conclude that EIT, which is the result of destructive interference between excitation paths, happens only when $|a_\pm\rangle$ lie within the linewidth of $|e\rangle$. Otherwise, transparency will not be the result of interference but of Rabi splitting [47].

As mentioned before, when $\delta_2 \neq 0$, the transparency window will move according to the two-photon resonance condition. Nevertheless, as shown in Fig. 2.6, in the EIT regime the linewidth starts broadening and becoming asymmetric as δ_2 increases (e.g. when $\delta_2 = 0.5\Gamma_e$). However, when δ_2 is too large ($\gg \Gamma_e$) the resulting absorption profile is that of a two-level atom together with a Raman peak very close to $\delta_1 = -\delta_2$. On the other hand, in the AT regime, the profile does not change much for detunings much smaller than Ω_2 but for larger ones a Raman peak is similarly observed. This time, however, the Raman peak broadens and is pushed farther away due to the larger AC Stark shift which, at the same time, pushes the central peak to the opposite direction.

The transparency features explained so far can also appear when $\gamma_r \neq 0$. By comparing Eqs. 2.31 and 2.48 it can be argued that all transparency features must be present as long as the coupling field Rabi frequency satisfies

$$|\Omega_2|^2 \gg \Gamma_e \gamma_r. \tag{2.52}$$

It must be pointed out that this condition accounts for $\gamma_r = \Gamma_r + \gamma_d$; thus, it depends on the total decoherence rate. Consequently, any process that broadens

[3] Additionally, although not shown in Fig. 2.6, the dispersion curve in the EIT regime shows a very steep slope that can be exploited for different applications [42, 43, 44, 45, 46].

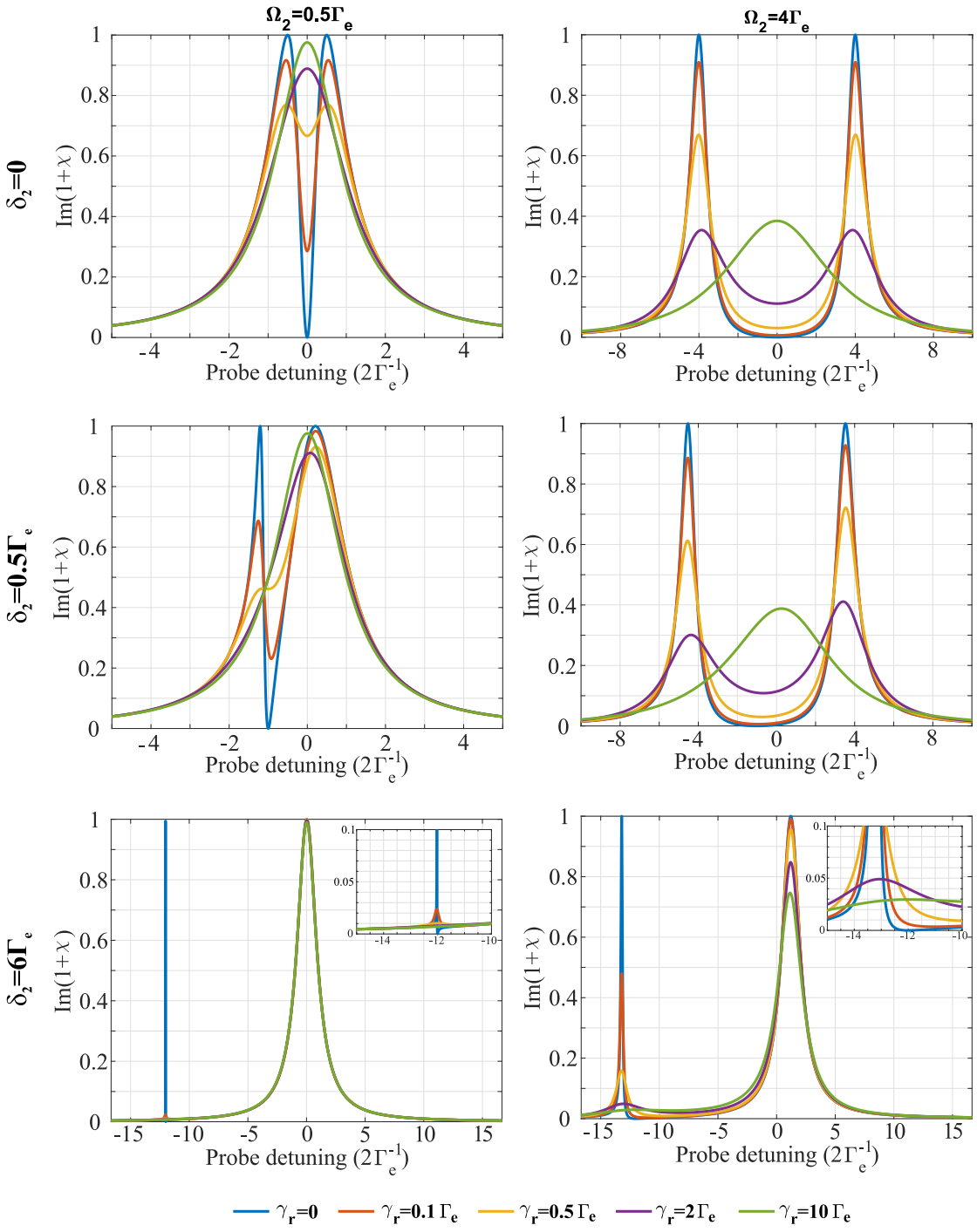

Figure 2.6.: Absorption profiles of the lower transition on a ladder-type three-level atom in the weak probe limit for different (δ_2, Ω_2) pairs and values of γ_r. In spite of γ_r, transparency can be recovered by increasing Ω_2; however, a too large value ($\gg \Gamma_e$) transforms the EIT into an AT doublet. The last row shows the dispersive regime where the system behaves as having two resonance frequencies. The insets better show the area around the two-photon resonance condition: transparency is achieved exactly when this condition is met while the Raman peak moves away from this point due to the AC Stark shift.

the linewidth of $|r\rangle$ (in general, also of $|e\rangle$) can potentially wash out the interference process responsible for EIT. This behavior is observed throughout Fig. 2.6 where traces with different colors represent various values of γ_r in units of Γ_e.

2.3. Cavity QED

Quantum Electrodynamics (QED) studies the interaction between matter and light when both parts are described within quantum theory. In this context, the monochromatic (single-mode) light field which has been used so far is now described by creation ($\hat{a}^\dagger$) and annihilation ($\hat{a}$) operators [48]:

$$\hat{\mathcal{E}} = i\sqrt{\frac{\hbar\omega}{2\epsilon_0 \mathrm{V}}}(\hat{a}\boldsymbol{\varepsilon} - \hat{a}^\dagger\boldsymbol{\varepsilon}^*). \tag{2.53}$$

Where $\boldsymbol{\varepsilon}$ is the unit polarization vector and the prefactor $i\sqrt{\hbar\omega/2\epsilon_0 V}$ is interpreted as the single-photon electric field amplitude with the quantization volume V.

When interacting with a two-level atom, following Eq. (2.3), the interaction Hamiltonian is, after the RWA, given by the Jaynes-Cummings Hamiltonian [31, 49]:

$$\hat{\mathcal{H}}_{int} = \hbar g_0(i\hat{a}^\dagger\hat{\sigma}^- - i\hat{a}\hat{\sigma}^+). \tag{2.54}$$

The energy exchange rate $g_0 = \mathbf{d}_{ge}\cdot\boldsymbol{\varepsilon}\sqrt{\frac{\omega}{2\hbar\epsilon_0 V}}$ is interpreted as half the single-photon Rabi frequency.

Furthermore, the energy of the field is given by the Hamiltonian

$$\hat{\mathcal{H}}_f = \hbar\omega\left(\hat{a}^\dagger\hat{a} + \frac{1}{2}\right) \tag{2.55}$$

where the factor $1/2$ gives the vacuum energy $\hbar\omega/2$.

In the present thesis, a single mode of a light field is selected with the aid of an optical cavity or resonator; hence, the name cavity QED. In what follows, the properties and equations governing the dynamics between a set of atoms and a cavity will be described in more detail.

2.3.1. The optical resonator

For the sake of simplicity, this section will be dedicated to linear, near confocal, cavities[4]. They are composed of two spherical mirrors aligned on the same axis (i.e. the cavity axis) facing each other as in Fig. 2.7. The cavity's length L is the distance between the mirrors measured along its axis and is nearly equal to the mirror's radius of curvature r_c. Furthermore, in our case, the transmission of both mirrors is considered to be equal.

An electric field with a Gaussian intensity distribution is stable or can resonate inside an optical cavity [50]. It propagates, under the paraxial approximation, as a plane wave with wavevector $\mathbf{k}$ parallel to the cavity axis (z direction). Therefore, the field can be written as $E(x,y,z) = u(x,y,z)e^{-ikz}$ with

$$u(x,y,z) = \frac{w_0}{w(z)} e^{-\frac{r_\perp^2}{w(z)^2}} e^{i\left(\Phi(z) - k\frac{r_\perp^2}{2R(z)}\right)} \tag{2.56}$$

and $r_\perp^2 = x^2 + y^2$. As expected, it is observed that the intensity $I(x,y,z) \propto |E(x,y,z)|^2$ follows a Gaussian function which decreases when moving away from the focus. This decrease is measured by the beam waist $w(z)$:

$$w(z) = w_0 \sqrt{1 + \left(\frac{z}{z_R}\right)^2} \tag{2.57}$$

where $z_R = \frac{\pi w_0^2}{\lambda}$ is the Rayleigh length. Similarly, the field's wavefront is modified along z and r being curved like a sphere centered at the origin with radius

$$R(z) = z\left(1 + \left(\frac{z_R}{z}\right)^2\right). \tag{2.58}$$

Furthermore, in the longitudinal direction, the field differs from a plane wave by the Gouy phase:

$$\Phi(z) = \arctan\left(\frac{z}{z_R}\right). \tag{2.59}$$

It is important to realize from Eqs. (2.57), (2.58) and (2.59) that the propagation

[4]However, the methods introduced in this section can be extrapolated to be used for other types of cavities. In particular, for example, the bow-tie cavity used to generate the blue light necessary to couple atoms to Rydberg states.

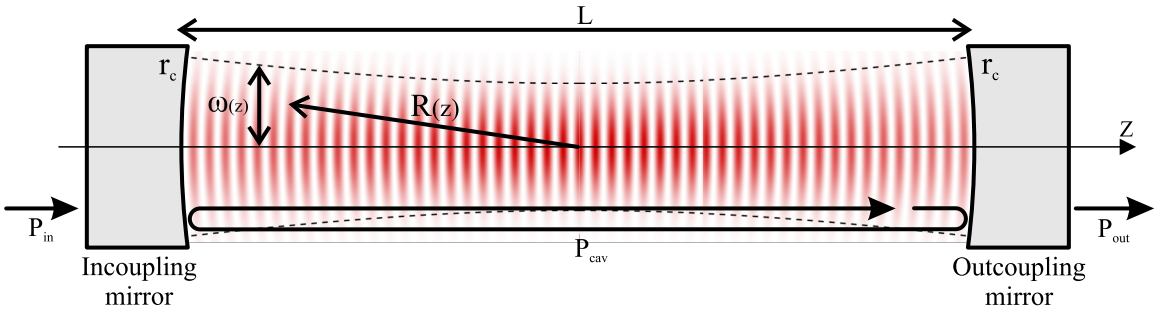

Figure 2.7.: Sketch of a confocal cavity of length L and curved mirrors with radius of curvature r_c. A Gaussian shaped standing wave (the fundamental mode) resonates inside the cavity. Its beam waist increases along the cavity axis (z-axis) and its radius of curvature $R(z)$ coincide with r_c at the position of the mirrors. Due to the several round trips light makes inside the cavity, the intracavity power is enhanced relative to the power coming into it.

of a Gaussian beam is completely defined by the wavelength λ and the beam waist w_0 located at the origin[5].

The stability or phase-matching condition for a light field inside the cavity is constructive interference (i.e. it must repeat itself after a round-trip). Therefore, for the cavity considered here, this condition translates into $R(z = \pm L/2) \stackrel{!}{=} \pm r_c$ and $\int_0^{2L} \varphi' dz \stackrel{!}{=} 2\pi q$ with $q \in \mathbb{Z}$. While the former equality fixes the beam waist w_0, the latter defines a set of allowed frequencies $\{\nu_q\}$ which are known as longitudinal frequencies. In particular, the frequency difference $\nu_{q+1} - \nu_q = \frac{c}{2L}$ is called Free Spectral Range (FSR).

Other Gaussian beams can also resonate inside the cavity. These are termed transverse modes and are indexed by the non-negative integer numbers m and n. In particular, when $m = n = 0$ the mode is called fundamental. These modes are described by rewriting Eq. (2.56) as

$$u_{mn}(x, y, z) = \frac{w_0}{w(z)} H_m\left(\sqrt{2}\frac{x}{w(z)}\right) H_n\left(\sqrt{2}\frac{y}{w(z)}\right) e^{-\frac{r_\perp^2}{w(z)^2}} e^{i\left(\Phi_{mn}(z) - k\frac{r_\perp^2}{2R(z)}\right)} \quad (2.60)$$

where $H_{m,n}$ is the Hermite polynomial of order m, n. Thus, these indices indicate the number of nodes that the transverse intensity pattern will show along the x and

[5]Nevertheless, the beam waist w_0 does not necessarily have to be located at $z = 0$. Consequently, the change $z \to z - z_0$ must be made in Eqs. (2.57), (2.58) and (2.59).

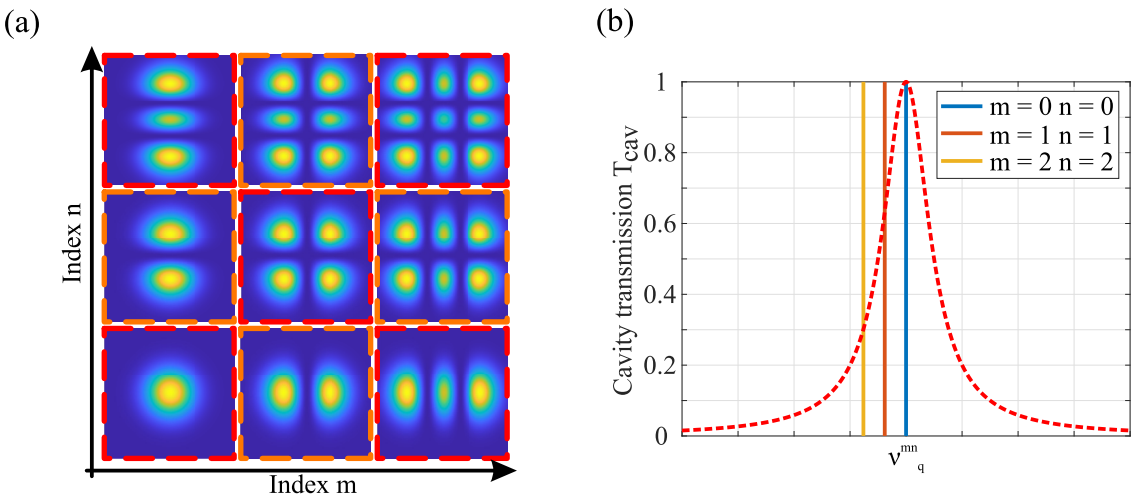

Figure 2.8.: (a) Transverse spatial profiles of resonant cavity modes given by $|u_{mn}(x, y, z = 0)|^2$ (Eq. (2.60)). These are labeled with coordinates (m, n) locating the fundamental (0,0)-mode at the lower left corner. In an ideal confocal cavity, transverse modes with the same border color are degenerate (i.e. resonate at the same frequency ν_q^{mn}) (b) In the near confocal case this degeneracy is lifted; however, if ν_q^{mn} lies within the cavity FWHM, it is still considered degenerate. Here, for $\delta L/L$, the (1,1)-mode is degenerate but not the (2,2)-mode.

y direction (see Fig. 2.8(a)). In addition, the Gouy phase is modified:

$$\Phi_{mn}(z) = (m + n + 1) \arctan\left(\frac{z}{z_R}\right). \tag{2.61}$$

The dependence of the Gouy phase on m and n results in a relative phase between the transverse modes and the fundamental mode after a round-trip. As a result, the transverse modes have different resonant frequencies (i.e. transverse frequencies) which complement the set $\{\nu_q\}$ of longitudinal frequencies. Indeed, imposing the stability condition together with Eq. (2.61) it is obtained

$$\nu_q^{mn} = \mathrm{FSR}\left(q + \frac{n + m + 1}{\pi} \cos^{-1}\left(1 - \frac{L}{r_c}\right)\right). \tag{2.62}$$

In the perfect confocal case ($L = r_c$) transverse modes with $m + n =$ even (odd) are degenerate or resonate at the same frequency ν_q^{even} (ν_q^{odd}) such that $\nu_q^{even} - \nu_q^{odd} = \mathrm{FSR}/2$. As L gets larger the transverse frequencies start shifting until all modes are

degenerate at the concentric cavity limit ($L = 2r_c$). As will be explained next, due to the finite lifetime of light inside the resonator, the uncertainty of ν_q^{mn} is given by the FWHM. Therefore, modes can be considered degenerate when their frequencies lie within a FWHM (see Fig. 2.8(b)).

Another aspect of resonators or cavities is their capacity to store energy. This characteristic is measured by the Quality factor Q and is dependent on the losses suffered by the light field after a round-trip inside the resonator. Energy is lost out of the resonator mode by transmission through the mirrors, by absorption of an intracavity element (e.g. atoms, non-linear crystal) or scattering due to mirror imperfections.

Similarly, energy can be input into the resonator by an incident field E_{in}. In order to efficiently couple light into the resonator, the Gaussian shape of E_{in} must be mode-matched with one of the resonator modes. Additionally, the mirror upon which E_{in} reflects is called incoupling mirror while the outcoupling mirror is the one from which light only leaks out of the cavity. Ideally, each mirror has a reflectivity r_j and transmissivity t_j such that $r_j^2 + t_j^2 = 1$. Then, when energy is lost only by transmission through the mirrors, the phase-matching condition implies $r_{out} = r_{in} = r$ which results in

$$T_{cav} = \frac{P_{out}}{P_{in}} = \frac{T^2}{(1-R)^2 + 4R\sin^2(\varphi/2)} \tag{2.63}$$

where $T = t^2$, $R = r^2$ and $\varphi = 2\pi\frac{\nu-\nu_q}{FSR}$. For this thesis it is a good approximation to consider $R \sim 1$ and $\varphi \ll 1$. In this limit, the cavity transmission has a Lorentzian shape [6]:

$$T_{cav} = \frac{1}{1 + (\varphi/T)^2}. \tag{2.64}$$

The resonator's linewidth is then identified as $FWHM = FSR\frac{T}{\pi}$ which corresponds to an inverse lifetime of

$$\tau_{cav}^{-1} = \kappa = 2FSR \cdot T. \tag{2.65}$$

[6] In general, the light field's round trip reflectivity is $r_m = r_1 r_2\sqrt{1-\mathcal{L}}$ with $\mathcal{L}$ denoting other losses inside the resonator besides the mirrors. Then, Eq. (2.64) is generalized to

$$T_{cav} = \frac{T_1 T_2}{(1-r_m)^2 + r_m\varphi^2}$$

and the impedance-matching condition to $1 - \mathcal{L} = r_1^2$. It follows that $\tau_{cav}^{-1} = 2FSR\frac{1-r_m}{\sqrt{r_m}}$ which in turn implies $\mathcal{F} = \pi\frac{\sqrt{r_m}}{1-r_m}$

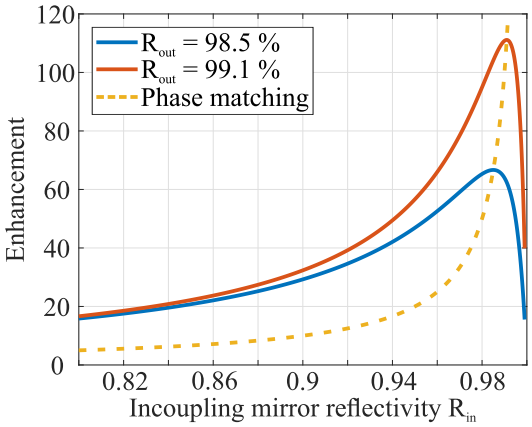

Figure 2.9.: Knowing the resonator losses beforehand (R_{out}), its enhancement can be plotted as a function of the incoupling mirror reflectivity R_{in}. The maximum enhancement for a given R_{out} is reached when the phase matching condition is satisfied (dashed).

The characteristic parameter for optical resonators to quantify its capacity to store light is the finesse $\mathcal{F}$ given by

$$\mathcal{F} = \frac{FSR}{FWHM}. \tag{2.66}$$

By realizing that FSR^{-1} is the light field's round trip time, $\frac{\mathcal{F}}{2\pi} = \tau_{cav}/\tau_{rt}$ which can be interpreted as the light field's number of round trips before leaving the resonator. Because of this, the power circulating inside the resonator $P_{cav} = P_{out}/T$ can be larger than $T \cdot P_{in}$. To gauge this, the resonator enhancement is introduced [7]

$$\Xi = \frac{P_{cav}|_{\varphi=0}}{P_{in}} = \frac{1}{T} = \frac{\mathcal{F}}{\pi}. \tag{2.68}$$

In particular, this is an important gauge to consider in the frequency-doubling resonator.

[7] In fact, this value is reached only when the phase-matching condition is satisfied. In general, but still considering loss due to transmission only, the enhancement is given by

$$\Xi = \frac{T_1}{(1 - r_m)^2}. \tag{2.67}$$

This relation is plotted in Fig. 2.9 for two different outcoupling mirror reflectivities.

2.3.2. Atom-cavity Bloch equations

Each mode of the optical resonator or cavity is described by a single creation (anihilation) operator $\hat{a}_q^\dagger$ ($\hat{a}_q$)[33]. As mentioned before, all optical modes within the cavity's FWHM are considered degenerate. However, here it will be assumed that only a single mode is driven and, at the same time, interacts with the atoms.

First, we recall Eq. 2.53 and identify the field frequency as the cavity's mode frequency ω_c. Also, the quantization volume V is identified as

$$V = \int |\psi(\mathbf{r})|^2 d^3\mathbf{r}. \tag{2.69}$$

Where $\psi(\mathbf{r})$ is a function describing the Gaussian mode resonating inside the cavity. Of main interest to us is the fundamental mode in a confocal cavity which results in $\psi(\mathbf{r}) = (u(\mathbf{r})e^{-ikz} + u^*(\mathbf{r})e^{ikz})/\sqrt{2}$. In particular, if the cavity's length L is smaller than the Rayleigh length z_R we have approximately

$$|\psi(\mathbf{r})|^2 = \cos(kz)^2 e^{-2r_\perp^2/w_0^2} \tag{2.70}$$

which results in $V = \frac{\pi w_0^2 L}{4}$.

Additionally, as mentioned before, the light field in the cavity has a lifetime due to the non-perfectly reflecting mirrors. On one hand, this means that we can drive the cavity (i.e. light can enter or feed the cavity mode) which can be described with the Hamiltonian

$$\hat{\mathcal{H}}_D = i\eta(\hat{a} - \hat{a}^\dagger), \tag{2.71}$$

where $\left(\frac{\eta}{\kappa}\right)^2 = \Xi\frac{I_{in}}{\hbar\omega_c}$ and $I_{in} = \frac{2P_{in}}{\pi w_0^2}$. On the other hand, light leaks out of the cavity through its mirrors. This incoherent process is accounted in the master equation with a dissipator consisting of the Lindblad operator $\hat{\mathrm{L}}_{cav} = \hat{a}$ with rate $\gamma_{cav} = \kappa$.

Furthermore, since we are interested in the interaction of N two-level atoms with the cavity mode we use, instead of Eq. (2.54), the Tavis-Cummings Hamiltonian is introduced. Thus, considering a set of N atoms distributed within the cavity we have

$$\hat{\mathcal{H}}_{int} = \sum_j^N \hbar g_j(i\hat{a}^\dagger\hat{\sigma}_j^- - i\hat{a}\hat{\sigma}_j^+). \tag{2.72}$$

Where $g_j(\mathbf{r}) = g_0\psi(\mathbf{r})$ quantifies the coupling rate of each atom according to its

location in the cavity mode. Then, we can think of an effective number of atoms [51] $N_{eff} = \int \zeta(\mathbf{r})|\psi(\mathbf{r})|^2 d^3\mathbf{r}$ which actually interact with the cavity. Indeed, considering the atomic density to be spherically symmetric with a Gaussian distribution as

$$\zeta(\mathbf{r}) = \zeta_0 e^{-r^2/2w^2} \tag{2.73}$$

such that $\zeta_0 = \frac{N}{(w\sqrt{2\pi})^3}$ we obtain, together with Eq. (2.70), $N_{\text{eff}} = \zeta_0 w w_0^2 (\pi/2)^{3/2}$. Consequently, we can make the changes $g_j \to g_0$ and $N \to N_{\text{eff}}$ in Eq. (2.72).

Finally, the atom-cavity system is described by the Hamiltonian

$$\hat{\mathcal{H}}_{a-c} = \hat{\mathcal{H}}_a + \hat{\mathcal{H}}_f + \hat{\mathcal{H}}_{int} + \hat{\mathcal{H}}_D \tag{2.74}$$

and the dissipators due to spontaneous decay of the atoms and cavity losses following Eq. (2.21). But, as the Fock space has an infinite number of states, the atom-cavity density matrix will have an infinite number of components which results in an infinite set of differential equations. Using the Heisenberg picture one can compactly write a finite set of equations for the atomic variables; however, the product terms (e.g. $\hat{a}\hat{\sigma}_j^z$, $\hat{a}\hat{\sigma}_j^+$ and $\hat{a}^\dagger\hat{\sigma}_j^-$) necessary for describing atom-field correlations imply solving more, in principle, an infinite number of equations.

At this point it is important to introduce the cooperativity parameter

$$C_1 = \frac{2g_0^2}{\kappa\Gamma} \tag{2.75}$$

which breaks down the atom-cavity dynamics into different regimes according to its value. In particular, the semiclassical limit is reached when $C_1 \to 0$ and $N_{\text{eff}} \to \infty$ such that $C_1 N_{\text{eff}}$ is finite [52]. In this limit it is possible to neglect correlations or entanglement between the field and the atoms, the system's density operator can be written as $\rho(t) = \rho_a(t) \otimes \rho_c(t)$. Consequently, taking the expectation values in the Heisenberg equations, any product term can be separated (e.g. $\langle \hat{a}\hat{\sigma}_j^z \rangle = \langle \hat{a} \rangle \langle \hat{\sigma}_j^z \rangle$).

As a result, the so called mean-field equations are obtained:

$$\frac{d}{dt}\langle\hat{a}\rangle = -(\kappa/2 - i\Delta)\langle\hat{a}\rangle + g_0\langle\hat{\sigma}^-\rangle + \eta \tag{2.76}$$

$$\frac{d}{dt}\langle\hat{\sigma}^-\rangle = -(\Gamma/2 - i\delta_p)\langle\hat{\sigma}^-\rangle + g_0\langle\hat{a}\rangle\langle\hat{\sigma}^z\rangle \tag{2.77}$$

$$\frac{d}{dt}\langle\hat{\sigma}^z\rangle = -\Gamma(N_{eff} + \langle\hat{\sigma}^z\rangle) - 2g_0(\langle\hat{a}\rangle\langle\hat{\sigma}^+\rangle + \langle\hat{a}^\dagger\rangle\langle\hat{\sigma}^-\rangle). \tag{2.78}$$

Where the collective variables $\langle\hat{\sigma}^\pm\rangle = \sum_{j=1}^{N_{eff}}\langle\hat{\sigma}_j^\pm\rangle$ and $\langle\hat{\sigma}^z\rangle = \sum_{j=1}^{N_{eff}}\langle\hat{\sigma}_j^z\rangle$ together with the cavity detuning $\delta_c = \omega_c - \omega_{ge}$, probe detuning relative to the atomic transition $\delta_p = \omega_p - \omega_{ge}$ and relative to the cavity $\Delta = \delta_p - \delta_c$ have been introduced.

Solving for the steady-state in the weak probe limit, the cavity transmission T_{cav} can be calculated as [52]

$$\frac{|\langle\hat{a}\rangle|^2}{(2\eta/\kappa)^2} = T_{cav} = \left|\frac{1}{1 - i(2\Delta/\kappa + 2C_1N_{eff}\chi')}\right|^2 \tag{2.79}$$

where $\chi' = \frac{i}{1-i2\delta_p/\Gamma}$ is proportional to the atomic susceptibility. Indeed, one can rewrite $2C_1N_{eff}\chi'$ in terms of χ (Eq. (2.30)) and ζ_0 (Eq. (2.73)) to obtain [53]

$$2C_1N_{eff}\chi' = k\ell\chi\mathcal{F}/\sqrt{2\pi} \tag{2.80}$$

where $\ell = 2w$ is the diameter of the atomic cloud. Therefore, one can notice that the atomic susceptibility is modified by the cavity through its finesse $\mathcal{F}$. In particular, the optical density is enhanced by the several round trips ($\mathcal{F}/2\pi$) made by light or a photon before leaking out of the cavity.

Interestingly, in Ref. [54] it is shown that the cavity transmission for the atom-cavity system in steady-state can be derived from fully classical concepts in the form of Eq. (2.63):

$$T_{cav} = \frac{T^2}{(1 - Re^{-\alpha\ell})^2 + 4Re^{-\alpha\ell}\sin^2(\Phi/2)} \tag{2.81}$$

with $\Phi = \frac{\Delta}{2\mathrm{FSR}} + \frac{k\ell}{2}\mathrm{Re}(\chi)$ and $\alpha = k\,\mathrm{Im}(\chi)$ is the atomic absorption coefficient. Then, Eq. (2.79) can be recovered by assuming that Δ and the atomic dispersion are small compared to the FSR; thus, $\sin(\Phi/2) \to \Phi/2$.

For a given empty cavity detuning (δ_c) the atom-cavity system will resonate (i.e. store or transmit the most light) at different probe frequencies δ_p such that

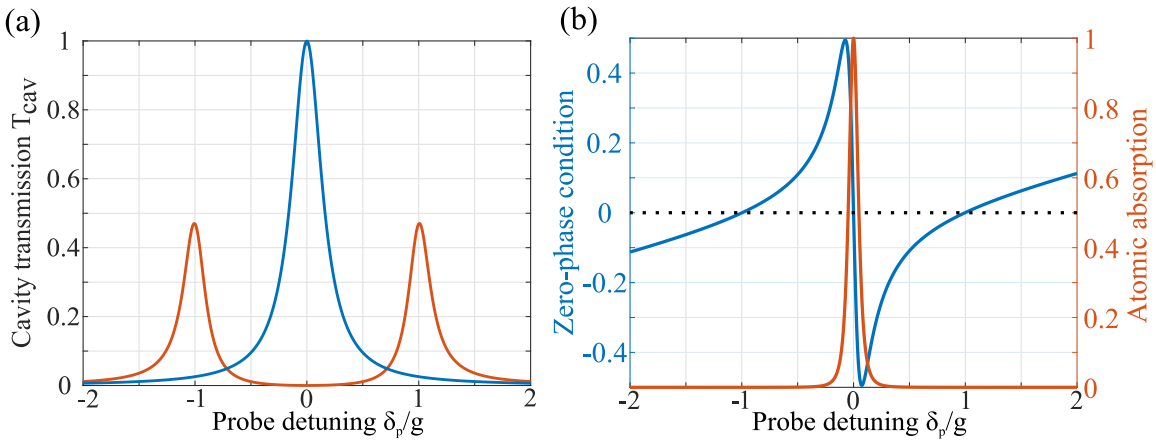

Figure 2.10.: (a) Transmission of a cavity resonant with the atomic transition ($\delta_c = 0$) as a function of the probe detuning for the cases of an empty cavity (blue) and with atoms inside (orange) where normal mode splitting is observed. (b) The atom-cavity system resonates at those probe detunings δ_p where the zero-phase condition is fulfilled. Even though three resonances exist the middle one is highly absorbed by the atoms; thus, is not transmitted by the cavity

Φ is a multiple of 2π or, equivalently, the zero-phase condition $2(\delta_p - \delta_c)/\kappa + 2C_1 N_{eff}\,\mathrm{Re}(\chi') = 0$ introduced in [55] is met. As a result, the cavity spectrum will show what is called Normal Mode Splitting or Vacuum Rabi Splitting: the single resonant peak of an empty cavity splits in two (see Fig. 2.10). In particular, for the case of a resonant cavity ($\delta_c = 0$), the atom-cavity spectrum is symmetric on δ_p with resonances appearing at

$$\delta_p = \pm g_0 \sqrt{N_{eff}} \tag{2.82}$$

where it has been assumed that $\Omega_{NM} = 2g \gg |\kappa - \Gamma/2|$ with $g = g_0\sqrt{N_{eff}}$. At the same time, the cavity transmission is reduced at these peaks to values of

$$T_{cav} = \left(\frac{1}{1+\Gamma/\kappa}\right)^2. \tag{2.83}$$

Under the same approximation, in the non-resonant cavity case ($\delta_c \neq 0$) the resonances are located at

$$\delta_p = \frac{1}{2}\left(\delta_c \pm \sqrt{\delta_c^2 + \Omega_{NM}^2}\right). \tag{2.84}$$

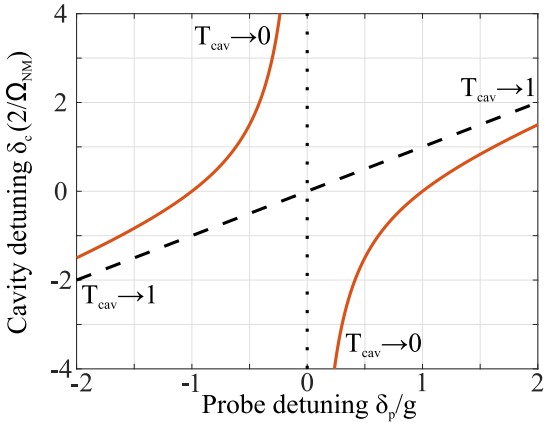

Figure 2.11.: The behavior of these peaks when $\delta_c \neq 0$ is that of an avoided crossing. The heights of these peaks change accordingly: $T_{cav} \to 1(0)$ for the mode with frequency closer (farther) to ω_c.

Thus, they follow an avoided crossing similar as in Eq. (2.13). On the other hand, the cavity transmission $T_{cav} \to 1(0)$ for the resonance peak with the same (opposite) sign as δ_c (see Fig. 2.11).

2.3.3. Cavity EIT

Even though the cavity interacts or exchanges photons only with two atomic states, three-level atoms can influence the atom-cavity dynamics. It has been discussed that, following Eq. (2.79), an atomic ensemble modifies the cavity spectrum via its susceptibility χ which is, in turn, enhanced by the presence of the cavity through its Finesse $\mathcal{F}$. Therefore, it is expected for the cavity transmission to be further modified by the presence of a classical light field coupling the atoms to a third atomic state. Indeed, in Fig. 2.13 the cavity transmission is plotted as a function of δ_p for a cavity resonant with the lower transition ($\delta_c = 0$). There, a narrow transparency window clearly appears at the empty cavity resonance frequency location.

In the EIT regime, Fig. 2.13 (a) shows how the transparency window gets smaller and slightly broadened with increasing γ_r as expected from the discussion in Sec. 2.2. On the other hand, Fig. 2.13 (b) shows how the transparency peak is shifted towards δ_c as Ω_2 is increased while $\delta_2 = \Gamma_e$. This effect, particular of cavity EIT, is called frequency pulling [56, 57]. By analyzing the zero-phase condition $2(\delta_p - \delta_c)/\kappa + 2C_1 N_{eff}\,\mathrm{Re}(\chi') = 0$ one obtains a relation for the frequency at which the

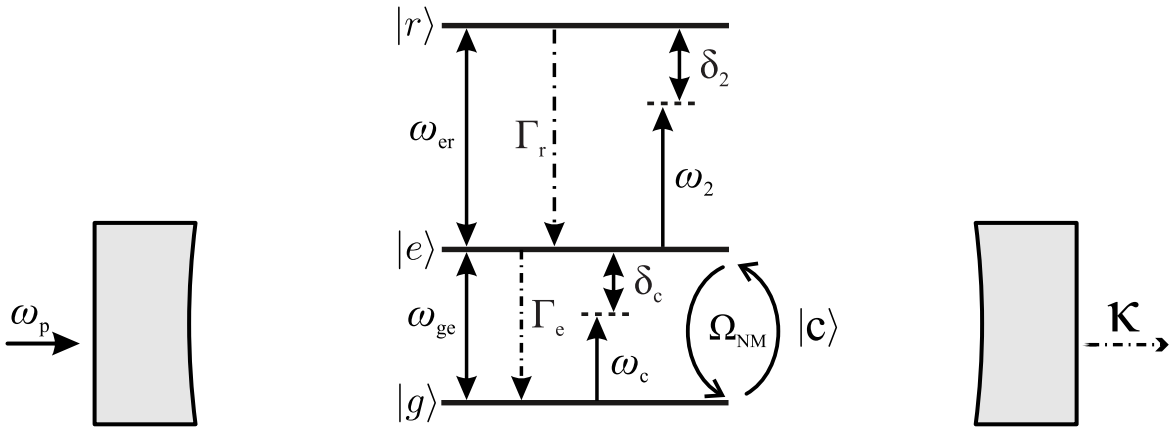

Figure 2.12.: Energy level scheme for cavity EIT. The cavity exchanges photons with the lower transition of an atom at a rate $\Omega_{NM} = 2g_0\sqrt{N_{\text{eff}}}$. On the other hand, the upper transition is strongly driven with Rabi frequency Ω_2 making the absorption paths of the cavity photon to interfere destructively; thus, making the cavity transparent to the probe field.

EIT resonance occurs:

$$\omega_D = \frac{1}{1+\xi}\omega_c + \frac{\xi}{1+\xi}\omega_{ge} \tag{2.85}$$

with $\xi = \frac{k\ell}{\text{FSR}}\frac{d\chi}{d\delta_p}$ and the dark state frequency ω_D.

The situation in cavity EIT is then similar to Sec. 2.2. The main difference being that this time the lower atomic transition is not driven by a classical field but, instead, an atomic ensemble exchanges excitations for cavity photons at a rate $\Omega_{NM} = 2g_0\sqrt{N_{\text{eff}}}$ (see Fig. 2.12). As a result, when tuned at the EIT resonance, the cavity inherits characteristics of the uppermost state $|r\rangle$ since the dark state is written as

$$|D\rangle = \cos\theta\,|C\rangle - \sin\theta\,|r\rangle \tag{2.86}$$

with $\tan\theta = \Omega_{NM}/\Omega_2$ as the dark-state rotation angle and $|C\rangle$ representing a cavity photon. In particular, when a Rydberg state is used as $|r\rangle$ this can be interpreted as the appeareance of a quasiparticle called cavity Rydberg polariton [58]. Under this interpretation Eq. (2.85) is rewritten as the quasiparticle energy relative to ω_{ge}:

$$\delta_D = \delta_c\cos^2\theta - \delta_2\sin^2\theta. \tag{2.87}$$

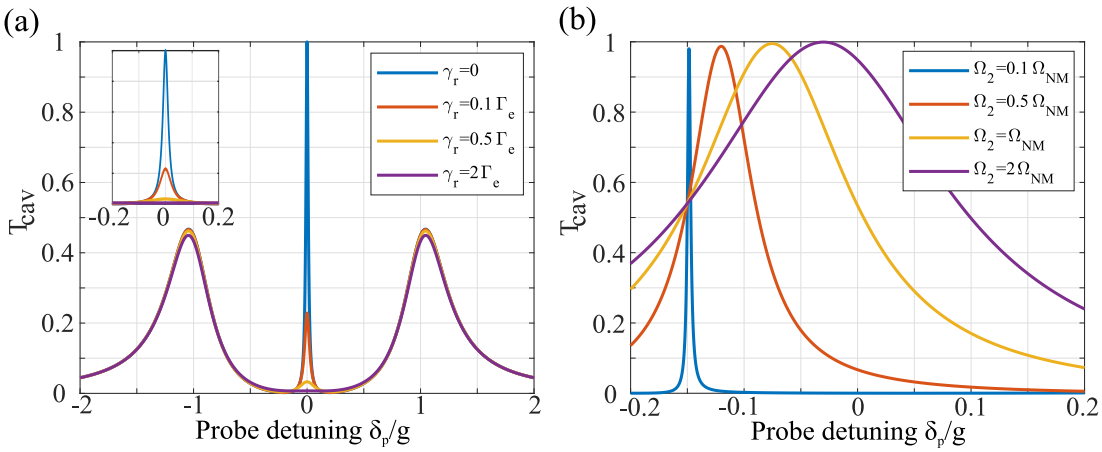

Figure 2.13.: A narrow transparency window appears on the cavity transmission when the atoms are coupled to a third state by a classical light field. In (a) it is shown how the maximum transparency is reduced as γ_r is increased for a fixed $\Omega_{NM} \sim 7\Gamma_e$ and $\Omega_2 \sim 0.6\kappa$. The frequency pulling effect is shown in (b) for $\gamma_r = 0$, $\Omega_{NM} \sim 13\Gamma_e$ and $\delta_c = 0$: the peak transparency is shifted towards δ_c as Ω_2 is increased.

Aditionally, it has a decay rate given by

$$\Gamma_D = \kappa \cos^2\theta + \gamma_r \sin^2\theta. \tag{2.88}$$

In conclusion, the properties (height and width) of the transparency peak from cavity EIT are closely linked to the parameters from the upper transition. Therefore, in order to gauge Ω_2 and γ_r, for a given set of data, a least-square fit to Eq. (2.79) will be performed throughout this thesis. A similar strategy can be found in [53, 57].

2.4. Superradiance

So far in this chapter when considering an atomic ensemble it has been assumed that atoms act independently of one another. On the other hand, when there are interactions between the atoms cooperative effects arise. Interestingly, it is not necessary for atoms to interact directly with each other but photons, for instance, can act as mediators for an effective interaction to arise [59]. The main focus of this thesis is on one particular cooperative effect: superradiance.

2.4.1. Master equation for collective radiative emission

The system considered is that of an ensemble of N two-level atoms with fixed but random positions $\mathbf{R}_j$, parallel dipoles $\mathbf{d}_{ge}$ and with the basis $\left\{|g\rangle_j, |e\rangle_j\right\}$. The atoms, also, are coupled to the electromagnetic vacuum. Following Ref. [59], this can be described by an electric field operator in a plane-wave expansion:

$$\hat{\mathrm{E}}(\mathbf{R}) = \sum_{\mathbf{k}} \mathcal{E}_k \left(\hat{a}_{\mathbf{k}} e^{i\mathbf{k}\cdot\mathbf{R}} + \hat{a}^\dagger_{\mathbf{k}} e^{-i\mathbf{k}\cdot\mathbf{R}}\right) \epsilon_{\mathbf{k}}. \tag{2.89}$$

Here, a perfectly reflecting cube of arbitrary length ℓ is considered. Thus, k is a multiple of $2\pi/\ell$ on each Cartesian coordinate and the index k runs over all field modes: all possible k vectors and polarizations $\epsilon_{\mathbf{k}}$.

An open-system dynamics approach is then applied to reduce the complexity of the system. In this approach the field degrees of freedom are traced out leaving only the atomic Hilbert space of dimension 2^N. The resulting collective quantum master equation for the atomic density operator $\hat{\rho}$ reads

$$\dot{\hat{\rho}}(t) = i\left[\hat{\rho}(t), \sum_{j=1}^{N} \hat{\mathcal{H}}_{aj} + \hat{\mathcal{H}}_{dd}\right] + \mathcal{L}_e\left[\hat{\rho}\right]. \tag{2.90}$$

Here, $\hat{\mathcal{H}}_{aj}$ is the free atom Hamiltonian for the j-th atom while $\hat{\mathcal{H}}_{dd}$ and $\mathcal{L}_e$ describe collective coherent and dissipative processes, respectively. As discussed in Sec. 2.1.1 the last term describes irreversible loss of photons into the electromagnetic vacuum modes and it is defined as

$$\mathcal{L}_e\left[\hat{\rho}\right] = \sum_{jj'=1}^{N} 2\gamma_{jj'}\left(\hat{\sigma}_j \hat{\rho} \hat{\sigma}^\dagger_{j'} - \frac{1}{2}\left\{\hat{\sigma}^\dagger_j \hat{\sigma}_{j'}, \hat{\rho}\right\}\right). \tag{2.91}$$

The matrix $\gamma_{jj'}$ is, in general, non diagonal; thus, it is revealing the collective behavior of the atoms. The collective decay rates are $2\gamma_{jj'} = 3\Gamma_e/2F(k_0 R_{jj'})$ where $R_{jj'} = |\mathbf{R}_j - \mathbf{R}_{j'}|$ and

$$F(kR) = \left(1 + \frac{(\mathbf{e}_d \cdot \nabla_{\mathbf{R}})^2}{k^2}\right) \frac{\sin(kR)}{kR} \tag{2.92}$$

with the unit vector $\mathbf{e}_d \parallel \mathbf{d}_{ge}$.

In order to have a physical picture one may bring the line of thought followed when discussing EIT: interference between excitation paths. This time, however, we are dealing with several many-body states decaying to the same continuum (vacuum modes). If a many-body state is symmetric (antisymmetric) then interference will be constructive (destructive) resulting in superradiant (subradiant) decay. One can also notice that, by diagonalizing $\gamma_{jj'}$, Eq. (2.91) can be written in the form of Eq. (2.21) and, thus, it is explicitly showing that there are many independent possible decay channels.

As explained in [59], the coherent term $\hat{\mathcal{H}}_{dd}$ describes a dipole-dipole interaction characterized by a virtual exchange of a photon via the vacuum modes:

$$\hat{\mathcal{H}}_{dd} = \sum_{j,j'}^{N} \Omega_{jj'} \hat{\sigma}_j^\dagger \hat{\sigma}_{j'} \tag{2.93}$$

where the sum is between pairs of atoms such that $j \neq j'$ and $\Omega_{jj'} = -3\Gamma_e/4G(k_0 R_{jj'})$ with

$$G(kR) = (1-\cos^2\theta)\frac{\cos(kR)}{kR} - (1-3\cos^2\theta)\left(\frac{\sin(kR)}{(kR)^2} + \frac{\cos(kR)}{(kR)^3}\right). \tag{2.94}$$

At first order in R this can be simplified to

$$G(kR) \to \frac{1-3\cos^2\theta}{(kR)^3}. \tag{2.95}$$

This coherent term will be further discussed in the context of Rydberg atoms in Ch. 3.

2.4.2. Dicke superradiance

Dicke was the first to introduce superradiance by considering an elementary situation [14]. This model assumes the case of N atomic dipoles within a very small volume so as to make them indistinguishable but neglecting their dipole-dipole interactions. In this context, we can think of all atoms to be in the same position; thus, maximizing and making all collective decay rates equal: $2\gamma_{jj'} = \Gamma_e$. Consequently, a single

(superradiant) decay channel is open:

$$\mathcal{L}_e[\hat{\rho}] = \Gamma_e \left(\hat{S}\hat{\rho}\hat{S}^\dagger - \frac{1}{2}\left\{ \hat{S}^\dagger \hat{S}, \hat{\rho} \right\} \right). \tag{2.96}$$

Here, the collective spin operator $\hat{S} = \sum_j \hat{\sigma}_j^-$. Additionally, by defining $\hat{S}^z = \sum_j \hat{\sigma}_j^z$ one may complete the spin angular momentum algebra by building the operator $\hat{\mathbf{S}}^2 = (\hat{S}^z)^2 + (\hat{S}^\dagger \hat{S} + \hat{S}\hat{S}^\dagger)/2$. Then, together with the collective basis $|s, m_s\rangle$ such that $0, 1/2 \leq s \leq N/2$ (where $1/2$ holds for odd values of N) and $-s \leq m_s \leq s$ we have

$$\hat{\mathbf{S}}^2 |s, m_s\rangle = s(s+1) |s, m_s\rangle \tag{2.97}$$

$$\hat{S}^z |s, m_s\rangle = m_s |s, m_s\rangle . \tag{2.98}$$

As is known for angular momentum algebra the action of $\hat{S}$ ($\hat{S}^\dagger$) is to decrease (increase) by 1 the value of m_s of a state $|s, m_s\rangle$ without changing s. Therefore, the dynamics governed by Eq. (2.96) happens within a manifold of dimension $2s + 1$ with states parametrized by their value of m_s.

Let us consider a typical situation, when the initial atomic state is fully inverted: $|\psi(t = 0)\rangle = |s = N/2, m_s = N/2\rangle$. Then, the equation of motion for the population difference can then be derived to be

$$\left\langle \dot{\hat{S}}^z \right\rangle = -\Gamma_e (s + m_s)(s - m_s + 1). \tag{2.99}$$

This equation can be rewritten by considering the number of atoms $N = N_e + N_g$ as constant with the number of excited atoms $N_e = s + m_s$:

$$\left\langle \dot{N}_e \right\rangle = -\Gamma_e N_e (N_g + 1). \tag{2.100}$$

This result shows that the decay rate of the atomic ensemble is state-dependent; thus, it no longer follows an exponential law. At $t = 0$ the decay rate equals $N\Gamma_e$ as expected for N independent decaying dipoles. However, notice that the effect of the collective jump operator on $\hat{\rho}$ is to project it into a large superposition of states with only one atom in the ground state: it creates correlations between the atoms. Indeed, this can be quantified as $\left\langle \hat{\sigma}_i^\dagger \hat{\sigma}_j \right\rangle = (s^2 - m_s^2)/N(N-1)$ which is $\neq 0$ for

any state with $m_s \neq \pm N/2$ and reaches a maximum at $m_s = 0$ exactly the state at which the decay rate also reaches its maximum $\propto N^2\Gamma_e$.

In conclusion, this simple example reveals that atomic correlations are the essence of superradiance. These correlations originate from the indistinguishability of the dipoles relative to photon emission which makes it possible to describe the system as an entangled atomic state invariant by atom permutation [26]. From another (more classical) perspective, one may see superradiance as the buildup of a global dipole $\propto N$ (where the individual oscillating dipoles are synchronized in phase) resulting in a radiation rate of $N^2\Gamma_e$. In any case, it is the ensemble and not the individual character of the atoms that plays the fundamental role in superradiance.

2.4.3. Extended ensembles

A more realistic situation is studied in Ref. [60] where an arbitrary distribution of atoms is considered without conditioning the atoms to be closer than the transition wavelength. Following a different approach to Eq. (2.90), Ref. [60] compacts all of the complications due to N cooperating dipoles into a single constant μ. Indeed, the obtained radiation law is given by

$$\frac{dW}{dt} = -\mu\Gamma_e \left(\frac{N}{2} + W\right)\left(\frac{N}{2} - W + \frac{1}{\mu}\right) \tag{2.101}$$

where $W = (N_e - N_g)/2$. Notice that, when $\mu = 1$, Eq. (2.99) is recovered. On the other hand, for $\mu = 0$ the equation describes a set of N independent dipoles radiating each at a rate Γ_e. Therefore, the constant μ can be seen as a gauge of superradiance with respect to the atomic ensemble's size.

The shape factor or cooperativity parameter μ is a complicated function of the size and shape of the volume in which the two-level atoms are contained. In particular, for $N \gg 1$ randomly distributed atoms it is given by

$$\mu = \frac{\int I_0(\mathbf{k})\Lambda(\mathbf{k}, \mathbf{k}_1)d\Omega_{\mathbf{k}}}{I_0}. \tag{2.102}$$

Where $I_0 = \int I_0(\mathbf{k})d\Omega_{\mathbf{k}} = \hbar\omega_0\Gamma_e$ is the total power radiated by a dipole. Also, the

function Λ is defined with respect to the emission ($\mathbf{k}$) and excitation ($\mathbf{k}_1$) wavevector:

$$\begin{aligned}\Lambda(\mathbf{k},\mathbf{k}_1) &= \left|\frac{1}{N}\sum_{j=1}^{N} e^{i(\mathbf{k}-\mathbf{k}_1)\cdot\mathbf{r}_j}\right|^2 \\ &= \frac{1}{V^2}\int d^3x \int d^3x' e^{i(\mathbf{k}-\mathbf{k}_1)\cdot(\mathbf{x}-\mathbf{x}')}. \end{aligned} \tag{2.103}$$

In particular, for a spherical homogeneous distribution of atoms of radius R the cooperativity parameter is given by

$$\mu = \frac{9(\sin(k_0R) - k_0R\cos(k_0R))^2}{(k_0R)^6}. \tag{2.104}$$

3. Rydberg atoms

This chapter introduces the energy structure description of atoms paying particular attention to states with high principal quantum number n: Rydberg states. First, it will be shown how large the dipole moments of Rydberg atoms are compared to the ground state dipoles. As a consequence, Rydberg atoms are very sensitive to electric or magnetic fields as well as to room temperature Black Body Radiation (BBR). The effects on the Rydberg atom lifetime is discussed afterwards; also, a method on how to introduce the Rydberg atom decay into the OBE of Sec. 2.2 is presented. Finally, the chapter concludes by describing long-range dipole-dipole interactions between Rydberg atoms.

3.1. Dipole moment of Rydberg atoms

The dipole moment between two atomic states was introduced in Eq. (2.5). By means of the Wigner-Eckart theorem the angular part of the dipole moment can be factored out leaving only an integral over the radial part of the wavefunctions:

$$\mathcal{R}_{nL\to n'L'} = \int R_{nL}(r) r R_{n'L'}(r) r^2 \mathrm{d}r. \tag{3.1}$$

Here, the dipole selection rules (see Fig. 3.1) are assumed to be fulfilled. Then, it is easy to realize that the dipole moment is larger for neighboring states as their wavefunctions can be similar and even larger if one considers neighboring Rydberg states because $\langle r \rangle \propto n^2$. In ^{87}Rb, for example, $\mathcal{R}_{5S_{1/2}\to 5P_{3/2}} = -5.2ea_0$ compared to $\mathcal{R}_{5S_{1/2}\to 50P_{3/2}} = -0.0033ea_0$ and $\mathcal{R}_{50S_{1/2}\to 50P_{3/2}} = 2511ea_0$ with e the electron charge and a_0 the Bohr radius.

The energy difference between neighboring Rydberg states scales as n^{-3}. Consequently, together with the large dipole moment, Rydberg atoms turn out to be very sensitive to electric fields as their polarizability scales as n^7. Another consequence is

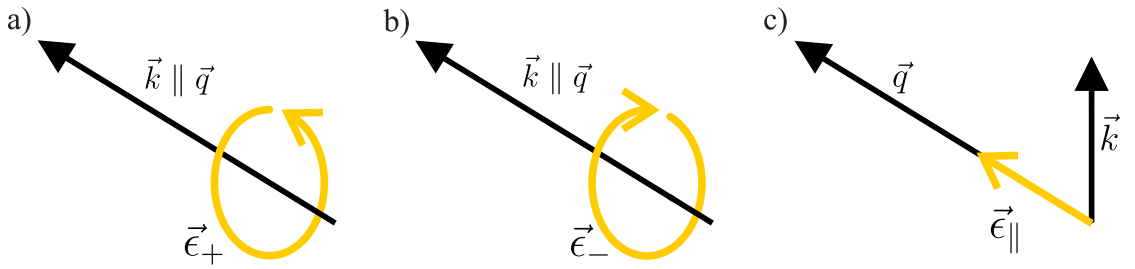

Figure 3.1.: An atomic transition from state i to k by absorption or emission of a photon follows (dipole) selection rules. The parity rule specifies that $\Delta\ell = \pm 1$ with the orbital angular momentum quantum number ℓ. Similarly, the total angular momentum F and J for the hyperfine and fine structure respectively must obey $\Delta F = 0, \pm 1$ and $\Delta J = 0, \pm 1$. Also, the angular momentum component m along the quantization axis $\vec{q}$ can be changed by $\Delta m = m_k - m_i = 0, \pm 1$. Overall, a dipole transition is named $\sigma_\pm$-transition ($\Delta m = \pm 1$ on absorption or $\Delta m = \mp 1$ on emission) or π-transition ($\Delta m = 0$) when the photon spin equals $\pm\hbar$ or averages 0, correspondingly. Light polarization for (a) σ_+ (b) σ_- and (c) π transitions are shown.

their large (small) transition wavelength (frequency). This makes them a convenient platform for superradiance as will be discussed more later but also it makes them susceptible to microwave photons present due to BBR at room temperature.

3.1.1. Total decay rate of a Rydberg state

In order to analyze the effects of BBR on the Rydberg atom lifetime one must first take into account all other atomic states beyond those that are coherently coupled by monochromatic light as discussed in Ch. 2. Then, the radiative lifetime τ_{nL} of a given state with quantum numbers n, L is the inverse of the total radiative decay rate [61]. This is obtained by summing the decay rates (see Eq. (2.23)) over all n', L' states with lower energy:

$$\tau_{nL}^{-1} = \sum_{n'L'} \Gamma_{nL,n'L'}. \tag{3.2}$$

Due to the $\omega^3_{nL,n'L'}$ factor in $\Gamma_{nL,n'L'}$, this sum will have its major contribution from transitions with higher frequencies (i.e. from transitions to ground states). In general, by using software packages like the Alkali Rydberg Calculator (ARC) [62]

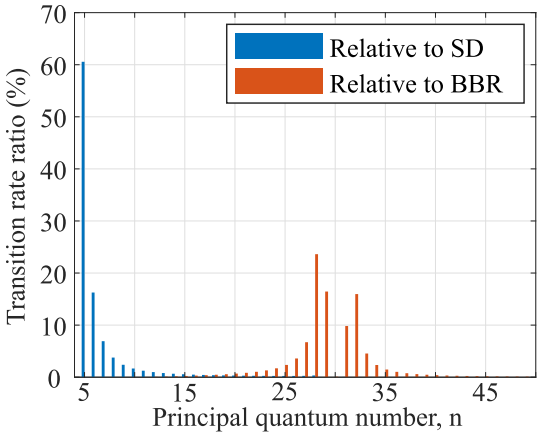

Figure 3.2.: Transition rates due to spontaneous decay (blue) and BBR (red) for the $30D_{5/2} \rightarrow nP_{3/2}, nF_{7/2}$ transitions of ^{87}Rb calculated using ARC. The rates are normalized to their respective total rate: $\tau^{-1}_{30D_{5/2}} = 38.4$ KHz and $\tau^{-1}_{BBR} = 17.4$ KHz. The software allows also to calculate that most (84%) of spontaneous decay transitions happen to $nP_{3/2}$ states while most (60%) of BBR induced transitions happen to $nF_{7/2}$ states.

the sum in Eq. 3.2 can be explicitly calculated as shown in Fig. 3.2.

It is known that the rate of stimulated emission (or absorption) of thermal photons due to BBR is proportional to the spontaneous decay rate of a given transition:

$$K_{nL,n'L'} = \frac{\Gamma_{nL,n'L'}}{e^{h\nu/k_BT} - 1}. \tag{3.3}$$

At room temperature ($T = 300K$) one obtains a thermal frequency of $\nu_T = k_BT/h \sim$ 6 THz or a corresponding wavelength of $48\mu m$. Transitions with frequencies smaller and up to this order can be achieved with Rydberg atoms and their transition rates to neighboring states are shown in Fig. 3.2. Then, similarly as with Eq. 3.2, the decay rate due to BBR from state nL is given by

$$\tau^{-1}_{BBR} = \sum_{n'} K_{nL,n'L'} \tag{3.4}$$

where, this time, n' can go up to infinity. Finally, the total decay rate is written as

$$\Gamma_{nL} = \tau^{-1}_{nL} + \tau^{-1}_{BBR}. \tag{3.5}$$

From the discussion above it is clear that in order to describe atomic decay from a Rydberg state down to the ground state one may have to consider several intermediate states; thus, decay channels. For this only the atomic populations and the dissipative part of Eq. (2.21) play a role. As a result, a set of well-known rate equations of the form [60]

$$\frac{dN_i}{dt} = -\Gamma_{ii}N_i + \sum_{j\neq i}\Gamma_{ij}N_j \tag{3.6}$$

are obtained. Here, recognizing that the set of quantum numbers for any atomic state is unique they have been replaced with a single index i. Then, N_i is the population of state i, Γ_{ij} is the decay rate from $j \to i$ [1] and Γ_{ii} is the total decay rate of state i. Finally, it is easy to realize that all of these rate equations can be written as

$$\frac{d\vec{N}}{dt} = A\vec{N} \tag{3.7}$$

with the vector $\vec{N} = [N_i]$ and the matrix $A = [\Gamma_{ij}]$ such that $\sum_i A_{ij} = 0$ which guarantees that there is no loss of atoms.

3.2. Superradiance with Rydberg atoms

Rydberg atoms offer a convenient platform to study superradiance in the context described in Ch. 2. Indeed, the transition wavelength between Rydberg states is comparable to the size of an atomic cloud. Nevertheless, at these highly excited states the enhanced decay rate is induced by BBR and not vacuum fluctuations as discussed above, unless the atomic system is in a cryogenic environment. Whichever the case, superradiance in mm-wave transitions has been thoroughly studied in the context of Rydberg-atom masers [63]; however, its decoherence due to dipole-dipole interaction has recently received greater attention [29]. This section aims to introduce and justify the theoretical description used to interpret the data presented in Sec. 4.

[1] The state j can be above or below i on the energy scale. This is because BBR stimulates not only emission but also absorption.

3.2.1. Decoherence by dipole-dipole interactions

The interaction potential between two two-level atoms separated by R is given in Eq. (2.95) as $\hat{\mathcal{H}}_{\mathrm{dd}} = \sum_{j,j'}^{N} \Omega_{jj'} \hat{\sigma}_j^\dagger \hat{\sigma}_{j'}$. At first order, notice that this Hamiltonian has no effect on the eigenenergies when both atoms are in the same state. Indeed, since an excitation is exchanged between the atoms, the mean value of $\hat{\mathcal{H}}_{\mathrm{dd}}$ taken over a pair state $|rr\rangle$ is always zero. Then, one needs to consider second-order perturbation theory in order to obtain the van der Waals energy shift E between a pair of atoms at distance R:

$$E = \frac{C_6}{R^6}. \tag{3.8}$$

It is in this context that effects like Rydberg blockade or Förster resonances, key for quantum computation using Rydberg atoms [64], are studied. Next, without going into much details, the two regimes with different scalings of R that originate are introduced.

In essence, the pair state under study $|rr\rangle = |r\rangle_1 |r\rangle_2$ interacts via $\hat{\mathcal{H}}_{dd}$ through different channels (i.e. other pair states) denoted as $|pq\rangle$ resembling a two-level system as depicted in Sec. 2. It was demonstrated in [65] that an avoided crossing indeed appears and, thus, reveals the two different regimes of the interaction potential: the resonant ($U_{dd} \propto R^{-3}$) regime and the van der Waals regime ($U_{dd} \propto R^{-6}$). One can define a critical distance R_c such that $\delta = C_3/R_c^3$ in order to draw a border between both regimes. Here, δ is the energy defect (i.e. the energy difference between two pair states) and $C_3 = \langle r| er |p\rangle \langle r| er |q\rangle / 4\pi\epsilon_0$.

In the present project the state $|r\rangle = 30D_{5/2}$ is considered. For second order effects, the most important interaction channels are to the pair states $\left|32P_{3/2}, 28F_{7/2}\right\rangle$ and $\left|31P_{3/2}, 29F_{7/2}\right\rangle$ with energy defects of 4.6 GHz and 6.4 GHz, respectively. Using ARC one can calculate the critical radii to be ~ 0.5 μm for both channels. As will be shown in Ch. 4, the usual interatomic separation used in this work is larger; therefore, the second order contribution is in the $1/R^6$ van der Waals regime.

The van der Waals interaction is then considered negligible compared to the first order contribution, i.e. resonant interaction between pair states $|rr'\rangle$ ($r \neq r'$). Approximating the ensemble as a continuum one finds out that the transition frequency will suffer a density dependent shift called the collective Lamb shift as a result from the exchange of virtual photons between atoms. This and other shifts due to resonant interactions has been studied in [66] where due to the large num-

ber of atoms considered a continuum approximation is done replacing the sum over different atom pairs by an integral. An alternative approach which accounts for the spatial distribution of atoms; thus, considers the position-dependent dipole-dipole (DD) interactions is the single excitation regime [67, 68, 69]. Here, the collective decay rate of the atomic ensemble is diminished by the rapid dephasing or decoherence caused by DD interactions on the light-induced dipole. This is revealed by the excited state inhomogeneous broadened linewidth. For a two-photon Rydberg excitation similar results are obtained [70, 71] but superradiance is not present.

The DD-induced frequency shift is also dependent on the atomic ensemble geometry and size relative to the transition wavelength. In a microscopic picture, the problem of including resonant interactions has been solved exactly for two and three atoms with specific triangular shapes in [72]. Here, it is remarked that in the case of two identical atoms Dicke superradiance is preserved and no decoherence takes place. They argue that, for fixed atomic dipole orientations, the interaction potential will be the same for both atoms; therefore, no matter how close they are the situation is unchanged: two (identical) two-level atoms with the same transition wavelength (as they experience the same potential, the energy shift is the same) will superradiantly decay. They later show that when the identical atoms premise is lifted (e.g. different transition wavelengths or more than two atoms), the interaction potential between them suppresses superradiance. Numerically the problem has been approached with up to five randomly distributed atoms in [73] and for a linear array [74]. In any case, it is concluded that dipole-dipole interactions diminish the superradiant decay rate. Further insight is given at the conclusions of [72] where it is argued that a consequence of pair interactions is the coupling of subradiant states and the lack of freedom to permute the atom positions without altering the system (i.e. the frequency shifts experienced by different atom pairs). The latter, is said, render the atoms to be nonequivalent.

A large step forward on the understanding of this problem was done recently in [27]. There, a numerical method is introduced that allows to track the problem for hundreds of randomly distributed atoms. As a result, it is shown that the superradiant decay rate is not only diminished as the atomic ensemble is less diluted but that there is a peak decay rate. This point draws a line in atomic density: on one hand, interatomic distance is short making the dephasing of superradiance to be dominated by dipole-dipole interactions; on the other hand, the atomic ensemble

is diluted enough for the dominant role to be replaced by finite-size effects as in [60] which states that atoms will start to radiate incoherently as the distance between them grows larger than their transition wavelength. Furthermore, the competition of two superradiant decay channels is studied and the complex interplay between their transition parameters and the number of atoms is discussed.

From another perspective, superradiance can be pictured as the result of interference between different decay paths [75]. Indeed, it is shown that tracking the emission of a single photon from a symmetric Dicke state multiple indistinguishable decay paths appear: a pair of atoms sharing an excitation project the system into a single state but is impossible to discriminate which atom emitted (two decay paths). As a result, the radiated intensity is greater than for independent radiating dipoles with the difference given by interference terms between pairs of decay paths. In fact, the points of maximum radiation are shown to follow

$$I_{max} = I_{\text{inc}} + \mathcal{P}_{\text{no.}}^{\text{pair}} \left|f\right\rangle_{\text{no.}} \mathcal{N} \tag{3.9}$$

where I_{inc} is the incoherent contribution, $\mathcal{N}$ is the squared normalization constant of the Dicke state while $\mathcal{P}_{\text{no.}}^{\text{pair}}$ and $\left|f\right\rangle_{\text{no.}}$ are the number of interfering decay path pairs and final states after a single photon emission, respectively.

For the case of superradiant decay, the first term (I_{inc}) corresponds to N_e and the second term ($\mathcal{P}_{\text{no.}}^{\text{pair}} \left|f\right\rangle_{\text{no.}} \mathcal{N}$) to $N_e N_g$ which then results in Dicke's result $N_e(N_g+1)$. Notice that it is the second term that is affected by the cooperativity or shape parameter μ for an extended atomic ensemble introduced in Sec. 2.4.3. This is not surprising since μ controls the amplitude of a diffraction pattern formed from the scattered photons [60]. On the other hand, the Hamiltonian $\hat{\mathcal{H}}_{\text{dd}}$ (see Eq. (2.93)) makes pairs of atoms interact via exchange of excitation $\left|r_1\right\rangle_i \left|r_2\right\rangle_j \leftrightarrow \left|r_2\right\rangle_i \left|r_1\right\rangle_j$. Then, pairs of atoms that are coupled by $\hat{\mathcal{H}}_{\text{dd}}$ will be dephased relative to other not so strongly coupled pairs. This would effectively reduce the second term of Eq. (3.9) since the interference between pairs of decay paths will be dephased. Decoherence or dephasing by dipole-dipole interactions must also compete with other decohering sources that inhomogeneously broadens the Rydberg state linewidth γ_r [76]. In order to account for this competition a critical radius r_c is defined as $\Omega_{ij} = C_3/r_c^3 = \gamma_r$ where both rates are equal. This means that if two atoms are closer than r_c the dephasing rate due to Ω_{ij} is faster than any other one; thus, a density dependent

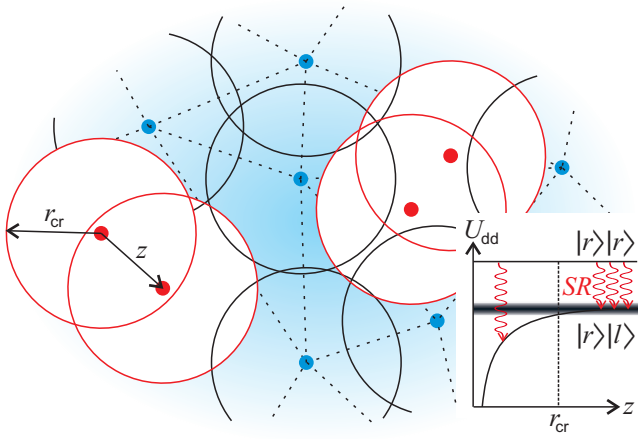

Figure 3.3.: Representation of a set of interacting Rydberg atoms. Superradiant decay from state $|r\rangle$ to a neighboring Rydberg state $|l\rangle$ is possible as long as they form a coherent many-body state: a Dicke state (in blue, dashed lines, shaded region). If the distance z to the next neighbor is smaller than the critical radius r_{cr} (in red, unshaded) the transition is tuned out of resonance due to the dipole-dipole interaction potential $U_{\mathrm{dd}}(z)$ making those atoms unable to link to the Dicke state. Effectively, less atoms take part in the superradiant decay.

decoherence of superradiance should be observed.

We aim to introduce a density dependent factor β that alongside μ reduces superradiance. Although a formal derivation is not presented, β contains the effects of resonant interactions on superradiance explained above. Since the typical ensemble has randomly distributed atoms, the nearest neighbor probability distribution $W(r) = 4\pi r^2 \rho e^{-\frac{4}{3}\pi\rho r^3}$ is used to describe the number of atom pairs at distance r instead of considering the exact geometry of the atomic positions. In particular, given the atomic density ρ, it is most likely that the nearest neighbor of any atom is at a distance $r_{max} = (2\pi\rho)^{-1/3}$.

Next, it is necessary to calculate the ratio of atom pairs $P(r_c)$ separated at a distance smaller than r_c. This is obtained by integrating $W(r)$:

$$P(r_c) = 1 - e^{-\frac{4}{3}\pi\rho r_c^3}. \tag{3.10}$$

It is these atom pairs that dephase superradiance by reducing the number of interfering decay paths. We are then left with $1 - P(r_c) = \beta$ as the ratio of atom

pairs effectively taking part in the superradiant decay without dephasing due to dipole-dipole interactions (see Fig. 3.3).

4. Optical setups and measurements

The present chapter describes the experimental work done for the realization of this thesis. In regard of the optical setups, major emphasis is given to the blue laser source and the science cavity setup as they are key elements for the fulfillment of this project. Nevertheless, the MOT setup (based on the previous one by Mathias Mildner) was completely rebuilt from the ground up mainly in order to install cat-eye lasers and Acousto-Optical Modulators (AOM) in replacement of all lasers and shutters, respectively. Afterwards, experimental evidence of the phenomena discussed in Ch. 2 is shown. The chapter is finished by showing the main results giving the title for this thesis: the use of an optical cavity transmission as detector of Rydberg dynamics.

4.1. The MOT setup

In this thesis the Alkali isotope ^{87}Rb is the atom of interest. The single valence electron of Rb has the lowest energy in the ground state $5^2S_{1/2}$. In particular, the D2 transition structure consists of two ($F = 1,\ 2$) and four ($F = 0,\ 1,\ 2,\ 3$) hyperfine levels corresponding to the $5^2S_{1/2}$ and $5^2P_{3/2}$ states, respectively. Here, the ground ($|g\rangle$) and excited ($|e\rangle$) states introduced in the previous chapters are now defined as the $5^2S_{1/2}F = 2$ and $5^2P_{3/2}F = 3$ hyperfine states, respectively. Furthermore, each of these constitute a manifold of degenerate (in the absence of magnetic field) states: the Zeeman states. In App. A it is shown how to take these manifolds into account for a cavity QED system as discussed in Sec. 2.3.2. Usually an average over these manifolds is considered throughout this thesis.

In this context, the MOT setup consists of three lasers: the "reference", the "MOT" and the "Repump" (Rp) laser. The last two laser's frequencies (ν_{MOT} and ν_{Rp}) are stabilized relative to the reference laser frequency (ν_r) which is, in turn, stabilized to ^{87}Rb by saturation spectroscopy. Specifically, to the crossover between

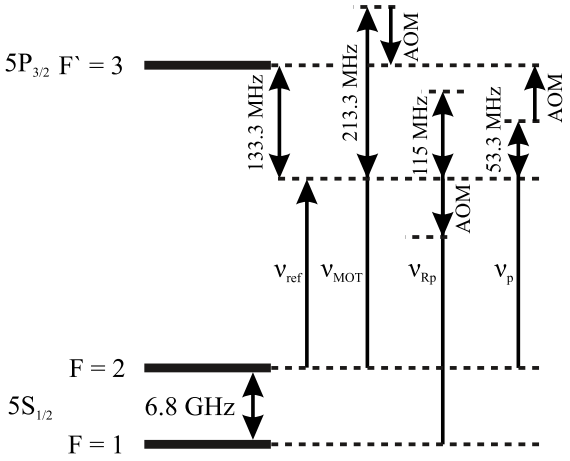

Figure 4.1.: The reference laser frequency is fixed to 133.3 MHz red detuned to the $F = 2 \rightarrow F' = 3$ transition of ^{87}Rb. All other laser frequencies are controlled relative to the reference frequency. Finally, an AOM controls the optical power of each laser and shifts their frequencies by a constant 80 MHz.

the $F = 2 \rightarrow F' = 2$ and $F = 2 \rightarrow F' = 3$ transitions of the D2 line. Therefore, it has a red detuning of 133.3 MHz relative to the atomic transition of interest (see Fig. 4.1). The choice of stabilizing the laser to this crossover was made because its error signal, obtained using a frequency-modulation (FM) technique, has the largest signal-to-noise ratio.

The stabilization procedure for the other lasers is by a "beat lock". The RF signal (beat) resulting by superposing light from the reference laser and another one (e.g. MOT or Rp) has a frequency equal to the difference between both frequencies ($\nu_{RF} = |\nu_r - \nu_{MOT,Rp}|$). Then, in order to stabilize ν_r, an error signal is generated by means of a linear frequency-to-voltage (f/u) converter [1] with a dynamic range of 100 MHz and a bandwidth from DC-1576 MHz. In particular, the RF signal obtained from the Rp laser is beyond this bandwidth (see Fig. 4.1). Thus, after detection by a fast photodiode, the signal is first mixed with an RF oscillator at 6896.4 MHz and then fed to an f/u converter [2].

The MOT laser optical power needs to be controlled. First, it is amplified by a

[1] See "Frequenzstabilisierer für Dioden-Laser" Version-3 Nr. 6256 in the electronic workshop.

[2] The fast photodiode used is a 10GbE SFP+ SR Transceiver model TAS-A2NH1-P11 from FormericaOE and the mixer is a MiniCircuits ZX05-153-S+.

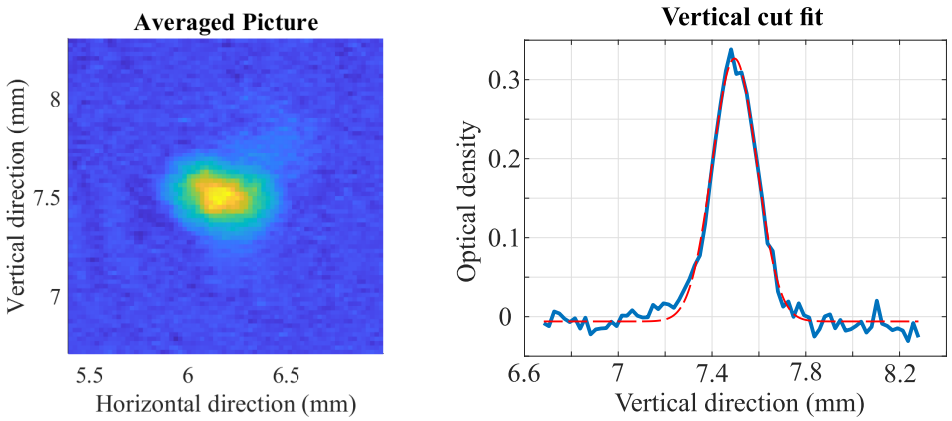

Figure 4.2.: An ensemble of atoms is loaded into a MOT and released after a short flight time ($\sim$ 100 μs) to be used in the experiment. A transversal cut to the image allows to measure the cloud radius to be $\sim$ 0.25 mm containing around 1 million atoms. At the end, only around 10^4 atoms are located inside the cavity mode. A larger cloud and longer flight time were used to measure the temperature to be $\sim 30\mu$K.

tapered amplifier [3] reaching $\sim$ 500 mW. Then, it passes through an AOM operating at 80 MHz with an RF power controlled by a Voltage Controlled Attenuator. The -1 order beam is then coupled into a single mode fiber. On the other hand, the Rp laser is not amplified ($\sim$ 5 mW) and only passes through an AOM also operating at 80 MHz but at a constant RF power. The +1 order beam is then coupled into a single mode fiber.

In the present project one pair of coils separated by a distance of 42 mm with an inner and outer radius of 22 mm and 56 mm and 6 mm width is used. The base pressure reached in the chamber is 2×10^{-10} mbar. There, the MOT beams have a beam waist of 9 mm and an optical power of 9 mW each compared to the 2.5 mm and 5 mW of the Rp beam. Additionally, two ^{87}Rb dispensers from SAES Getters are used as atomic source and are usually driven between three and five amperes. Furthermore, a copper rod is positioned in front of each dispenser in order to avoid ejecting hot atoms directly into the MOT position. The experimental cycle has a duration of 15 s and starts by turning on the dispensers for 6 s. After the dispensers are off, the MOT keeps loading atoms for 3 more seconds before the current running through the coils is turned off. At this moment, a mollasses phase starts lasting

[3] BoosTA from Toptica

for 10 ms: the optical power of the cooling beams is reduced to $\sim$ 30% and the frequency is changed to reach a detuning of $\Delta_{MOT} = -65$ MHz. This allows us to obtain a typical cloud temperature of $T \sim 30$ μK.

In order to measure the number of atoms and the cloud temperature, absorption imaging is used. For this, part of the light ($\sim$ 1 mW) from the reference laser passes through an AOM running at 133.3 MHz making it resonant to the atomic transition. Additionally, a lens of 75 mm focal length is used for imaging the MOT onto a CCD camera (Sony XC56) with magnification 1:3. The image taken has 640×480 pixels and 8-bit depth. A typical picture taken using this method is shown in Fig. 4.2. The atom number is measured by summing the optical density across all pixels. Also, a vertical cut along the peak OD is shown together with the lorentzian curve used to extract the cloud radius and temperature.

4.2. The blue laser setup

In order to transfer atoms into a certain Rydberg state a two-photon transition is performed. To make this possible a new laser setup with the appropriate wavelength had to be designed and built. This section is dedicated to describe this setup. First of all, notice that the only dipole allowed transitions starting from the $5^2P_{3/2}$ state are to the $nS_{1/2}$, $nD_{3/2}$ or $nD_{5/2}$ Rydberg states. The corresponding transition wavelength is 480 nm. This wavelength is produced by frequency doubling a laser of 960 nm and, afterwards, it is precisely tuned using EIT spectroscopy on a Rb cell so as to couple a particular Rydberg state.

4.2.1. Frequency doubling cavity

Second harmonic generation (SHG) or frequency doubling is possible due to the $\chi^{(2)}$ non-linearity of a material. Two fields with different wavelengths will then propagate through the crystal: the pump (λ) and the second harmonic ($\lambda/2$). For the wavelengths considered in this thesis (960 and 480 nm) an LiB_3O_5 (LBO) crystal is commonly used. This is a biaxial type of crystal meaning that the refractive indices along its principal axes (i.e. x, y, z) are all different. In practice, however, nonlinear effects in this type of crystals are evaluated or considered for light propagating in the principal planes only.

Type-I SHG, in LBO, is possible only for wavevectors in the xy or xz principal planes [77]. In particular, the xy plane is used in this thesis as it is the one offered by the crystal manufacturer EKSMA. Then, the pump field is linearly polarized along z while the second harmonic field is linearly polarized in the xy-plane with an angle φ relative to the x axis. In order for SHG to be efficient, a phase matching condition must be fulfilled where the refractive index for both fields are equal. For critical phase matching, the angle φ is varied at a working temperature T (see Fig. 4.3(a)) until the phase matching condition is reached at $\varphi = \theta_{\mathrm{pm}}$:

$$\theta_{\mathrm{pm}} = \mathrm{asin}\left(\sqrt{\frac{\frac{1}{\eta_{z\mathrm{p}}^2} - \frac{1}{\eta_{y\mathrm{SH}}^2}}{\frac{1}{\eta_{x\mathrm{SH}}^2} - \frac{1}{\eta_{y\mathrm{SH}}^2}}}\right). \tag{4.1}$$

The temperature dependence of the refractive indexes correspond to those given in [78]. On the other hand, non-critical phase matching requires temperature to be changed. However, a temperature well above 100 °C is required. For this project, critical phase matching is chosen in order to avoid temperature perturbations to the optical cavity in which the LBO crystal is located. Then, a working temperature of 25°C is chosen since it is closer to room temperature. Consequently, the manufacturer was required to prepare the crystal at a cut angle $\phi = 18.4°$ (see Fig. 4.3(b)) so that, in practice, we have normal incidence of light on the crystal. Additionally, Fig. 4.3(b) shows how the working temperature needs to be changed in order to excite different Rydberg states (i.e. change the pump wavelength). Finally, to minimize back reflection, antireflection coatings for 960 nm were deposited on the crystal faces of dimensions 3×3 mm.

Further parameters to take into account for the efficiency of SHG are the ones characterizing the fundamental Gaussian beam such as power and beam waist as well as the crystal length. The importance of the former is straightforward to justify as the power of the frequency-doubled field P_{SHG} is given by

$$P_{SHG} = \gamma P_{in}^2 \tag{4.2}$$

where P_{in} is the power of the fundamental field and γ is the crystal conversion efficiency [79]. In our case, high light powers are achieved by using a TA Pro from Toptica which can deliver at most 2 W with a wavelength range from 955 up to

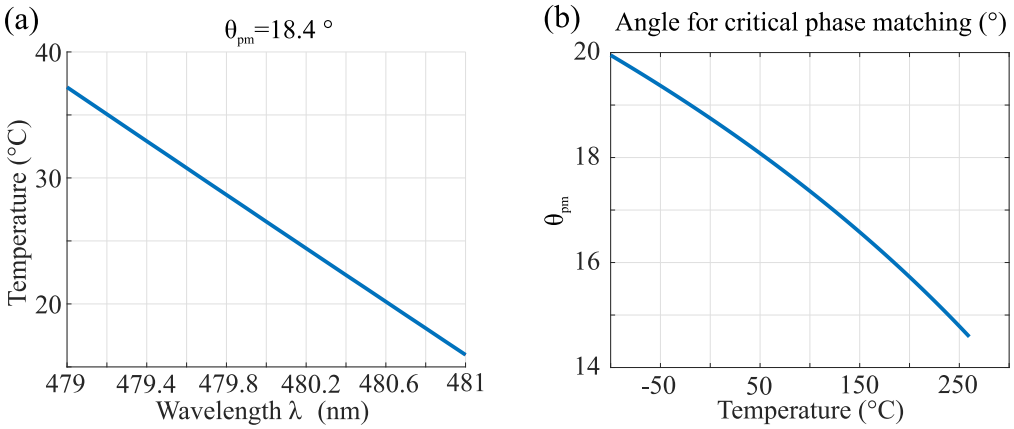

Figure 4.3.: The phase matching condition for SHG is fulfilled at the angle $\varphi = \theta_{\mathrm{pm}}$. At this angle both, pump and second harmonic fields, travel through the crystal with the same refractive index. Therefore, θ_{pm} depends on temperature.

980 nm controlled by a diffraction grating. Moreover, the maximum possible P_{in}, though limited by the LBO damage threshold, is enhanced by putting the crystal inside a resonator mode. At the same time, the cavity geometry will define the beam waist of the fundamental field which, in principle, needs to be close to the optimal waist defined by the crystal length [80]. Considering a crystal length $\ell = 15$ mm (offered by the manufacturer) and following [81] a focusing parameter $f = \ell/b$ where $b = w_0^2 k_p$ is the confocal parameter with w_0 and k_p are the pump beam waist and wave number, respectively. In [81] an optimum focusing parameter $\zeta_m(B)$ is defined which depends on the double refraction parameter $B = \rho\frac{\ell k_p}{2}$ where ρ is the walk-off angle (see Fig. 4.4) which is the angle between the residual pump beam and the second harmonic beam. As a result, the optimum beam waist is estimated to be $w_0 = 38$ μm.

The resonator used is a bow tie type cavity consisting of four mirrors [4]: 2 concave and 2 plane folded as shown in Fig. 4.5. The mirrors sit on an Invar 36 plate of 230 × 160 mm and 30 mm thickness surrounded by a plastic cover. Also, in order to control the cavity length, one of the plane mirrors is glued to a piezo transducer [5] while the crystal is located within the short space of length $L_1 = 65$

[4]Highly reflective ($R > 99.9\%$) at 960 nm and highly transmissive ($R < 2.5\%$) at 480 nm from Laseroptik.
[5]P-010.00H PICA from PI Ceramic.

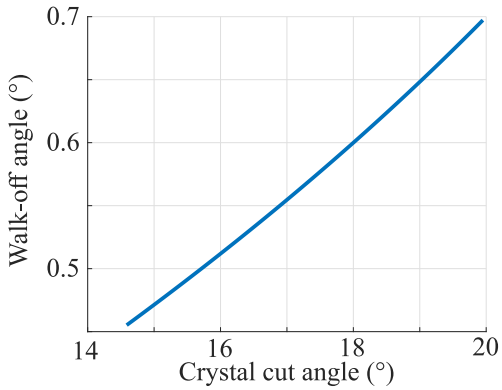

Figure 4.4.: The walkoff angle as a function of the phase matching angle θ_{pm}. The second harmonic beam is tilted by an amount given by the walkoff angle ρ relative to the pump beam.

mm between the curved mirrors. In total, the roundtrip length $L_{rt} = 215$ mm but, since the crystal refractive $\eta_\phi = 1.58$ must be accounted for the applicable length, the resulting $FSR = 1.34$ GHz. Also, the relatively small folding angle $\theta = 15°$ is selected to avoid a too large ellipticity of the resonator mode at the center of the crystal. Indeed, the expected transversal and sagital beam waists are $w_0^x = 41.9\ \mu m$ and $w_0^y = 43.2\ \mu m$, respectively.

Inside the cavity, P_{in} in Eq. 4.2 must be replaced by the intracavity power P_{cav}. The latter, in the ideal case scenario, is amplified by the cavity enhancement Ξ discussed in Ch. 2. In reality though the present case is non ideal: mirrors scatter as well as absorb (i.e. $R+T \neq 1$) and, furthermore, the input beam may be considered to not perfectly match the cavity mode. In any case, the phase matching condition guarantees the largest enhancement for a given round-trip loss. Then, following the crystal specifications and mirror nominal reflectivity of 99.9% (in practice, can be higher) given by the manufacturers, under perfect phase matching the incoupler transmission must equal 0.5% which would result in $\mathcal{F} = 603$ and $\Xi = 192$. However, preventing for possible higher round-trip losses [6], the incoupler reflectivity is chosen to be $R_{in} = 98.5\%$ below the optimum value. This defines a lower bound for $\mathcal{F} = 208$ and $\Xi = 66$ under perfect phase matching.

The characterization of the cavity was estimated experimentally by driving it with

[6] Smaller than nominal mirror reflectivities due to a higher scattering rate (e.g. dust on the mirrors), pump depletion due to the SHG and crystal degradation.

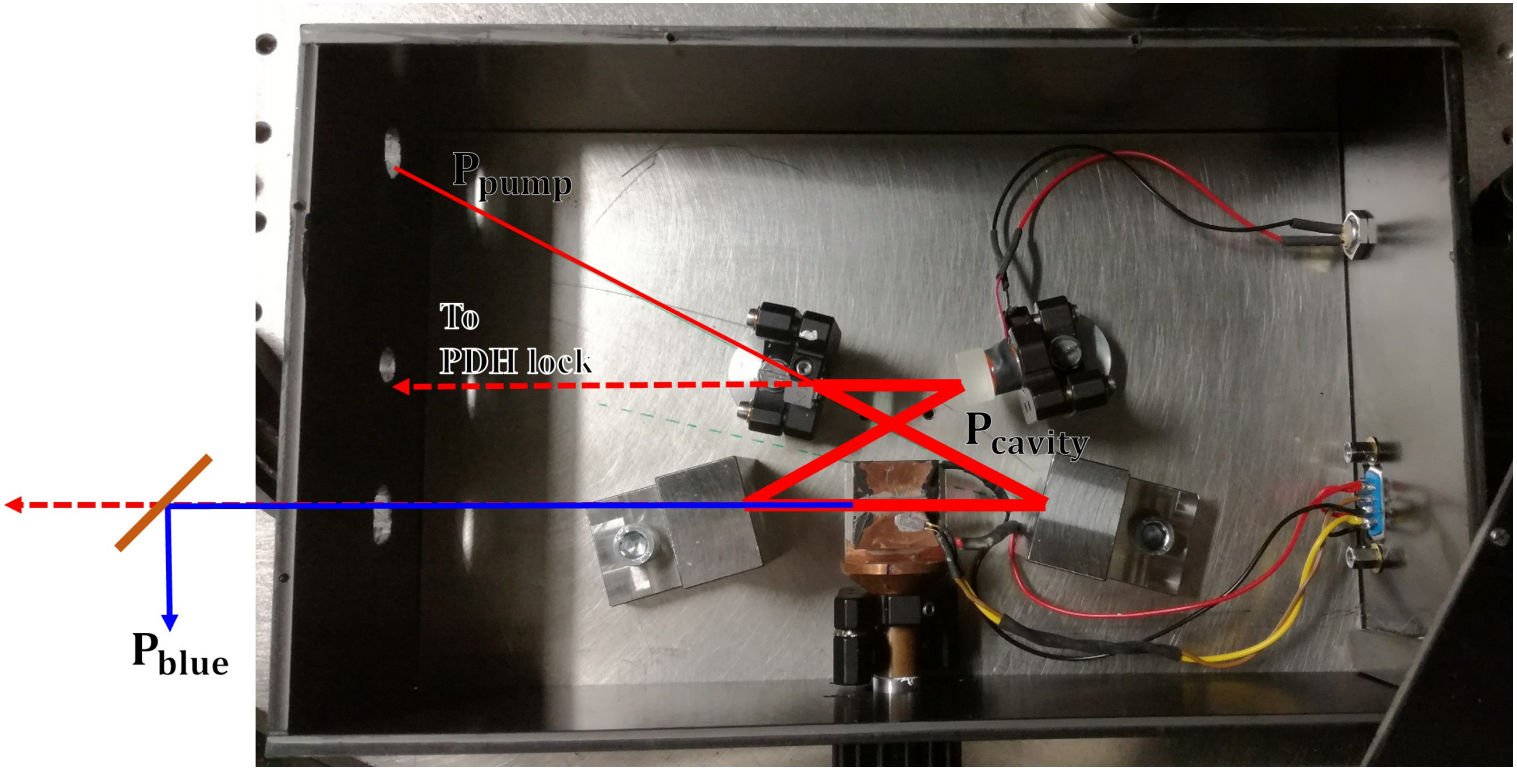

Figure 4.5.: A bow tie cavity is used to enhance light of 960 nm that is then frequency doubled by type-I SHG using an LBO crystal. The cavity consists of four mirrors on top of an Invar plate: two curved mirrors are fixed to the plate while the other two mirrors are plane and can be tilted. One of the plane mirrors is glued to a piezo in order to control the cavity length. The LBO crystal of 15 mm length is located between the curved mirrors where the beam waist is smallest.

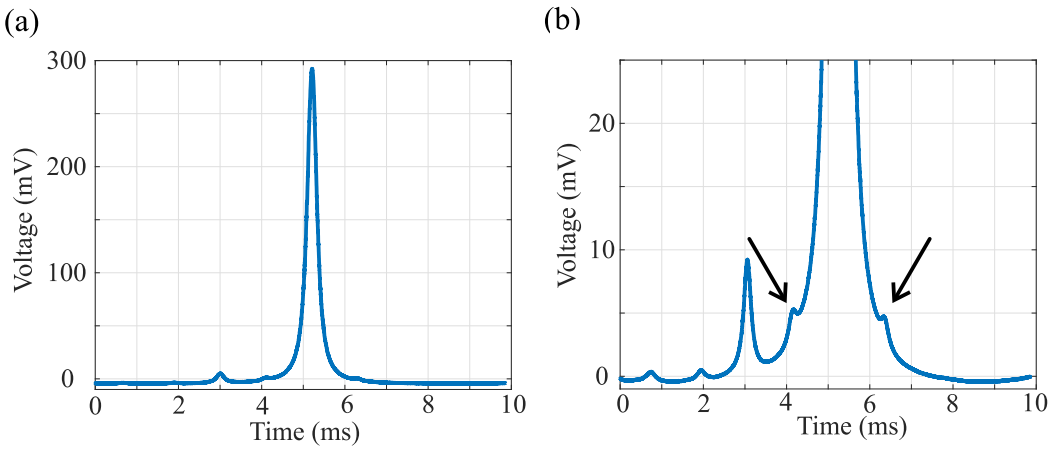

Figure 4.6.: The piezo of the bowtie cavity is ramped across the fundamental mode resonance peak in 10 ms. (a) From this peak one can estimate the FWHM from its definition. (b) The same peak with a smaller scale allows to observe more clearly the pair of small peaks corresponding to the 20 MHz modulation of the laser frequency. These peaks allow to calibrate the time axis to frequency units.

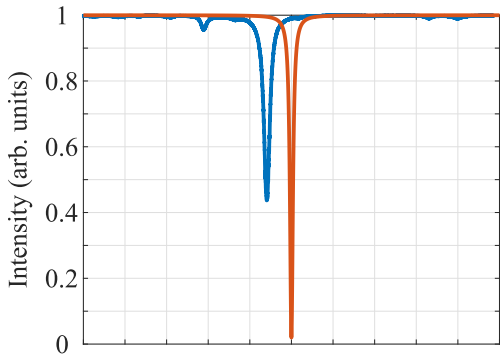

Figure 4.7.: Measured (blue) and expected (orange) spectrum of the bowtie cavity on reflection. The difference between them is argued to be due to imperfect mode-matching. An effective cavity enhancement can then be calculated.

the lowest possible power so as to avoid heating effects and pump depletion. The measured resonance peak of the fundamental mode is shown in Fig. 4.6 where the inset is a zoom to better show the calibration peaks. These are part of the PDH setup to control the cavity length and their frequency difference is a known constant parameter. Therefore, it is used as frequency calibration of the time axis. In this way, the resonance peak was measured to have a $FWHM = 5.7$ MHz corresponding to $\mathcal{F} = 237$ which would, in turn, correspond to $\Xi = 87$ by virtue of Eq. 2.67. However, the expected reflected spectrum is compared with the measured one and shown in Fig. 4.7. The higher reflected power measured is assumed to be due to imperfect mode matching [7]; therefore, an effective enhancement is calculated to be $\Xi = \frac{1-I_{exp}}{1-I_{th}} = 50$.

The SHG efficiency is also estimated experimentally. For this, the outcoupling mirror transmissivity was previously measured to be 0.01%. Then, by measuring the transmitted power out of this mirror, P_{cav} is estimated. However, since 480 nm light is simultaneously outputted, a dichroic mirror (DMLP650 from Thorlabs) is used to separate both wavelengths. Furthermore, the reflectivity and transmissivity of this dichroic mirror is also measured at both wavelengths allowing a more precise value of P_{cav} and P_{SHG} to be estimated. The resulting curve obtained as a function of intracavity power is shown in Fig. 4.8 together with a fit to Eq. 4.2. From it the conversion efficiency is estimated to be $\gamma = (1.09 \pm 0.43) \times 10^{-4}\ W^{-1}$. At higher values of P_{cav}, its depletion is taken into account by fitting a line which resulting in a proportionality factor of 1.3×10^{-2} between P_{cav} and P_{SHG}.

Due to the high optical powers reached inside the cavity, the effects of temperature drifts on the optical components produce a non linear effect on the cavity spectrum. Indeed, it was observed that the resonance peak is pushed farther away the greater P_{cav} is; thus, making it difficult for the servo loop to stabilize the cavity length. In the context of ring nanocavities, Ref. [82] shows that this non linear effect is due to thermal expansion and to the dependence of refractive index on temperature. Nevertheless, they also show that the frequency pulling can be engineered by calibrating the thermal dissipation response between the nanocavity and its surroundings. In our particular case, taking the crystal out of the cavity this effect is not seen meaning

[7] This can be considered to be a good approximation because the beam profile out of the TA Pro is not perfectly gaussian and, evenmore, its ellipticity is not shaped before the cavity: a single lens is used.

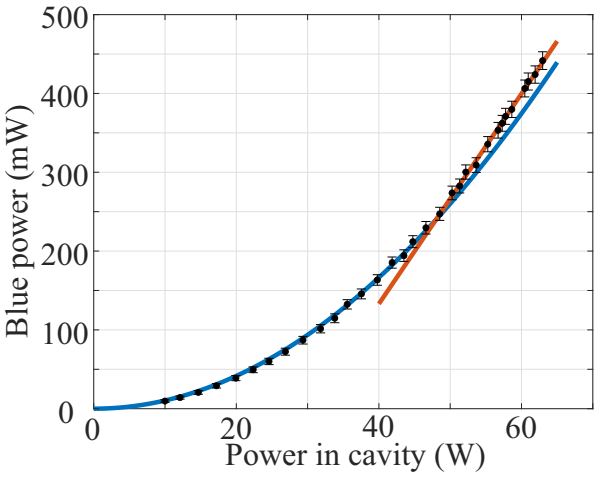

Figure 4.8.: Generated optical power by SHG at 480 nm dependence with the intracavity power P_{cav}. A quadratic function is fitted to this data in order to estimate the conversion efficiency. A linear fit is used for the higher power cases in order to account for pump depletion.

that the leading role is taken by the crystal on this matter.

Unfortunately, LBO thermal response is slow (see App. B) meaning that heat can accumulate for a long time inside the crystal before dissipating to the outside which finally results in greater thermal expansion. Therefore, the crystal thermal coupling to its surroundings had to be engineered and the final design that worked best is shown in Fig. 4.9. The crystal is surrounded by a copper plate acting as a heatsink with its temperature controlled by a Peltier element. A silver heat paste of 50 μm thickness and a thermal conductivity of 10 $W/m \cdot K$ is used to join the crystal with the copper plate. Then, the other side of the Peltier element is connected to another heatsink which is conveniently manufactured to fit into a mirror mount [8] allowing us at the same time to finely adjust the crystal orientation.

4.2.2. EIT spectroscopy on a Rb cell

In order to tune the wavelength of the coupling laser to a particular Rydberg state EIT spectroscopy is performed on a Rb cell. As explained in a previous chapter, at two-photon resonance the lower transition shows a transparency window which can be much smaller than Γ_e. This property can then be exploited by using the

[8] KS05 from Thorlabs

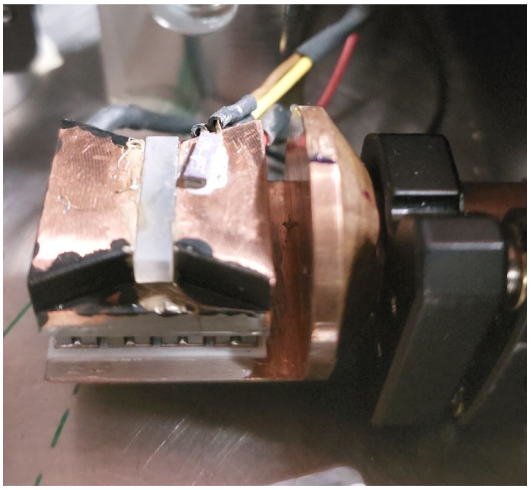

Figure 4.9.: A Peltier element is glued to copper devices. One is used as heatsink for the Peltier element as well as to be mounted into a mirror mount in order to tilt and rotate the crystal. The other, smaller, copper device serves as heatsink for the crystal. A silver heat paste is used to join the crystal with this device.

PDH method to generate a very steep error signal out of this resonance peak. An example is shown in Fig. 4.10 together with the optical setup used. First, the elliptical beam out of the bow tie cavity is collimated with a lens of focal length $f = 200$ mm and then transformed to a circular profile of beam waist $w_0 = 1$ mm by using an anamorphic prism pair. At this point the optical power for this beam is ~ 300 mW. On the other hand, the Rb cell is heated at 25 °C by winding wire around it with a constant current. The wire is folded so that current flows in both directions; thus, magnetic fields are cancelled. The cell is positioned between two dichroic mirrors that allow the probe and coupling beams to counter propagate along the same path through the cell. The probe beam comes directly from the reference laser after passing through an EOM [9] driven at 19.65 MHz and is finally detected by an avalanche photodiode [10].

With the aid of a wavemeter the lasing frequency of the TA Pro is measured while observing the EIT peaks. The observed peaks can then be labeled to a Rydberg state by following Ref. [83]. Nevertheless, since $\Delta_p = -133.3$ MHz, the coupling frequency must be blue detuned in order to fulfill the two-photon resonance condi-

[9] PM7-NIR_20 from QUBIG.
[10] APD130A/M from Thorlabs.

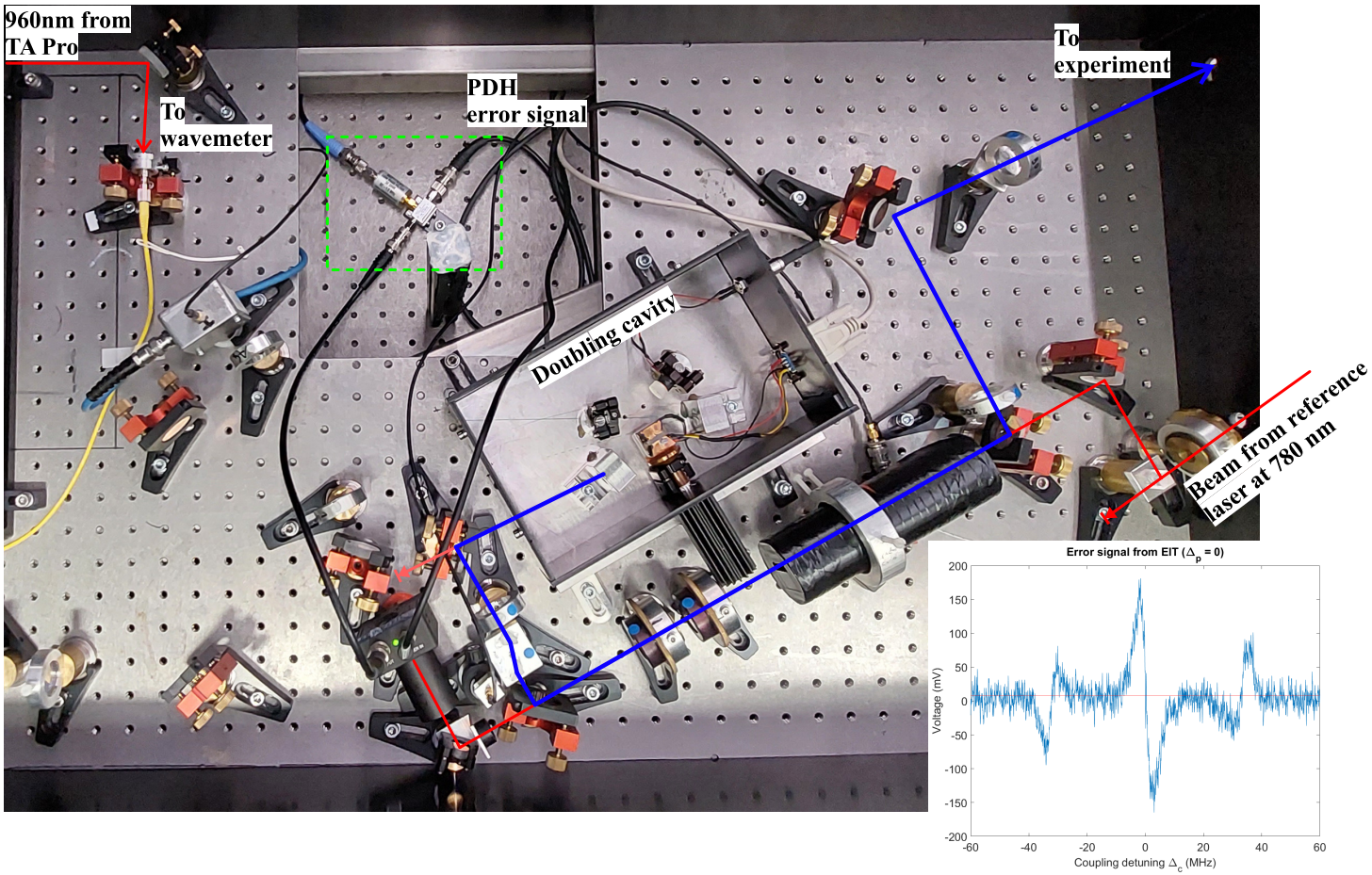

Figure 4.10.: Optical setup for the SHG of 480 nm light. The beam traces highlighted correspond to the setup for EIT spectroscopy on a Rb cell. Rydberg transition is performed via two-photon excitation. Probe light is frequency modulated at 19.61 MHz and detected by an APD. The dispersion curve from the transparency peak due to EIT (lower right corner) is then generated with a mixer found inside the green dashed box.

tion. Furthermore, the Doppler shifts must be accounted for because both beams have different wavelengths. Indeed, there is a particular velocity class with speed $v = \Delta_p/k_p$ that makes the photon to be resonant with the lower atomic transition. Then, in order to fulfill the two-photon resonance condition, the coupling frequency ω_c must also have a detuning $\Delta_c = k_c v$ which equates to $\Delta_c = (\lambda_p/\lambda_c)\Delta_p$. In our particular case, the coupling beam would then have a frequency such that $\Delta_c = 1.62 \times 133.3 = 216$ MHz. Finally, a telescope is used to focus the beam on an AOM which is driven at this frequency. As a result, the coupling field is set to be resonant with the upper atomic transition and, at the same time, its power is controlled.

4.3. The science cavity setup

A picture of the cavity used in this thesis is shown in Fig. 4.11. It is a confocal cavity with mirrors of a radius of curvature $r_c = 50$ mm and equal nominal reflectivity $R = 98.5\%$. Consequently, the space between the mirrors has a length of 50 mm corresponding to a $FSR = 3$ GHz. Each, odd and even transverse modes are degenerate and separated by exactly $FSR/2$. In order to control the cavity frequency, a cylindrical piezo of low capacitance (10 nF) is glued between one of the mirrors and its mount. On the other hand, the second mirror is directly glued to its mount; however, both mounts are screwed to the same stainless steel bar of 240×30 mm and 7 mm thickness. A circular hole of 20 mm radius is made in the center between the mirrors to allow the propagation of the MOT beams. In addition, two plane mirrors are located outside the cavity right next to each curved mirror. These fold the incoupling and transmitted beam to make them enter and exit the vacuum chamber. Finally, as seen in Fig. 4.11 the steel bar sits on the lower MOT coil by means of three steel spacers.

In order to control the cavity detuning δ_c (i.e. ω_{cav}) the PDH method is applied. For this, a laser of 786 nm ("lock laser") is installed. This wavelength was chosen so as to be off resonant to any atomic transition in ^{87}Rb as well as for convenience since the diode is easily available. This choice though brings the difficulty that it is not possible to stabilize this laser by using spectroscopy. Thus, an alternative method is used which involves incorporating a highly stable cavity made out of Ultra Low

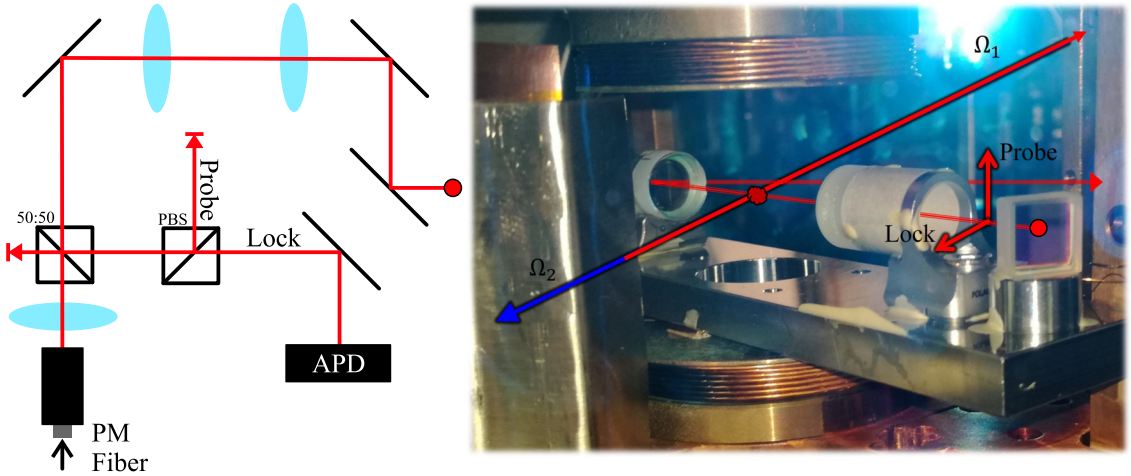

Figure 4.11.: Standing wave cavity used in this project. The beam out of a fiber containing the "lock" and "probe" light is shaped to mode-match the cavity. Reflected light is accessed by means of a beam splitter and both wavelengths are separated with a polarizing cube so that only lock light is detected by an APD. The atomic cloud is situated inside the cavity mode and is driven by two counterpropagating beams crossing the cavity transversally.

Expansion (ULE) glass to which the lock laser frequency is stabilized.

In order to have control over the cavity frequency, part of the lock laser light is coupled into a fiber EOM driven by a 2.1 GHz signal generator [11]. As a result, sidebands are created whose frequency distance can be controlled by almost a full FSR by tuning the signal generator frequency. Another "probe" field resonant to the atomic transition is simultaneously coupled into the cavity (see Fig. 4.12). Monitoring the cavity transmission while ramping its piezoelement one can simultaneously observe the probe resonance peak and one of the lock laser's sidebands PDH signal. By changing the EOM driving frequency one can displace the error signal closely on top of the probe resonance peak. Furthermore, to facilitate the discrimination of lock light in transmission, the chosen sideband drives the TEM_{01} mode while the probe drives the fundamental TEM_{00} mode. The sideband frequency can then be finely tuned by closing the feedback control loop and ramping the full range of the probe field frequency in 1.5 ms. Note that, from a previous measurement, the time axis is known as a function of probe detuning $\delta_p = \omega_p - \omega_{ge}$. Then, a least-square

[11] NIR-MX800-LN from IxBlue and Rigol DSG821

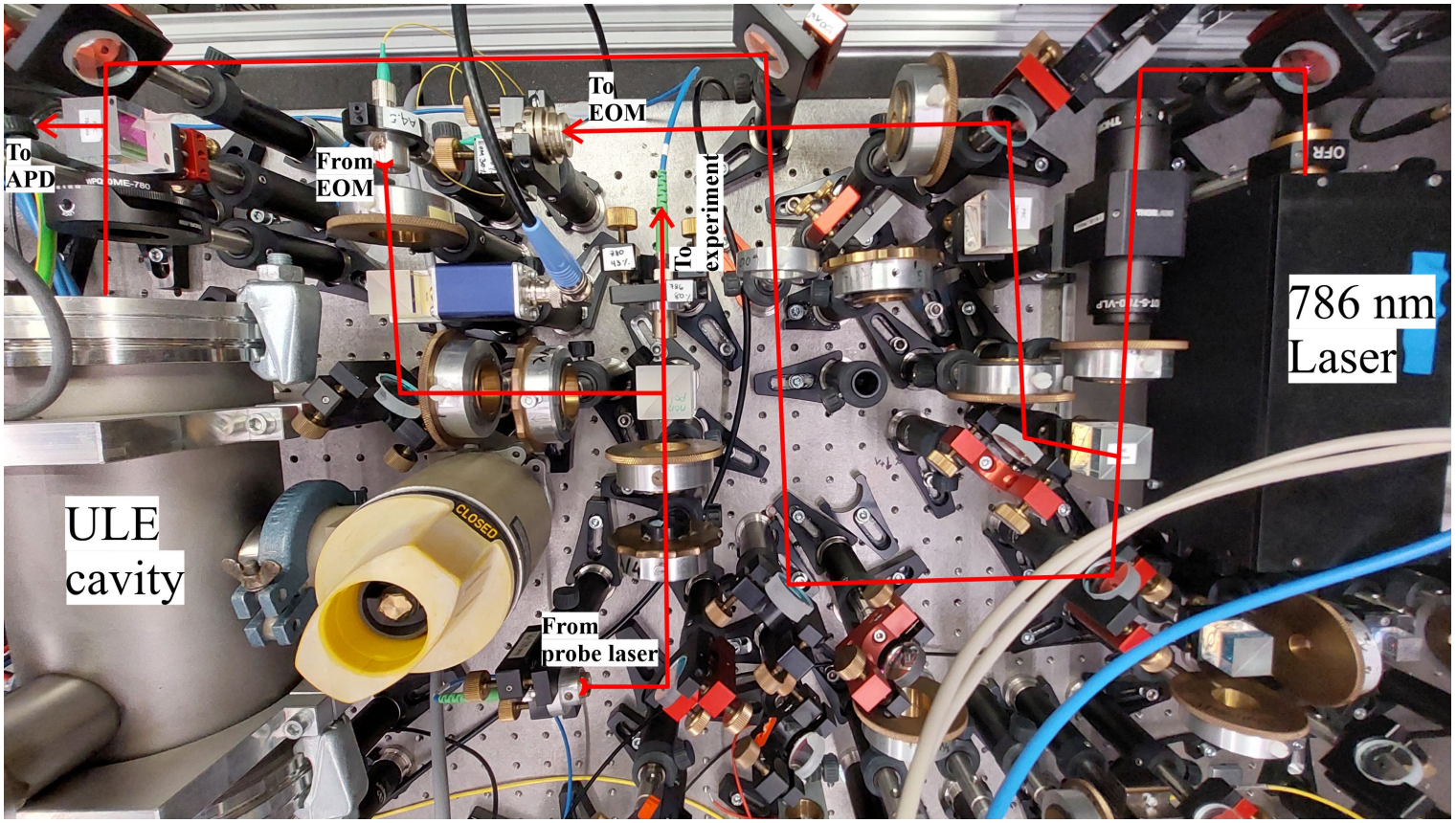

Figure 4.12.: A laser of 786 nm wavelength is coupled to a ULE cavity in order to stabilize the laser frequency. Furthermore, two wavelengths are coupled into the same single-mode polarization maintaining fiber with orthogonal polarizations: 786 nm ("lock" light) and 780 nm ("probe" light). In particular, lock light is AM by an EOM before being coupled to this fiber. The AM sidebands are used for controlling the science cavity frequency.

fit to Eq. (2.79) can be done on the measured transmission peak in order to obtain a value of $\delta_c = \omega_{cav} - \omega_{ge}$. A sample of values is collected after which a mean value is calculated and compared to the desired one in order to change the EOM driving frequency accordingly. In this way, Δ_c is adjusted with an uncertainty of 0.4 MHz given by the standard deviation. Finally a $FWHM = 13.4$ MHz is measured from the fit corresponding to a lifetime $\tau = 12$ ns and a finesse $\mathcal{F} = 213$.

An extra factor which affects the long-term stability of δ_c is temperature. Although details about the ULE cavity are not well known, its temperature is controlled to be at 30 °C. The science cavity, however, does not have any control over this parameter. As a result, due to temperature drifts around the chamber, it was observed that the value of δ_c drifted around 5 MHz on the order of hours. This was done by periodically measuring δ_c. The major problem with this was the corresponding voltage drift of the cavity piezoelement as will be explained later.

The signals of interest that are to be measured correspond to the transmitted light through the cavity. These are then compared with Eq. (2.79). For this, the measured signal is normalized with respect to the fitted peak voltage obtained by measuring the empty cavity resonance peak. This is a valid procedure for a non impedance matched cavity as well as one with non-ideal mirrors because, in any case, Eq. (2.79) is multiplied by a constant value. Nevertheless, the ratio of both lock and probe light are similarly transmitted through the cavity; however, only probe light is of interest. Thus, in order to discriminate it, an interference filter (IF) and a single mode fiber are used. While the former discriminates wavelength, the latter selects the fundamental transversal mode only. As a result, enough lock light to produce an error signal can be used while detecting just a small portion of it. In particular, this is detected with the most sensitive detector used (APD440A from Thorlabs).

As already mentioned, a probe field is used to drive the cavity. At the same time, a "pump" field travelling transversal to the cavity is needed for the Rydberg excitation. In the present work, probe and pump come from the same laser, stabilized by a beat with the reference laser. Each field is frequency shifted and switched using its own AOM. Consequently, the relative detuning between both fields ($\delta_1 - \delta_p$) is limited by the bandwidth of the AOMs. Finally, the transversal profile of the pump beam is shaped with a cylindrical lens in order to almost match the cavity mode profile. Similarly, the coupling beam is also shaped with another set of cylindrical lenses and

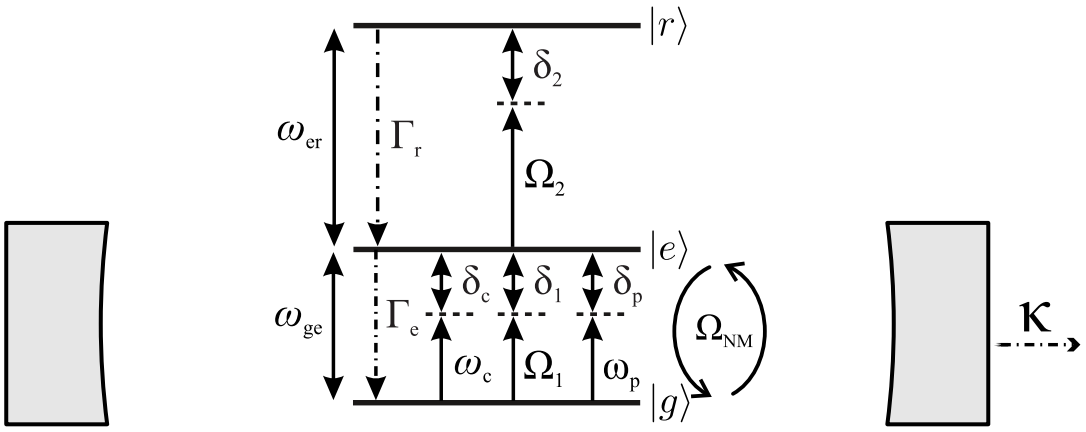

Figure 4.13.: Energy level scheme for three-level atoms inside a cavity. The cavity exchanges photons with the lower transition of an atom at a rate $\Omega_{NM} = 2g_0\sqrt{N_{\text{eff}}}$. On the other hand, the upper transition is strongly driven with Rabi frequency Ω_2 making the absorption paths of the cavity photon to interfere destructively; thus, making the cavity transparent to the probe field.

travels in the opposite direction of the pump beam. At the end, both beam waists at the MOT position are of similar size parallel to the cavity axis $w_r \sim 700\ \mu m$ and $w_z \sim 125\ \mu m$.

4.4. Normal mode splitting and EIT

The central point of the experimental setup is an atomic cloud positioned inside a cavity mode like the level scheme shown in Fig. 4.13. For this, the center of the MOT is shifted by the homogeneous field produced by the MOT coils and the compensation coils outside the vacuum chamber. First, a coarse adjustment is realized by loading an atomic cloud of large size while the cavity is resonant with the atomic transition and contains a large number of photons. As a result, with the aid of a CCD camera monitoring the MOT fluorescence, that part of the cloud which is inside the cavity mode is blown away due to radiation pressure. Then, the MOT position is optimized by switching on the probe laser right after the cloud preparation is finished and taking absorption images after a few microseconds time of flight. Finally, a finer adjustment is reached by reducing the MOT size close to the one that is finally used.

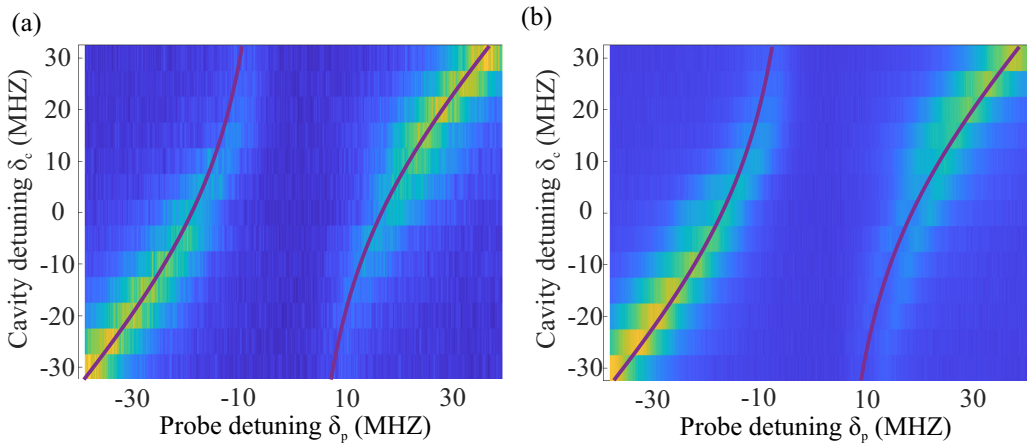

Figure 4.14.: Measured transmission spectra when atoms are located inside the cavity mode for different cavity detunings δ_c and intracavity photon numbers: ~ 2 in (a) and ~ 200 in (b). In both cases the transmission T is normalized to the respective peak empty cavity transmission: blue represents $T = 0$ while yellow $T = 1$. The purple curve corresponds to Eq. 2.84 with $\Omega_{NM} = 18$ MHz taken from a fit to (a) when $\delta_c = 0$.

At this point the cavity transmission spectrum shows the expected normal mode splitting. The overlap between MOT and cavity mode is then given a final adjustment by maximizing the frequency separation between the peaks for a resonant cavity. In general, the position and height of the normal mode peaks depend on the cavity detuning δ_c. The expected behavior is that of an avoided crossing, as observed in Fig. 4.14. There, measurements were taken for two different intracavity photon numbers in order to show that non linearities due to atomic saturation are not present in any case.

The number of atoms interacting with the cavity can be estimated by making a fit of the measured spectra to Eq. 2.79. A value of $g_0 = 2\pi \times 207$ kHz is calculated from a cavity mode volume of $V = 2.7 \times 10^{-10}\ m^3$ corresponding to the fundamental mode. Furthermore, an average Clebsch-Gordan coefficient (0.48 for $\pi-$transitions) over the equally populated ground states is accounted in this calculation. After this, the effective number of atoms interacting with the cavity is determined. For example, for the cloud shown in Fig. 4.2 a value of $N_{eff} = 10^4$ is obtained. In comparison, given the mode waist together with the cloud radius and total atom number extracted from this figure, $N_{eff} = 1.28 \times 10^4$ should be expected.

The transverse beams are aligned along the same axis crossing the atomic cloud

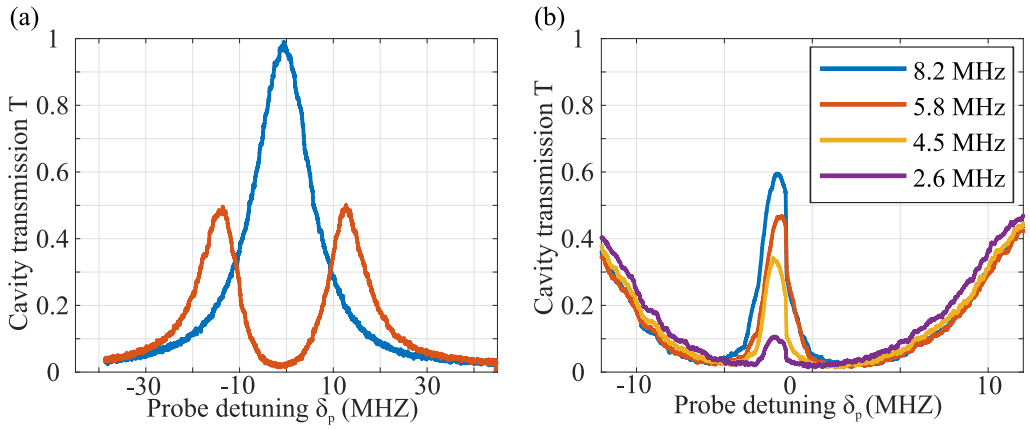

Figure 4.15.: The transparency window width and height dependence of cavity EIT on Ω_2. (a) Empty cavity spectrum (blue) and with atoms inside (orange). In this context, the transparency window dependence is shown in (b). The various colors represent different values of coupling Rabi frequency Ω_2. The traces here are averages of five measurements.

and the cavity axis. This is done by first optimizing the coupling beam path so that it allows the observation of cavity EIT. Due to the large difference between the beam waist in the cavity (on the order of 100 μm) and the large distance ($\sim$ 10 cm) to the last mirror a fine threaded screw is used for adjustment. Finally, the pump beam is made to overlap the coupling beam by maximizing the transparency window observed in free space EIT.

The cavity EIT spectrum is used for alignment of the coupling beam because the transparency window width and height depend on Ω_2. Then, as the beam has a Gaussian profile, the maximum intensity (thus, Ω_2) is located at its center. After this beam is properly adjusted, its optical power was changed in order to observe how the transparency window changes. These measurements are shown in Fig. 4.15. There, even though at higher values of Ω_2 the EIT peak is taller, its width increases. Nevertheless, the peak position on the frequency axis Δ_p and the actual height of the peak changes in each experimental cycle. For that reason, up to ten measurements were taken and each was fitted to Eq. 2.79. From this set of data, the mean and standard deviation were the values actually considered.

In Fig. 4.16 (a) two cavity EIT spectra are shown for equal Rabi frequency Ω_2 coupling the $5P_{3/2}$ state to the $30D_{5/2}$ Rydberg state. The difference between these plots is due to different values of the Rydberg state dephasing rate γ_r discussed

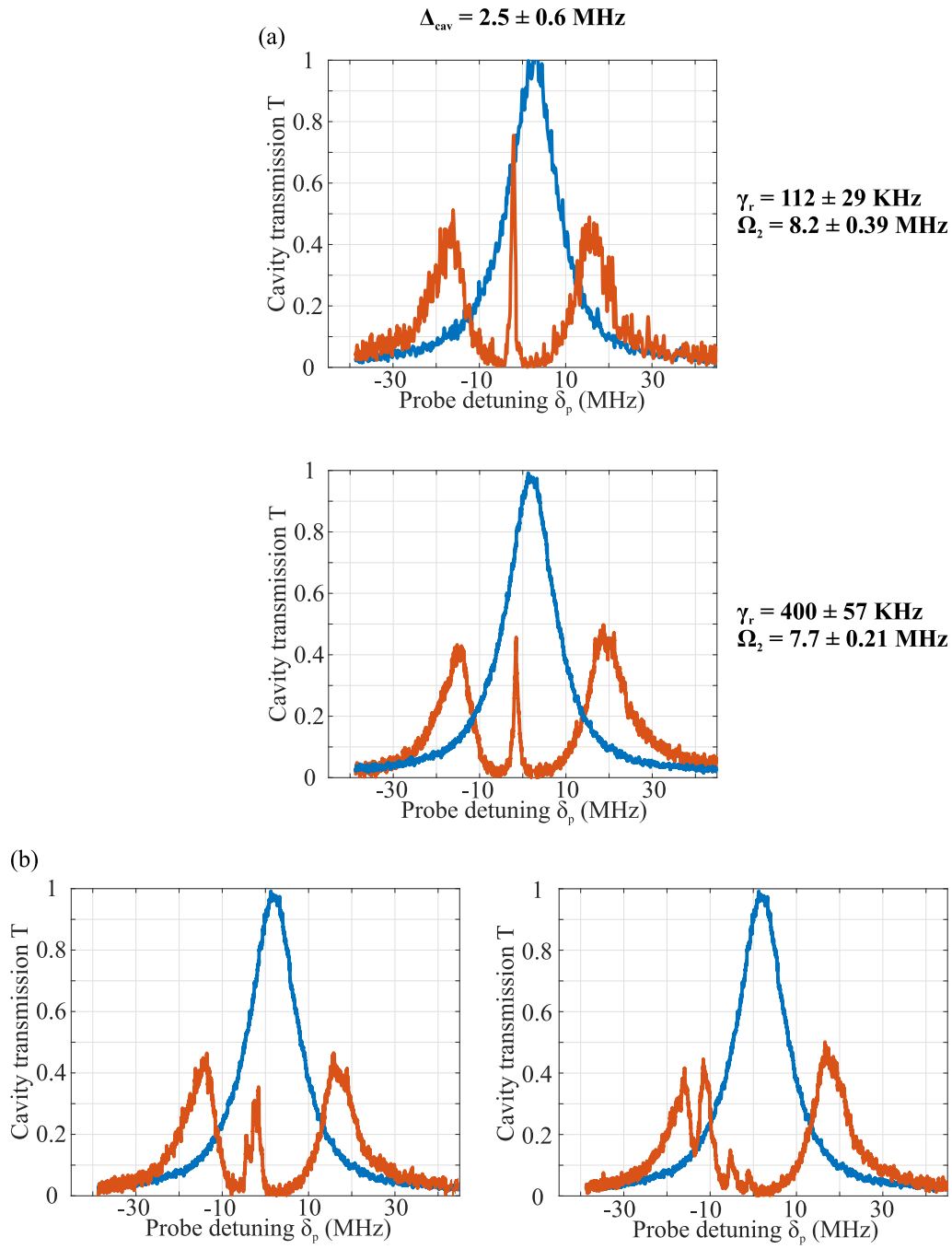

Figure 4.16.: (a) Cavity Rydberg EIT spectra with two different values of the dephasing rate γ_r as obtained from the fit. (b) When the cavity piezo voltage drifts too much what used to be a single transparency window turns into three. This is due to the Stark effect and is shown for two different electric field strengths. All traces here were taken in the same experimental conditions, the values shown are the fit results.

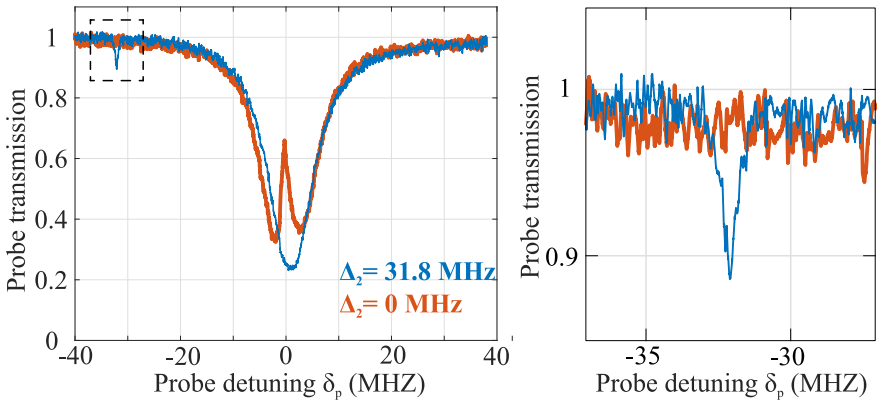

Figure 4.17.: Free space EIT under the experimental conditions of Sec. 4.5 for $\Delta_2 = 0$ and 31.8 MHz. Here though, the large detuning is done by using one of the sidebands resulting from the EIT spectroscopy on a cell. Therefore, keeping Ω_2 constant in contrast of Fig. 4.19 where the detuning was done by changing the AOM frequency.

in Ch. 2. These values are obtained by making a least-square fit to Eq. (2.79) with the atomic susceptibility given in Eq. (2.48). It was observed that γ_r was correlated with the piezo voltage. In fact, at some point the observed transparency window is splitted in three (see Fig. 4.16 (b)). These correspond to the three $|m_j| = 1/2,\ 3/2,\ 5/2$ states interacting with an electric field: the Stark effect. Here, the piezo is identified as the source for this field. A closer look to it revealed that the piezo was directly glued to the mirror mount. Consequently, it may be expected that there is a (bad) connection between the inner side (positive connector) of the piezo and the mirror mount which produces stray electric fields around the atoms. However, this is uncertain since the observed behavior was that the higher voltage across the piezo, the less dephasing. Then, as long as the piezo voltage is constant this stray electric field is "under control" since the dephasing rate γ_r would be constant. However, the cavity temperature drifts change the piezo voltage within hours limiting the time window to do an experiment under the same conditions. Trying to use the lower MOT coil as a heater on the last seconds of the experimental cycle was not successful.

Finally, the pump beam path is adjusted by observing EIT in free space: the lower transition is driven by the pump and not the intracavity field. This was the chosen procedure because the transparency window width and height depend on the overlap

between Ω_1 and Ω_2. The observations are shown in Fig. 4.18 for different values of Ω_2 and in Fig. 4.19 for varying Δ_2. There, one can observe both Autler-Townes splitting and EIT as discussed in Sec. 2.2.3. In particular, it is remarked that with a detuning $\Delta_2 = 31.8$ MHz (used for the results shown in Sec. 4.5) two-photon Rydberg excitation is shown to be possible (see Fig. 4.17 (b) and 2.6).

4.5. Optical cavity as detector of Rydberg dynamics

The cavity transmission has been previously used as detector of atom dynamics. In Ref. [84] it was used to observe the expansion of an atomic ensemble trapped in the optical lattice of a standing wave cavity. Also, in Ref. [85] precise measurements of the atom number fluctuations during evaporative cooling were performed using the same method. Finally, in Ref. [86] a dynamical phase transition was monitored by using light transmitted through the cavity.

In this work real-time detection of Rydberg dynamics is performed by exploiting the atom number dependence of the collective atom-cavity coupling Ω_{NM}. Indeed, N_{eff} accounts for those atoms that interact or exchange photons within the cavity mode unlike those which are excited to a Rydberg state. These are effectively off-resonant with respect to the cavity photons and, therefore, must be substracted from N_{eff}. Monitoring of Rydberg dynamics has been reported in [87, 88] without the use of a cavity.

In order to have a theoretical model to support the measurements the three-level optical Bloch equations are joined with the atom-cavity system. For this, the adiabatic approximation is recalled: whenever a bipartite system is governed by two different timescales, the full system dynamics can be described by the faster system eigenstates following the slower one. This is a procedure typically used in a cavity QED context in the so-called bad cavity regime where the cavity field is adiabatically eliminated. Here, this field is considered to reach its steady-state in a timescale κ^{-1}, much faster than the processes responsible of changing Ω_{NM}; in the present case: Rydberg dynamics, which is on the order of μs.

By following the discussion above, the cavity steady-state depends on the Rydberg dynamics via N_{eff}. Then, time-dependent $N_{\text{eff}}(t)$ is defined as

$$N_{\text{eff}}(t) = N_{\text{eff}}(P_g(t) + P_e(t)) \tag{4.3}$$

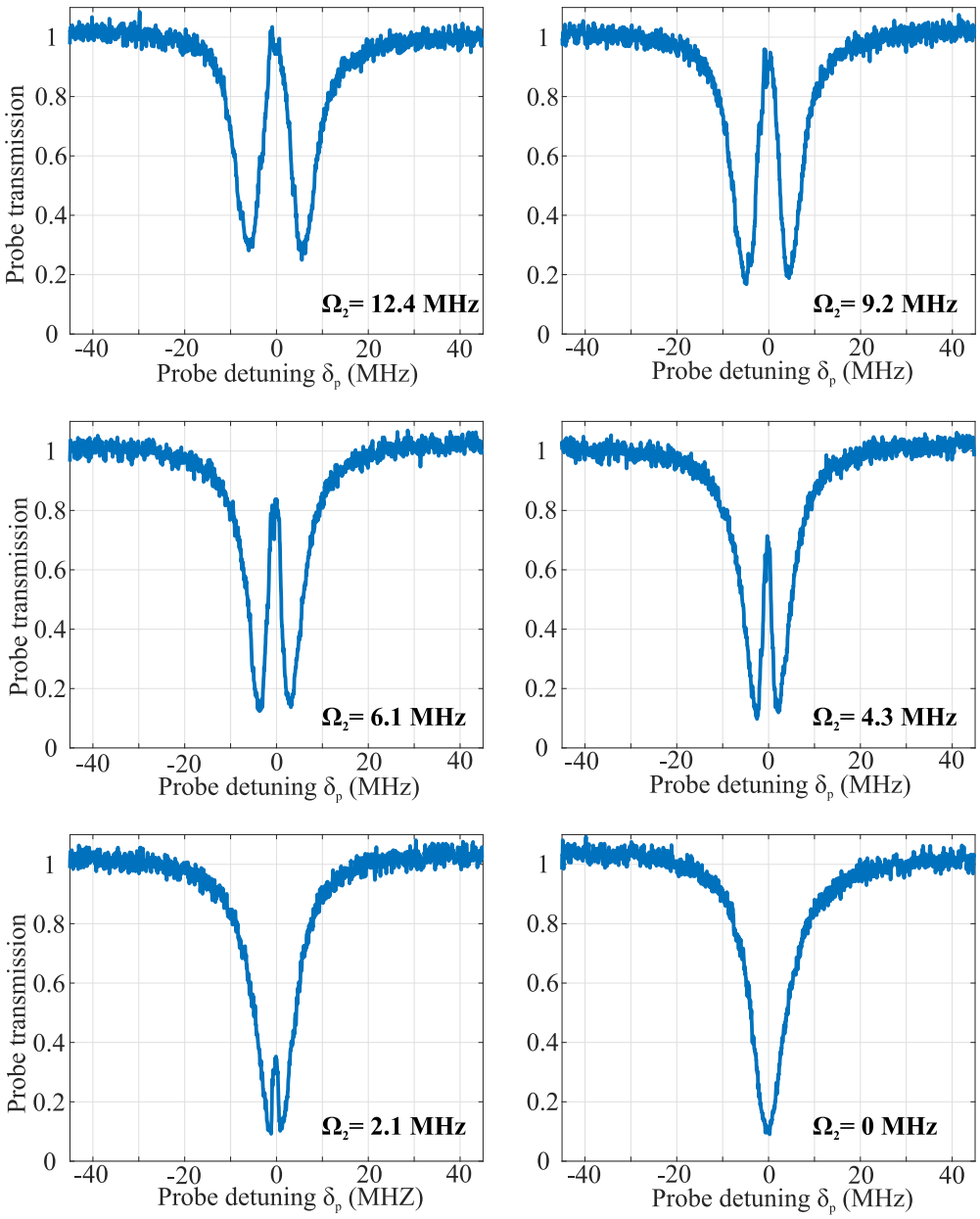

Figure 4.18.: Free space Rydberg EIT spectra. The coupling beam is focused ($w_0 = 200\ \mu m$) on the atomic cloud after which the transparency window is observed on the weak probe light. With $\Delta_2 = 0$, Ω_2 is varied from values greater than Γ_e so that Autler-Townes splitting is observed (top left) and, as it is decreased to values smaller than Γ_e EIT is finally observed (bottom left). Here, the probe detuning is scanned from +45 to -45 MHz in 1.5 ms.

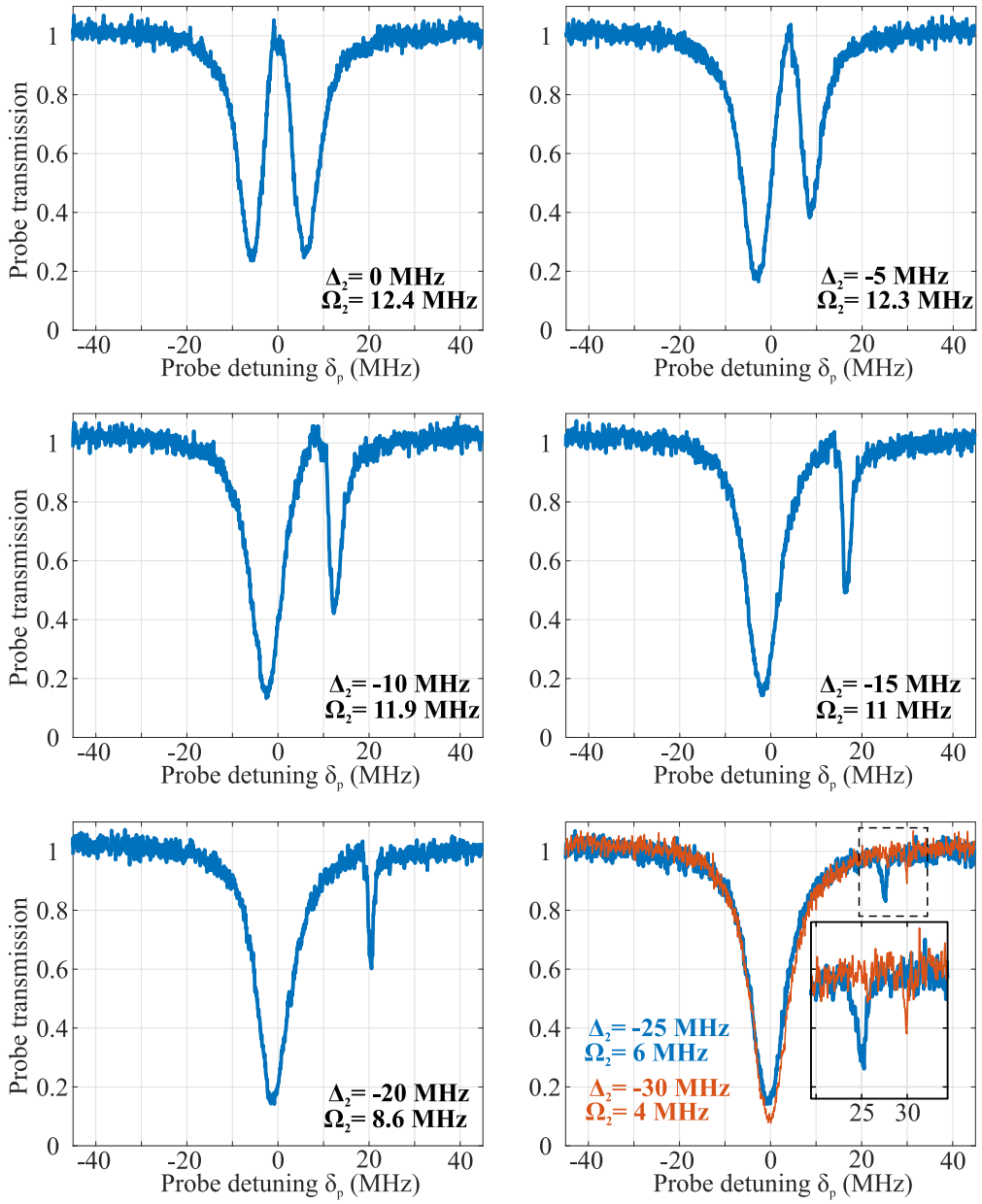

Figure 4.19.: Under the same conditions of Fig. 4.18 Δ_2 is varied. The coupling detuning is controlled by the RF driving the AOM which, however, does not keep the same optical power for each detuning; thus, Ω_2 also varies. Though the coupling beam angle after the AOM is also affected, care was taken to tilt the last mirror before the chamber horizontally every time. Nevertheless, at two photon resonance, transparency is observed and, at large detunings a second absorption deep corresponding to Rydberg excitation appears.

together with $P_g(t) + P_e(t) + P_{Ry} = 1$. Here, $P_{g,e,Ry}(t)$ is the probability for an atom to be in the ground, excited state or any other state, respectively. In particular, these can be the numerical solution of the three-level optical Bloch equations.

For this adiabatic approximation to be valid, the excited state must not influence the system dynamics. Thus, the low excitation regime or the effective two-level model as discussed in Sec. 2.2 must be fulfilled. Otherwise, the excited state population will make the system to decay or reach a steady-state faster since $\Gamma_e > \Gamma_r$. Therefore, for this experiment, the detuning δ_1 must be made large enough. On one hand, the RF frequency driving the AOM of the blue laser can be changed up to 30 MHz but at the cost of reducing the Rabi frequency to 30 %. On the other hand, one could use one of the sidebands generated by the EOM on the probe beam used on the Rb cell. Since the EOM is driven at 19.61 MHz this would translate to a coupling detuning $\delta_2 = 1.62 \times 19.6 = 31.8$ MHz (see Sec. 4.2.2) in vacuum with the advantage that the Rabi frequency is unchanged. This is the largest value that can be attained but, as shown before, it is enough to generate Rydberg excitation at two-photon resonance.

Since δ_2 is in this way fixed, δ_1 can be chosen appropriately to fulfill the two-photon resonance condition. This, in turn, limits the probe detuning δ_p driving the cavity because of the used setup. Indeed, as explained before, the difference between δ_1 and δ_p is varied by the driving frequency of two AOM: one fixed at 80 MHz and the other one variable. A difference $\delta_1 - \delta_p = 7.8$ MHz was chosen which then limits the tuning of $g_0\sqrt{N_{eff}}$ to ~ 20 MHz. This is in order to probe the cavity on the slope of one of the normal mode peaks which allows to observe changes of N_{eff}.

Another factor to consider for the Rydberg dynamics timescale is the dephasing rate. This is because, in the present case, population transfer into a Rydberg state relies on a coherent effect: Rabi oscillations. Indeed, within a Rabi period the atomic state is a superposition of $|g\rangle$ and $|r\rangle$. Thus, a faster decay rate of the coherences (antidiagonal terms of $\hat{\rho}$) will result in a less efficient Rydberg excitation. Furthermore, it is possible to derive a condition that the different parameters must fulfill to observe Rabi oscillations:

$$\frac{\Omega_2^2}{\Gamma_e} > \frac{\Omega_1\Omega_2}{2\Delta_1} > \gamma_d. \tag{4.4}$$

Here is shown that γ_d sets the lower limit for the effective two-level Rabi frequency

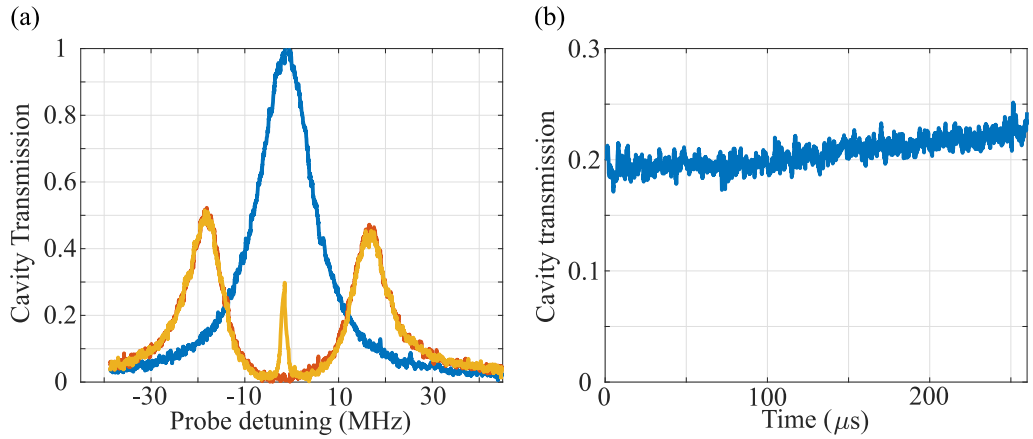

Figure 4.20.: (a) Measured cavity transmission spectra: empty cavity (blue), atom-cavity (orange) and cavity EIT (yellow). (b) The cavity transmission increases when the transversal beams are off due to optical pumping. This effect is treated as a systematic error by using this trace as reference.

Ω_{eff} and Ω_2^2/Γ_e which can be interpreted as the pump rate from $|e\rangle$ to $|r\rangle$. In the present case, $\Omega_{\text{eff}}^{\text{max}} = 0.466$ MHz and $\Omega_2^2/\Gamma_e = 9.6$ MHz meaning that Rabi oscillations wont be observed as $\gamma_d = 0.65$ MHz. Similarly, from the two-level effective model perspective, the ratio of excited atoms depend on the difference between Stark shifts from Ω_1 and Ω_2. In the present work, being Ω_2 fixed, the excitation efficiency is only controlled by the optical power of the pump beam (i.e. Ω_1).

4.6. Decoherence of Rydberg superradiance

The cavity transmission spectra corresponding to the experiment performed were taken with an avalanche photodiode of 10 MHz bandwidth and are shown in Fig. 4.20 (a). These traces are then fitted to Eq. 2.79 and the extracted parameter values are shown in Table 4.1. In particular, it is remarked that there is a slight cavity detuning $\Delta_c = -1.3$ MHz.

As explained before, the cavity is driven with a constant detuning $\Delta_p = 24$ MHz. Without turning on the transversal beams yet, the cavity transmission follows the optical pumping between the Zeeman states (see App. A). In Fig. 4.20 (b) an average from ten of these time signals is shown. This effect is treated as a systematic

	Empty cavity	Atom-cavity	Cavity EIT
Cavity detuning Δ_c	-1.3 ± 0.5 MHz	-	-
Cavity FWHM κ	13.6 ± 0.6 MHz	-	-
Atom number N_{eff} ($\times 10^3$)	-	6.5 ± 0.2	-
Dephasing rate γ_r	-	-	650 ± 69 kHz
Coupling Rabi frequency Ω_2	-	-	7.6 ± 0.3 MHz

Table 4.1.: Table with the experimental parameters obtained by doing a least-square fit to the spectra shown in Fig. 4.20.

error meaning that this averaged trace can be simply substracted from any subsequent measurement. For instance, this procedure is followed for Fig. 4.21 where $\Omega_1 = 2\pi \times 3.9$ MHz and $\Omega_2 = 0$. The result is a flat line which means that, at a detuning of $\Delta_1 = 31.8$ MHz, only optical pumping is present; thus, there is no radiation force coming from the pump beam.

Then, following this procedure, the coupling and pump beams are simultaneously turned on and Ω_1 is varied. The obtained time signals are shown in Fig. 4.21. The drop is more pronounced in transmission when two-photon excitation starts and gets deeper as Ω_1 increases. Furthermore, this fast drop happens on a timescale that corresponds to the inverse of the broadened linewidth γ_r^{-1}. This behavior corresponds to the coherent Rydberg excitation which would, in turn, be followed by a steady-state. However, the cavity transmission keeps slowly decreasing.

As explained in Ch. 2, a Rydberg state is in reality coupled to many other states around it. More importantly, BBR-induced transitions transfer atoms to neighboring Rydberg states which will, in turn, spontaneously decay back to the ground state through different states. This process is called shelving due to the longer timescale of spontaneous decay compared to stimulated emission. This is numerically simulated by using the parameters from Table 4.1 and the decay rate matrix shown in App. C as discussed in Sec. 3.1.1. The solution is shown as dashed lines in Fig. 4.21. Even though they qualitatively agree with the experimental data they do not fully explain the observed slow decrease quantitatively specially in those traces with greater Ω_1.

At this point we switch the attention to the excitation pulse endtime where also a quick jump occurs. This is, however, not related with Rydberg excitation but on the coupling field influence on the atom-cavity steady-state. Indeed, even though there

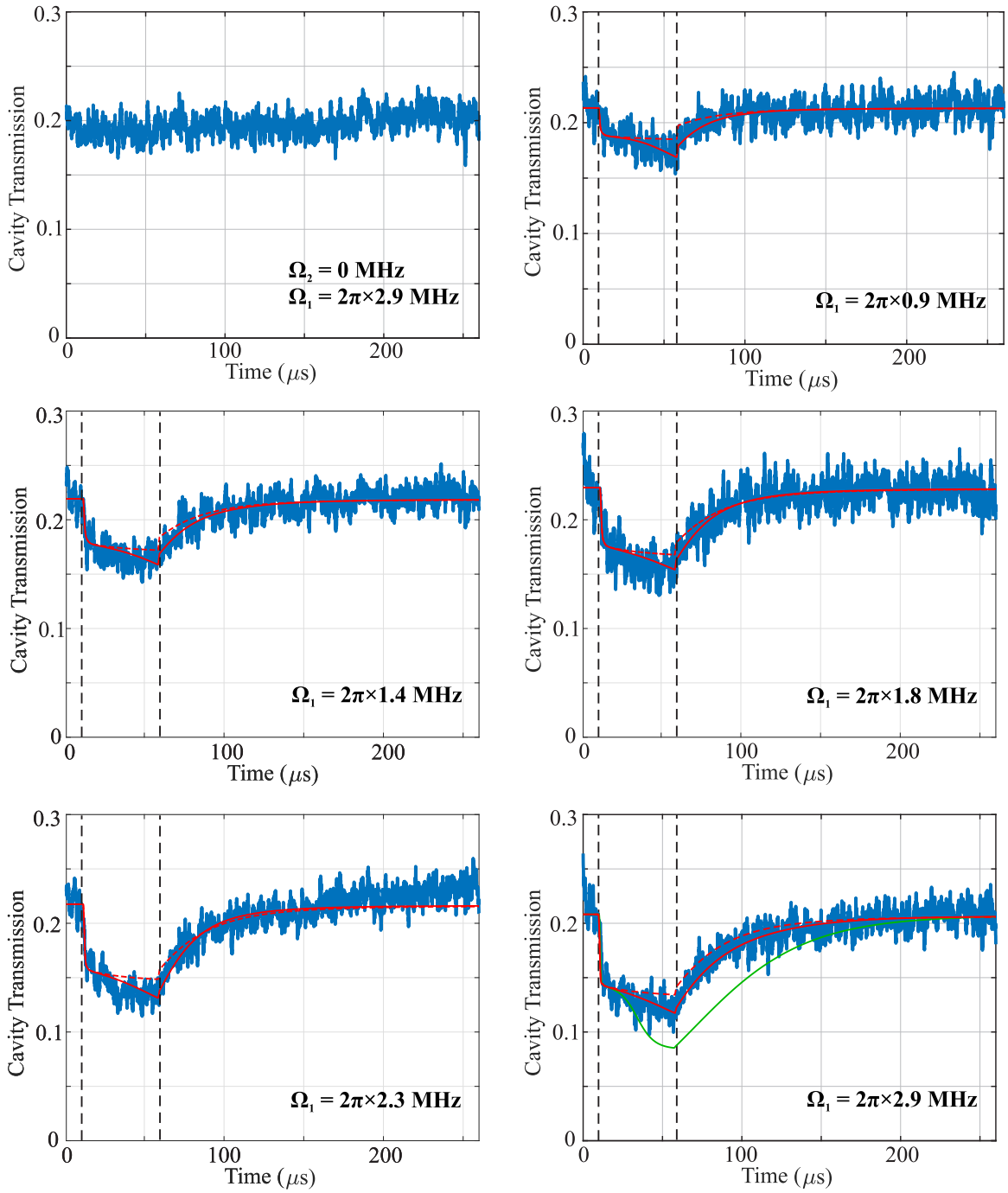

Figure 4.21.: Cavity transmission for fixed $\Delta_p = 24$ MHz. Transversal beams are pulsed simultaneously from $t = 10$ μs until $t = 60$ μs as highlighted with dashed vertical lines with exception of the top left figure which shows that Ω_1 does heat the atom cloud. The first 10 μs are used to determine Δ_c at each trace. The red lines show the result of numerical simulations excluding (dashed) and including (solid) superradiance together with the reduction factors $\beta_{1,2}$. The green solid line in the bottom right trace is the same numerical simulation but replacing the $\beta_{1,2}$ by the ones corresponding to the top right trace.

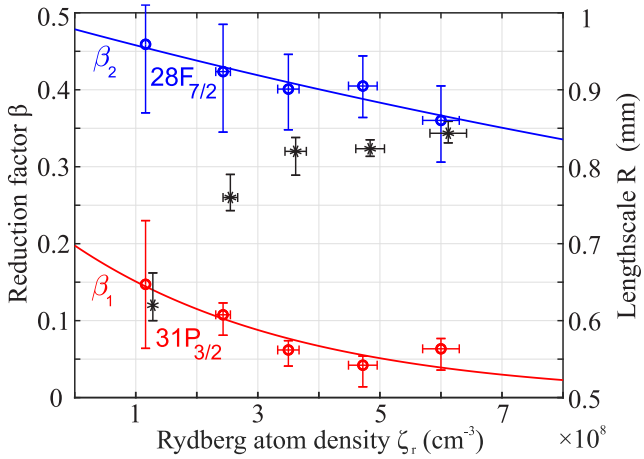

Figure 4.22.: Obtained parameters after fitting the time signals shown in Fig. 4.21. Circles (left axis) denote the reduction factors β_1 and β_2 for the two superradiant decays down to the $31P_{3/2}$ and $28F_{7/2}$ states, respectively. Stars (right axis) denote the length scale R of the superradiant cloud. Vertical error bars represent a 95% confidence interval and horizontal error bars represent a 5% uncertainty in the atom number. Solid lines are exponential fits (Eq. 4.5) to the reduction factors dependence on Rydberg atom density ζ_r. Data for R are shifted to the right by one data width for clarity.

is a two-photon detuning of 7.8 MHz between coupling field and cavity, it is not large enough. As a result, the cavity steady-state is different whether the coupling field is on or not. This is taken into account in all numerical simulations.

Shifting the attention back to the main part of the signal, a faster shelving rate than simulated is taking place in our system. Due to the atomic cloud size of $R \sim 0.5$ mm, superradiance can take place in our system and be responsible for the faster shelving rate. Indeed, the closer Rydberg states are the $31P_{3/2}$ and $28F_{7/2}$ (see Fig. 4.23) with transition wavelengths of 3.6 and 1.5 mm, respectively. Then, as the atomic sample and wavelengths have similar orders of magnitude, the cooperativity parameter introduced in Ch. 2 can reach large values. In parallel, the interparticle distance can be calculated from the peak density of the atomic cloud $\zeta = 2 \times 10^9$ cm^{-3}. Considering that in our case the percentage of atoms excited to the Rydberg state is at most 50%, it is most likely for any atom to have a neighbor at a distance of $(2\pi\zeta)^{-1/3} = 5.4$ μm.

From the discussion of Ch. 3, one can conclude that at these close distances

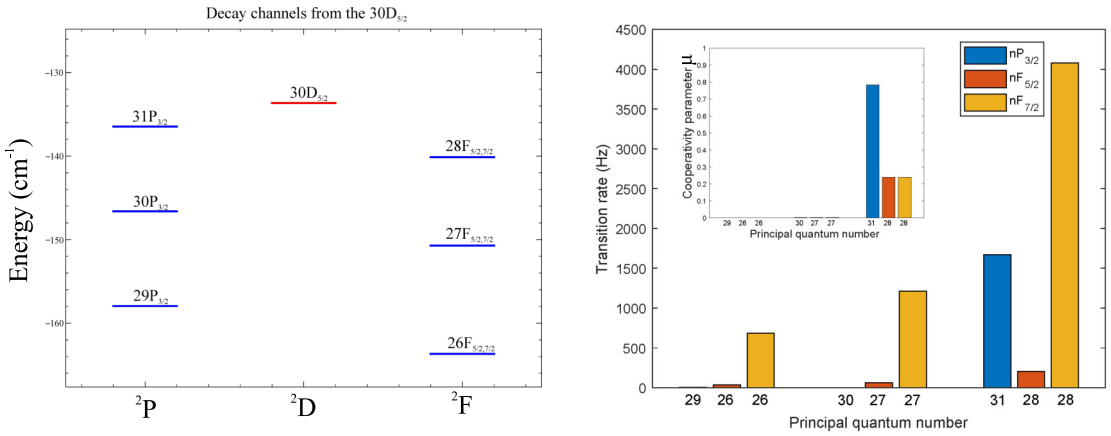

Figure 4.23.: Left: Nearby Rydberg states to the $30D_{5/2}$ state. Right: Transition rates in Hz from the $30D_{5/2}$ state to the states shown in the left figure. In the inset the cooperativity parameter μ introduced in Sec. 2.4.3 is shown for the same transitions.

dipole-dipole interactions should have an effect on superradiance, especially after considering the C_3 coefficients for the involved states shown in Table 4.2. The proposed model in the same chapter is then applied to the current experimental conditions with three free parameters: $\beta_{1,2}$ and R corresponding to decoherence and cloud lengthscale, respectively. In fact, though by using only the first ten microseconds, the cavity detuning Δ_c is also fitted to the data. This is because the shot to shot fluctuations of Δ_c change the initial positions of the different time traces.

The results are plotted in Fig. 4.22 with the error bars representing 1σ uncertainty. It is remarked that the horizontal axis correspond to $\zeta_r = P_r\zeta$ where P_r is the steady-state ratio of atoms in the Rydberg state in the simplified three-level system. Then, following the decoherence model discussed in Sec. 3.2.1, an exponentially decaying function of the form

$$\beta_{1,2} = A_{1,2}e^{-\frac{4\pi}{3}\zeta_r r^3_{\mathrm{cr}\ 1,2}} \tag{4.5}$$

is fitted to the data points of $\beta_{1,2}$. The obtained values of $r_{\mathrm{cr}\ 1,2}$ are compared to the theoretical ones in Table 4.2. A very good agreement is observed, confirming that dipole-dipole interactions do in fact decohere superradiance. Furthermore, in order to remark the need of different reduction factors for various Rydberg densities, in Fig. 4.21 the green line shows how using the largest values of $\beta_{1,2}$ (corresponding

to lowest ζ_r) on the trace of largest ζ_r results in an obvious discrepancy. Finally, since the parameters $A_{1,2}$ are density independent they are not caused by atom pair interactions. These parameters may be accounting for the unprecise knowledge of the atom number inside the cavity or they can be interpreted as the effects on superradiance due to homogeneous broadening on the Rydberg linewidth [89, 90, 91].

The calculated critical radii $r_{\mathrm{cr}\ 1,2}$ shown in Table 4.2 result from taking an average $\langle C_{3,k}\rangle$ where the index k denotes the decay into state $31P_{3/2}$ and $28F_{7/2}$. Indeed, in addition to its spatial dependence (see Eq. (2.95)), each pair of states from a dipole allowed transition has a different value of C_3 due to the varying Clebsch-Gordan coefficients. Then, a weighted average is defined as

$$\langle C_{3,k}\rangle = \frac{1}{n_j}\sum_{j'\neq j} C_{3,k}^{j,j'} G_{j,j'}^2 \tag{4.6}$$

where $G_{j,j'}^2$ is the squared Clebsch-Gordan coefficient for the decay path $|m_j\rangle \rightarrow |m_{j'}\rangle$ and the normalization constant is the number of m_j sublevels $n_j = \sum_{j,j'} G_{j,j'}^2$. The spatial dependence, on the other hand, is integrated as $\int |1-3\cos^2\theta| d\Omega$ where Ω is the solid angle on a unit sphere and an absolute value is taken in order not to balance positive frequency shifts with negative ones, as both signs lead to a detuning from the superradiant transition. As a result, the values obtained are $\langle C_{3,1}\rangle = 0.247$ GHz $(\mu\mathrm{m})^3$ for the decay down to the $31P_{3/2}$ state and $\langle C_{3,1}\rangle = 0.079$ GHz $(\mu\mathrm{m})^3$ for the decay down to the $28F_{7/2}$ state.

On the other hand, the observed reduction of R as ζ_r decreases is explained by the Gaussian spatial profile of $\Omega_{1,2} \propto e^{-r^2/w_0^2}$ and the nonlinear dependence of ζ_r on Ω_1. Indeed, for weak driving $\zeta_r \propto \Omega_1^2$; thus, the $1/e$ radius of the Rydberg cloud is $r_0 = w_0/\sqrt{2}$. As the peak Rabi frequency Ω_1 is increased (but below saturation), the scaling becomes linear such that both, cloud and beam radius are equal ($r_0 = w_0$). The factor of $\sqrt{2}$ difference in r_0 matches the observation in Fig. 4.22.

$30D_{5/2}$	Fit (μm)	Theory (μm)	C_3 (2π GHz $\mu\mathrm{m}^3$)	A
$\rightarrow 31P_{3/2}$	$8.4\ \pm\ ^{1.4}_{1.6}$	7.9	-0.247	$0.18\ \pm\ ^{0.09}_{0.07}$
$\rightarrow 28F_{7/2}$	$4.6\ \pm\ ^{1.0}_{1.9}$	5.4	-0.079	$0.48\ \pm\ ^{0.06}_{0.07}$

Table 4.2.: Obtained values for the critical radii compared to the calculated theoretical ones by using the C_3 coefficient.

5. Conclusions and outlook

In this work an ensemble of ^{87}Rb atoms is loaded into a MOT which overlaps with the mode of an optical cavity. The atoms are released and excited to the $30D_{5/2}$ Rydberg state. This collection of atoms exchanges energy (or photons) with the cavity mode at a rate given by the collective atom-cavity coupling $\Omega_{\mathrm{NM}} = 2g_0\sqrt{N}$ where N is the number of atoms interacting with the cavity. Then, by detecting variations of Ω_{NM} through the cavity transmission, atom dynamics within the cavity can be tracked [84]. In particular, for the present project the decay dynamics from the $30D_{5/2}$ state was monitored. The superradiant decay rate to neighboring Rydberg states is shown to depend on the Rydberg atom density: a signature of dipole-dipole interactions dephasing or decohering superradiance. To explain these observations a model is then introduced which effectively reduces the number of atoms participating in the superradiant decay [92]. These results contribute not only to better understand the interplay between superradiance and resonant dipole interactions but also the excitation to Rydberg states in a many-body context.

Rydberg excitation is performed via a two-photon transition using the $5P_{3/2}(F = 3)$ state as the intermediate state of a ladder-type system. The upper transition is driven by the coupling laser with a wavelength of 480 nm which is obtained by second harmonic generation or frequency doubling. For this, an optical resonator with an LBO crystal inside is designed and built as explained in Sec. 4.2.1. The coupling laser frequency is tuned to resonate with a particular Rydberg state by obtaining an error signal (FM technique) from the EIT spectrum measured in a Rb cell.

EIT is a coherent process where an atom becomes transparent to a two-level transition when a second laser strongly drives the upper state of this transition to a third state. In order to show that atoms inside the cavity are also coupled to a Rydberg state, cavity EIT was demonstrated. These traces were also used to benchmark some parameters like the broadened Rydberg linewidth γ_r and the

coupling Rabi frequency Ω_2. Later, EIT on free space was measured showing that control over Ω_2 allows to observe Autler-Townes splitting as well as EIT. Also, two-photon Rydberg excitation is observed by increasing the coupling laser detuning δ_2 up to ~ 32 MHz. Therefore, solid ground is given to the interpretation of the main results of this thesis.

Rydberg decay dynamics was observed by using the transmission of an optical cavity. For this, a low-finesse cavity was installed since, in the collective strong coupling regime ($\Omega_{\mathrm{NM}} \gg \Gamma_e/2$) and at resonance with the atomic transition ($\delta_c = 0$), the normal mode peaks are shown to transmit around half the light relative to the peak transmission when no atoms are present together with a linewidth of ~ 10 MHz. Then, probing the cavity on the slope of one of these modes delivers enough dynamic range for the expected change of N. Contrary to expectation, keeping δ_p and δ_c fixed without Rydberg excitation the cavity transmission is observed to be not constant. A set of equations is derived in App. A to explain this as the change of Ω_{NM} through the Clebsch-Gordan coefficients due to optical pumping by the intracavity light field. However, when Rydberg excitation is turned on the cavity transmission quickly drops agreeing with the argument that a number of atoms are excited out of the two-level system driven by the cavity. Later, when these beams are turned off, the cavity transmission slowly goes back to its original value on a timescale which does not correspond to the $30D_{5/2}$ state lifetime ($\tau \sim 20\mu$s). Thus, neighboring Rydberg states have also been populated (i.e. shelving). Simulations were performed accounting for the decay and BBR-induced transitions to several neighboring states (see App. C) without free parameters in the initial conditions.

A faster shelving rate is taking place that these simulations do not explain. Under the described experimental conditons this can only be explained by superradiant enhancement of the decay from the $30D_{5/2}$ state. Indeed, the decay down to the $28F_{7/2}$ and $31P_{3/2}$ state are shown to be the most important superradiant decay channels. Nevertheless, due to stray electric fields superradiance is expected to be damped. Interestingly, this dampening is observed to also depend on the Rydberg atom density. To explain this feature, a model is introduced that effectively reduces the number of atoms participating in the superradiant decay by defining a critical radius r_c that depends on the resonant dipole-dipole interaction C_3 coefficient: atom pairs closer than r_c are sufficiently dephased so that they become distinguishable from other pairs making up the many-body state responsible for superradiance. The

model is compared with the data and a very good agreement is observed.

The collective atom-cavity coupling is exploited in this project as a tool to study Rydberg decay dynamics. Most importantly, superradiant enhancement of the BBR induced transition rate to two neighboring Rydberg states is observed to be density dependent. The number of atoms inside the cavity mode is obtained by measuring the normal mode splitting and, from this, the ratio of atoms excited to the $30D_{5/2}$ state was implied from the measured Rabi frequencies of the beams transversal to the cavity. Instead, Rydberg population could be measured directly by collecting the fluorescence after estimulated emission from a fourth state (e.g. $6P_{3/2}$). To further improve control over our system broadening of the Rydberg state can be lowered by adding a set of electrodes to compensate any stray electric field; in addition, a ULE cavity has been recently built up in order to reduce the lasers' linewidth. Furthermore, a new science cavity has been designed which includes six electrodes and higher reflective mirrors. The latter will reduce the cavity FWHM and increase the cooperativity parameter C_1 which allows Rabi oscillations between the atomic ensemble and cavity photons to be observable. This new capability will open the possibility to explore collective behavior as in the Dicke phase transition [93] which could, in turn, be enriched by addition of dipole-dipole interactions between Rydberg atoms. This is the main subject of study of the new project currently being developed in the group.

A. Cavity QED with multilevel atoms

The state manifolds consisting of the different Zeeman states is usually not considered in cavity QED experiments. In fact, it is avoided by optically pumping the atoms into a Zeeman state with $m_F = \pm F$ and using circularly polarized light in order to isolate a single two-level transition. However, the Zeeman structure of atoms (i.e. multilevel atoms) has recently acquired particular attention in cavity QED systems [94]. For the present thesis a set of differential equations were derived in order to describe the interaction between a single cavity mode and an ensemble of multilevel atoms. Even though the work to be presented in this appendix was done independently of Ref. [94] they share a similar approach. Nevertheless, they follow different paths and arrive to different conclusions.

A.1. Interaction with a multilevel atom

We can think of a multilevel atom as consisting of many radiating dipoles interacting with the same field $\mathcal{E}$. The number of dipoles depends on the total angular momentum of the ground state (F_g) and excited state (F_e) as well as the polarization of the field. Here, the case to be considered is that of $F_g = 2$, $F_e = 3$ coherently coupled by π-transitions. Therefore, we have five dipoles one for each $m_F = -2 \rightarrow +2$ which will be labeled with an index k. Then, the interaction Hamiltonian, following Eq. 2.3, is written as

$$\hat{\mathcal{H}}_{int} = -\sum_{m=-2}^{2} \hat{\mathbf{d}}_m \cdot \mathcal{E} \tag{A.1}$$

where $\hat{\mathbf{d}} = \mathbf{d}_m \hat{\sigma}_m^- + \mathbf{d}_m^* \hat{\sigma}_m^+$ with $\hat{\sigma}_m^+ = |e, m\rangle\langle g, m|$ and $\hat{\sigma}_m^- = |g, m\rangle\langle e, m|$. The dipole matrix elements are proportional to a common value $\mathbf{d}_m = W_m \mathbf{d}_{ge}$ where W_m is the Clebsch-Gordan coefficient for the m-th transition and $\mathbf{d}_{ge} = \langle J_g \,||er||\, J_e \rangle$. Similarly, the uncoupled atom Hamiltonian can easily be extended to the multilevel case when

states of the same manifold are degenerate:

$$\hat{\mathcal{H}}_a = \frac{1}{2}\omega_0 \sum_{m=-2}^{2} \hat{\sigma}_m^z. \tag{A.2}$$

A.1.1. Lindblad operators

The jump or Lindblad operator describing spontaneous decay of a two-level atom was already introduced in Sec. 2.1.1 to be given by

$$\hat{\mathrm{L}} = \hat{\sigma}^- = |g\rangle\langle e|\,. \tag{A.3}$$

On the other hand, in the multilevel case, when a polarized photon is emitted by spontaneous decay it is impossible to determine which Zeemann state from the excited manifold has decayed. But it is possible to give a probability for this event to happen. Indeed, since the Zeemann states of the same manifold are orthogonal, the probability of emission of a photon with polarization μ is given by

$$p_\mu = \sum_k \beta_{jk} p_k^e \tag{A.4}$$

where p_k^e is the probability for the atom to be at the k-th Zeemann state of the excited manifold and β_{jk} is the corresponding branching ratio [95] of the same Zeeman state. This implies that the multilevel jump operator describing the emission of a μ-polarized photon by spontaneous decay can be written as

$$\hat{\mathrm{L}}_\mu = \sum_k \sqrt{\beta_{jk}}\hat{\sigma}_k^-. \tag{A.5}$$

Here, the index j corresponds to the Zeemann state of the ground manifold where the atom decays to. The dipole selection rules limit this index to $j = k-1, k, k+1$ (see Fig. A.1). Furthermore, the sum of these coefficients must sum one since

$$\Gamma_e = \sum_j \Gamma_j = \sum_j \beta_{jk}\Gamma_e \tag{A.6}$$

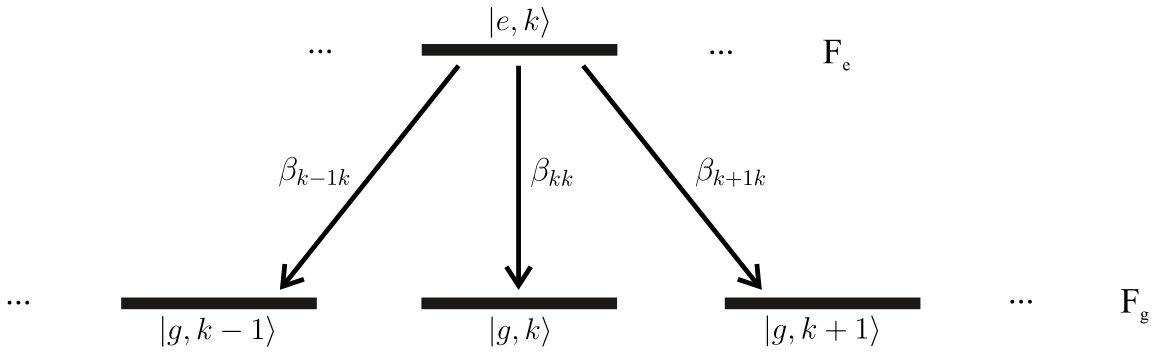

Figure A.1.: Building block of the level scheme for a multilevel atom where each dark line represent a Zeemann state belonging to a manifold of $2F+1$ Zeemann states. By spontaneous decay, an excited state emits a photon and transition to a certain Zeemann state from the ground state manifold. The probability or branching ratio for any of the three possible transitions is denoted as β_{jk}.

and, therefore

$$\sum_j \beta_{jk} = 1. \tag{A.7}$$

Consequently, one can build up a matrix $\tilde{\beta} = [\beta_{jk}]$ with the condition that the elements of each column must sum one.

For the hyperfine states considered in this thesis the excited manifold contains seven ($m_F = -3 \rightarrow +3$) Zeemann states while the ground manifold five ($m_F = -2 \rightarrow +2$). Finally, the three Lindblad operators for this particular case can then be written as

$$\hat{\mathrm{L}}_{\pi} = \sum_{k=-2}^{2} \sqrt{\beta_{kk}}\, |g,k\rangle \langle e,k| \tag{A.8}$$

$$\hat{\mathrm{L}}_{\sigma^-} = \sum_{k=-2}^{2} \sqrt{\beta_{kk+1}}\, |g,k\rangle \langle e,k+1| \tag{A.9}$$

$$\hat{\mathrm{L}}_{\sigma^+} = \sum_{k=-2}^{2} \sqrt{\beta_{kk-1}}\, |g,k\rangle \langle e,k-1| \,. \tag{A.10}$$

When an ensemble of atoms is considered an important assumption is made: atoms scatter independently of each other into the vacuum modes. This is particularly true in our experimental setup where a low-finesse cavity is used. Here is

where we depart from Ref. [94]. There it is assumed that the atoms scatter into the same (cavity) mode. Consequently, each Lindblad operator includes a sum over the atoms which results in superradiant decay modes.

A.1.2. Multilevel atom-cavity Bloch equations

Calculating the Bloch equations for an ensemble of N multilevel atoms interacting with a single cavity mode is done similarly as in Sec. 2.3. This time, however, Eq. A.1 must be considered. The equivalent Tavis-Cummings hamiltonian then reads

$$\hat{\mathcal{H}}_{int} = \sum_{j=1}^{N_{eff}} \sum_{m=-2}^{2} g_m (i\hat{a}^\dagger \hat{\sigma}_{jm}^- - i\hat{a}\hat{\sigma}_{jm}^+) \tag{A.11}$$

with $g_m = W_m g_0$. The homogeneity of g_0 allows to simplify this hamiltonian by introducing the variables $\hat{\sigma}_m^\pm = \sum_{j=1}^{N_{eff}} \hat{\sigma}_{jm}^\pm$ and $\hat{\sigma}_m^z = \sum_{j=1}^{N_{eff}} \hat{\sigma}_{jm}^z$. Then, accounting also for the dissipators introduced in the previous section, the mean-field equations are written as

$$\frac{d\langle\hat{a}\rangle}{dt} = -(\kappa/2 - i\Delta)\langle\hat{a}\rangle + \sum_{m=-2}^{2} g_m \langle\hat{\sigma}_m^-\rangle + \mathcal{E} \tag{A.12}$$

$$\frac{d\langle\hat{\sigma}_m^-\rangle}{dt} = -(\Gamma/2 - i\delta_p)\langle\hat{\sigma}_m^-\rangle + g_m \langle\hat{a}\rangle\langle\hat{\sigma}_m^z\rangle \tag{A.13}$$

$$\frac{dN_m}{dt} = \frac{\Gamma}{2}(\beta_{mm-1}(\langle\hat{\sigma}_{m-1}^z\rangle + N_{m-1}) + (\beta_m - 1)(\langle\hat{\sigma}_m^z\rangle + N_m) \tag{A.14}$$

$$+ \beta_{mm+1}(\langle\hat{\sigma}_{m+1}^z\rangle + N_{m+1})) \tag{A.15}$$

$$\frac{\mathrm{d}\langle\hat{\sigma}_m^z\rangle}{\mathrm{d}t} + \frac{dN_m}{dt} = -\Gamma(N_m + \langle\hat{\sigma}_m^z\rangle) - 2g_m(\langle\hat{a}^\dagger\rangle\langle\hat{\sigma}_m^-\rangle + \langle\hat{a}\rangle\langle\hat{\sigma}_m^+\rangle). \tag{A.16}$$

Here, $\Delta = \delta_p - \delta_{cav}$ where $\delta_{p,cav}$ is the detuning relative to atomic transition. In contrast to Sec. 2.3, an extra differential equation appears. This one describes optical pumping: the change on the number of atoms on the m-th driven transition $N_m = N_{eff}\mathcal{P}_m$. Where $\mathcal{P}_m = \mathcal{P}_m^e + \mathcal{P}_m^g$ is the probability for a single atom to belong on the mth transition whether on the state $|e, m\rangle$ or $|g, m\rangle$. Needless to say is that the total number of atoms is considered to be constant: $N = \sum_m N_m$.

A.2. Steady-state solution

It is of most interest to calculate the steady-state solution of the system. Then, all the derivatives are set to zero and we start by introducing the variable $\mathrm{X}_m = \langle \hat{a} \rangle / \sqrt{n_0^m}$ with the saturation photon number $n_0^m = \Gamma^2 b / 8 g_m^2$. From Eq. A.13 we have

$$\left\langle \hat{\sigma}_m^- \right\rangle = 2 \frac{g_m}{\Gamma} \sqrt{n_0^m} \frac{\langle \hat{\sigma}_m^z \rangle}{1 - i\delta_p'} \mathrm{X}_m. \tag{A.17}$$

Introducing this relation into Eq. A.16 results in

$$\Gamma(\langle \hat{\sigma}_m^z \rangle + N\mathcal{P}_m) = -8 \frac{g_m^2 n_0^m}{\Gamma} |\mathrm{X}_m|^2 \frac{\langle \hat{\sigma}_m^z \rangle}{1 + \delta_p'^2}. \tag{A.18}$$

Which can be further simplified to

$$\langle \hat{\sigma}_m^z \rangle = \frac{-N\mathcal{P}_m}{1 + \frac{b|\mathrm{X}_m|^2}{1+\delta_p'^2}}. \tag{A.19}$$

Then, combining eqs. A.17 and A.19 we get

$$\frac{g_m \left\langle \hat{\sigma}_m^- \right\rangle}{\kappa} = -N(1 - i\delta_p') \frac{\Gamma b}{4\kappa} \mathcal{P}_m'' \mathrm{X}'. \tag{A.20}$$

Here, $\mathrm{X}' = \langle \hat{a} \rangle$ and $\mathcal{P}_m'' = \mathcal{P}_m'/n_0^m$ with $\mathcal{P}_m' = \frac{\mathcal{P}_m}{1+\delta_p'^2+b|\mathrm{X}_m|^2}$. Also, the relation $n_0^m C_1^m = \frac{\Gamma b}{4\kappa}$ is used where $C_1^m = 2g_m^2/\kappa\Gamma$ is the single-atom cooperativity of the m-th transition.

Next, using Eq. A.15 together with Eq. A.19 we further obtain the relation

$$0 = \beta_{mm-1} \mathcal{P}_{m-1}'' + (\beta_m - 1)\mathcal{P}_m'' + \beta_{mm+1} \mathcal{P}_{m+1}'' \tag{A.21}$$

which can be rewriten in a matrix form:

$$0 = \mathrm{A} \cdot \vec{\mathcal{P}}'' = (\tilde{\beta} - \mathbb{1}) \cdot \vec{\mathcal{P}}''. \tag{A.22}$$

As mentioned before, the hyperfine states in consideration are $F_g = 2$ and $F_e = 3$ driven by π transitions. Therefore, we can define the vector $\vec{\mathcal{P}}'' = [\mathcal{P}_m]$ with $m =$

$-2, \ldots, +2$ and introduce the corresponding matrix

$$\mathrm{A} = \begin{pmatrix} 1/3-1 & 1/15 & 0 & 0 & \\ 2/3 & 8/15-1 & 1/5 & 0 & 0 \\ 0 & 2/5 & 3/5-1 & 2/5 & 0 \\ 0 & 0 & 1/5 & 8/15-1 & 2/3 \\ 0 & 0 & 0 & 1/15 & 1/3-1 \end{pmatrix}. \tag{A.23}$$

Eq. A.22 states that the vector $\vec{\mathcal{P}}''$ is an eigenvector of A with eigenvalue equal to 0 (i.e. is part of the null space). This can be solved to obtain

$$\vec{\mathcal{P}}'' = \mathrm{v}(1, 10, 20, 10, 1) \tag{A.24}$$

where v is a normalization constant which can be calculated by applying the condition

$$\sum_{m=-2}^{+2} \mathcal{P}_m = 1. \tag{A.25}$$

Indeed, by expanding Eq. A.25:

$$\sum_{m=-2}^{+2} (n_0^m(1+\delta_p^2) + b\,|\mathrm{X}'|^2)\mathcal{P}''_m = 1. \tag{A.26}$$

and then using Eq. A.24 the normalization constant can be finally obtained

$$\mathrm{v} = \frac{1}{(n'_0(1+\delta_p^2) + b'\,|\mathrm{X}'|^2)} \tag{A.27}$$

where $n'_0 = (n_0^{-2} + 10n_0^{-1} + 20n_0^0 + 10n_0^{+1} + n_0^{+2})$ and $b' = 42b$. Furthermore, because of symmetry on the Clebsch-Gordan coefficients, we have $n_0^{\pm 2} = n_0^2$ and $n_0^{\pm 1} = n_0^1$; thus, $n'_0 = 2(n_0^2 + 10n_0^1 + 10n_0^0)$.

Finally, by using Eq. A.12 and making $y' = 2\mathcal{E}/\kappa$ results in

$$y' = (1 - i\Delta')\mathrm{X}' + \frac{\Gamma b}{2\kappa}(1 + i\delta'_p)\mathrm{X}'N \sum_{m=-2}^{+2} \mathcal{P}''_m \tag{A.28}$$

where $\Delta' = 2\Delta/\kappa$. This can be solved by noting that

$$\sum_{m=-2}^{+2} \mathcal{P}''_m = 42\mathrm{v} = \frac{1}{(\bar{n}_0(1+\delta_p'^2) + b\,|\mathrm{X}'|^2)}. \tag{A.29}$$

where $\bar{n}_0 = (n_0^2 + 10n_0^1 + 10n_0^0)/21$ is the average of the saturation photon number over the population probability distribution of an atom in steady-state after optical pumping. Eq. A.28 can be rewritten as

$$y = \left((1 - i\Delta') + 2\bar{\mathrm{C}}_1 N \frac{1 + i\delta'_p}{1 + \delta_p'^2 + b\,|\mathrm{x}|^2} \right) x \tag{A.30}$$

where $y = 2\mathcal{E}/\kappa\sqrt{\bar{n}_0}$, $x = \langle \hat{a} \rangle / \sqrt{\bar{n}_0}$ and $\bar{\mathrm{C}}_1 = \frac{2\bar{g}_0^2}{\kappa\Gamma}$ with $\bar{g}_0^2 = \frac{\Gamma^2}{8\bar{n}_0} b$. Then, comparing this result with the one obtained in [52] it can be concluded that the inclusion of multilevel atoms results in an average or effective value of C_1.

A.3. Optical pumping in the cavity mode

These equations were derived in order to explain the observations when the cavity is probed at a constant detuning (e.g. $\Delta_p = 24.5$ MHz) at the outer slope of one of the normal mode peaks. Based on the discussion of Ch. 2 a constant cavity transmission is expected. However, the observed behavior is shown in Fig. A.2: the cavity transmission grows in a short timescale; then, it decreases after some ms.

The latter observation is argued to be a consequence of the atom cloud falling due to gravity and growing due to thermal expansion. These, in particular, are considered as atom loss from the cavity mode. Indeed, because the normal mode splitting depends on the atom number it is expected that as atoms leave the cavity mode, the normal mode peaks get closer to each other. This happens until the transmission spectrum shows only a single peak corresponding to an empty cavity. The change of transmitted light due to atom loss in a cavity has been published in Ref. [84] where two different timescales were also observed corresponding to axial and radial expansion of the atomic cloud.

Here, though, the growth of transmitted light at $\Delta_p = 24.5$ MHz cannot be explained as atom loss. Indeed, this growth would correspond to an increase of

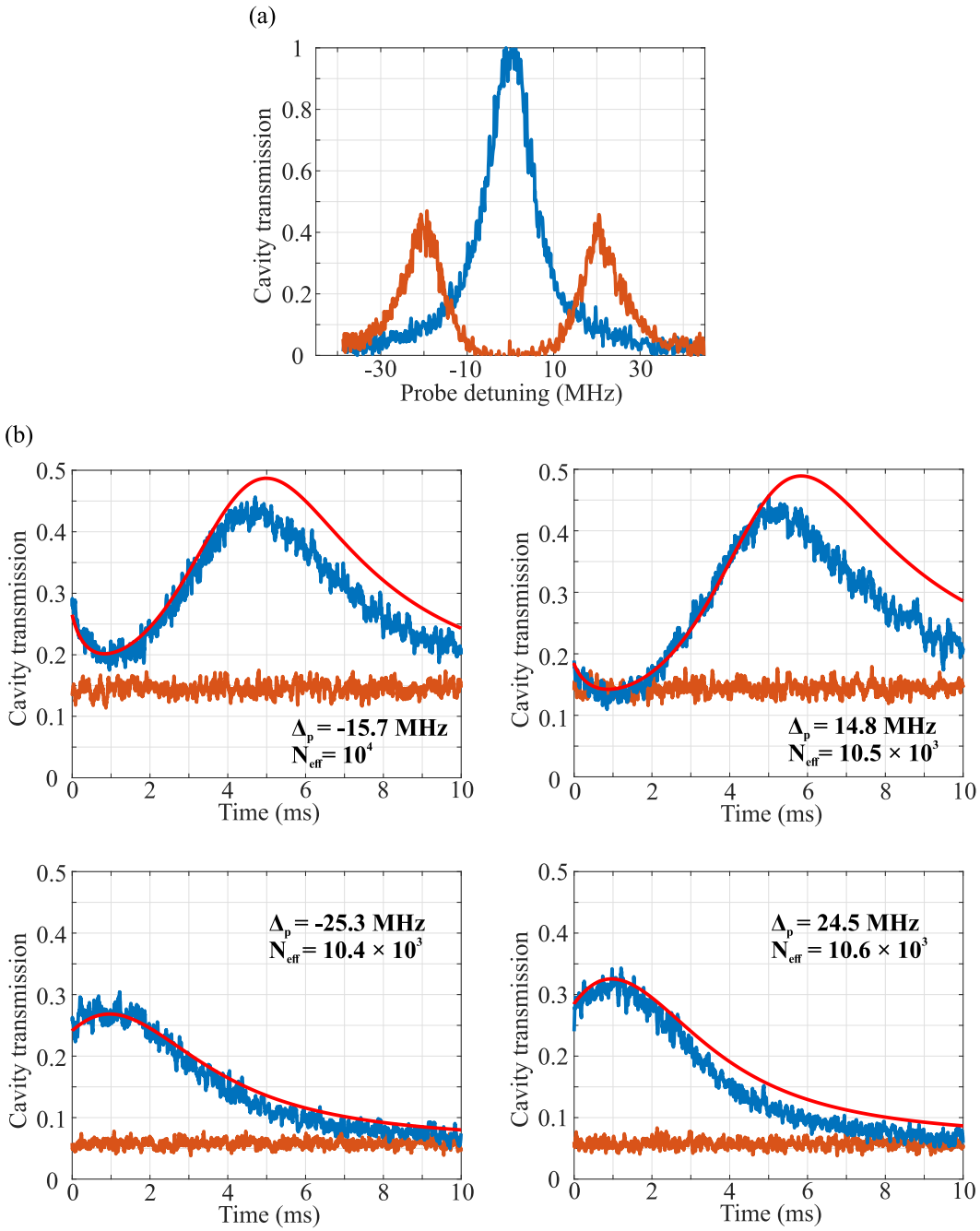

Figure A.2.: (a) Transmission spectrum corresponding to the measurements in (b). From here the number of atoms is estimated to be $N_{eff} = (10.4 \pm 0.4) \times 10^3$, the cavity detuning $\Delta_c = -2\pi \cdot 0.2 \pm 0.4$ MHz and linewidth $\kappa = 2\pi \cdot 13.4 \pm 0.6$ MHz. (b) Cavity transmission for different constant Δ_p: with atoms (blue) and without atoms (orange) inside the cavity. Based on the measured transmitted power, the peak intracavity optical power is 2.7 nW ($\eta = 2\pi \cdot 12.4$ MHz). The red lines correspond to a least-square fit optimizing N_{eff} while $w_0 = 310$ μm, $\Delta_c = 0$ MHz, $\kappa = 2\pi \cdot 13.2$ MHz and $T = 30$ μK are kept fixed.

Ω_{NM}: the normal mode peaks are getting farther away from each other. However, since care has been taken to hit the atom cloud at the center where the density is largest, there is no reason to believe that the atom number should increase. On the contrary, it should always decrease. Furthermore, the number of intracavity photons is low enough ($n_{ph} \sim 2$); thus, radiation force and/or the atomic external degrees of freedom should not play a role in these measurements.

It is the atomic internal degrees of freedom then that must be analyzed in more detail. In this context, a first approach taken in this thesis is to account the interaction of all Zeeman states with the same cavity mode. This has an effect on Ω_{NM} by means of the Clebsch-Gordan coefficients. Indeed, as concluded in this appendix, the steady-state of this multilevel atom-cavity system is characterized by an average coupling coefficient $\bar{g_0}$ over the final ground state probability distribution; thus, there is an interdependence between atomic ground state population and intracavity field via Ω_{NM}. In the present case the initial ground state probability distribution is considered to be homogeneous as it is taken after the MOT preparation. Then, the linearly polarized intracavity field drives π-transitions on the atoms aligning them towards the $m_F = 0$ Zeeman state: the one with highest Clebsch-Gordan coefficient. The new $\bar{g_0}$ is then larger than the initial one and the evolution of Ω_{NM} towards its final value generates the observed behavior in Fig. A.2 where other values of δ_p are also considered. In fact, it is shown in [96] that π-transitions always lead to an exponential evolution of a Zeeman state population while $\sigma^{\pm}$-transitions lead to non-exponential dynamics.

Finally, the set of differential equations derived in Sec. A.1.2 are used to obtain the solid red lines shown in Fig. A.2. In addition, the change of atom number due to ballistic expansion and gravity is accounted by doing

$$N(t) = N(t=0)\frac{w^2}{w^2 + (V_{th}t)^2} e^{-\frac{(0.5gt)^2}{2(w^2+(V_{th}t)^2)}}. \tag{A.31}$$

Here, $V_{th} = \sqrt{\frac{k_B T}{M}}$ is the thermal velocity for an atom of temperature T and mass M while g is the gravity acceleration.

B. LBO thermal response

At a steady state any material can be associated with a thermal resistance $R_{\text{th}} = \ell/\lambda A$ where ℓ is the length on the direction of the heat flow, A is the cross-sectional area and λ is the thermal conductivity. However, when it is an out-of-equilibrium situation there is an associated capacitance C_{th}:

$$C_{\text{th}} = \rho V C_p \tag{B.1}$$

with material density ρ, volume V and specific heat C_p. Sectioning the material into different layers corresponds to several low-pass RC filters.

Considering the specific heat of LBO to be 1060 $J/Kg{\cdot}K$, its density of 2.47 g/cm^3 and thermal conductivity of 3.5 $W/m \cdot K$ a time constant $RC = 6.6$ s is obtained.

C. Decay rate matrix

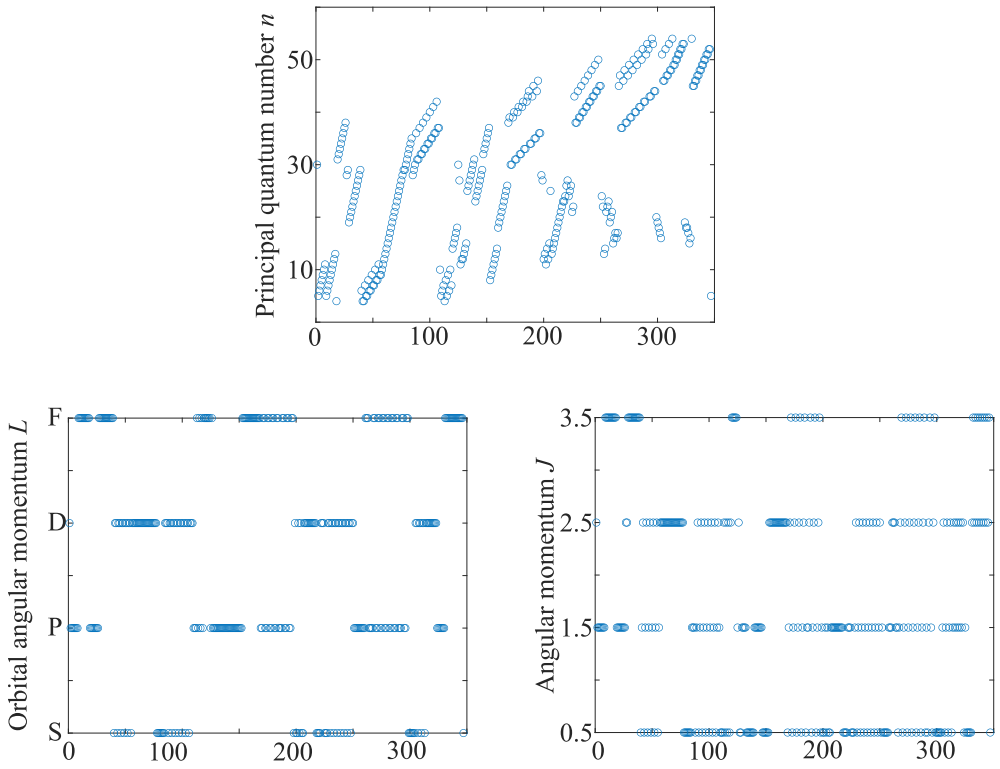

Figure C.1.: The quantum numbers for the states used in the decay matrix used in the numerical simulation of Sec. 4: principal quantum number n, orbital angular momentum L and angular momentum J.

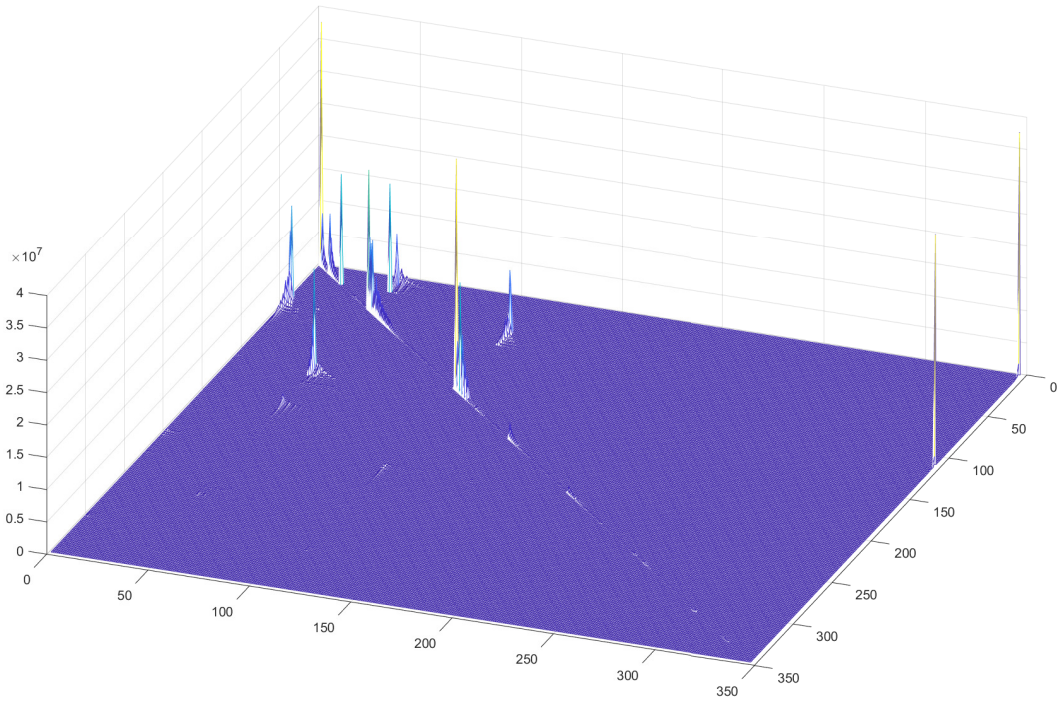

Figure C.2.: The decay matrix used in simulations of Sec. 4 to describe the decay dynamics from the $30D_{5/2}$ state including BBR are shown in the lower figure. The vertical axis is in Hz and the horizontal axis are indexes that correspond to an electronic state of principal quantum number n, orbital angular momentum L and angular momentum J. These states are displayed in Fig. C.1

D. List of Figures

E. Bibliography

[1] R. P. Feynman, R. B. Leighton, and M. Sands, *The Feynman lectures on physics; New millennium ed.* New York, NY: Basic Books, 2010. Originally published 1963-1965.

[2] W. H. Zurek, "From quantum to classical," *Phys Today*, vol. 37, 1991.

[3] D. J. Wineland, "Nobel Lecture: Superposition, entanglement, and raising Schrödinger's cat," *Rev. Mod. Phys.*, vol. 85, pp. 1103–1114, Jul 2013.

[4] S. Haroche, "Nobel Lecture: Controlling photons in a box and exploring the quantum to classical boundary," *Rev. Mod. Phys.*, vol. 85, pp. 1083–1102, Jul 2013.

[5] J.-S. Xu, X.-Y. Xu, C.-F. Li, C.-J. Zhang, X.-B. Zou, and G.-C. Guo, "Experimental investigation of classical and quantum correlations under decoherence," *Nature communications*, vol. 1, no. 1, pp. 1–6, 2010.

[6] H. D. Zeh, "On the interpretation of measurement in quantum theory," *Foundations of Physics*, vol. 1, no. 1, pp. 69–76, 1970.

[7] M. Schlosshauer, "Quantum decoherence," *Physics Reports*, vol. 831, pp. 1–57, 2019. Quantum decoherence.

[8] F. Hasselbach, H. Kiesel, and P. Sonnentag, "Exploration of the Fundamentals of Quantum Mechanics by Charged Particle Interferometry," in *Decoherence: Theoretical, Experimental, and Conceptual Problems*, pp. 201–212, Springer, 2000.

[9] C. Jönsson, "Elektroneninterferenzen an mehreren künstlich hergestellten Feinspalten," *Zeitschrift für Physik*, vol. 161, no. 4, pp. 454–474, 1961.

[10] A. Rembold, G. Schütz, R. Röpke, W.-T. Chang, I.-S. Hwang, A. Günther, and A. Stibor, "Vibrational dephasing in matter-wave interferometers," *New Journal of Physics*, vol. 19, no. 3, p. 033009, 2017.

[11] N. Kerker, R. Röpke, L.-M. Steinert, A. Pooch, and A. Stibor, "Quantum decoherence by Coulomb interaction," *New Journal of Physics*, vol. 22, no. 6, p. 063039, 2020.

[12] M. Gross, P. Goy, C. Fabre, S. Haroche, and J. M. Raimond, "Maser Oscillation and Microwave Superradiance in Small Systems of Rydberg Atoms," *Phys. Rev. Lett.*, vol. 43, pp. 343–346, Jul 1979.

[13] J. M. Raimond, P. Goy, M. Gross, C. Fabre, and S. Haroche, "Statistics of Millimeter-Wave Photons Emitted by a Rydberg-Atom Maser: An Experimental Study of Fluctuations in Single-Mode Superradiance," *Phys. Rev. Lett.*, vol. 49, pp. 1924–1927, Dec 1982.

[14] R. H. Dicke, "Coherence in Spontaneous Radiation Processes," *Phys. Rev.*, vol. 93, pp. 99–110, Jan 1954.

[15] R. Bonifacio, P. Schwendimann, and F. Haake, "Quantum Statistical Theory of Superradiance. I," *Phys. Rev. A*, vol. 4, pp. 302–313, Jul 1971.

[16] T. Laurent, Y. Todorov, A. Vasanelli, A. Delteil, C. Sirtori, I. Sagnes, and G. Beaudoin, "Superradiant Emission from a Collective Excitation in a Semiconductor," *Phys. Rev. Lett.*, vol. 115, p. 187402, Oct 2015.

[17] A. Angerer, K. Streltsov, T. Astner, S. Putz, H. Sumiya, S. Onoda, J. Isoya, W. J. Munro, K. Nemoto, J. Schmiedmayer, *et al.*, "Superradiant emission from colour centres in diamond," *Nature Physics*, vol. 14, no. 12, pp. 1168–1172, 2018.

[18] G.-D. Lin and S. F. Yelin, "Vibrational spectroscopy of polar molecules with superradiance," *Molecular Physics*, vol. 111, no. 12-13, pp. 1917–1922, 2013.

[19] F. Rajabi and M. Houde, "Dicke's superradiance in astrophysics. i. the 21 cm line," *The Astrophysical Journal*, vol. 826, p. 216, aug 2016.

[20] M. A. Norcia, M. N. Winchester, J. R. K. Cline, and J. K. Thompson, "Superradiance on the millihertz linewidth strontium clock transition," *Science Advances*, vol. 2, no. 10, p. e1601231, 2016.

[21] P. Weiss, A. Cipris, R. Kaiser, I. M. Sokolov, and W. Guerin, "Superradiance as single scattering embedded in an effective medium," *Phys. Rev. A*, vol. 103, p. 023702, Feb 2021.

[22] Y. Yoshikawa, Y. Torii, and T. Kuga, "Superradiant Light Scattering from Thermal Atomic Vapors," *Phys. Rev. Lett.*, vol. 94, p. 083602, Mar 2005.

[23] P. Weiss, A. Cipris, M. O. Araújo, R. Kaiser, and W. Guerin, "Robustness of Dicke subradiance against thermal decoherence," *Phys. Rev. A*, vol. 100, p. 033833, Sep 2019.

[24] S. Slama, G. Krenz, S. Bux, C. Zimmermann, and P. W. Courteille, "Cavity-enhanced superradiant Rayleigh scattering with ultracold and Bose-Einstein condensed atoms," *Phys. Rev. A*, vol. 75, p. 063620, Jun 2007.

[25] D. Braun, J. Hoffman, and E. Tiesinga, "Superradiance of cold atoms coupled to a superconducting circuit," *Phys. Rev. A*, vol. 83, p. 062305, Jun 2011.

[26] M. Gross and S. Haroche, "Superradiance: An essay on the theory of collective spontaneous emission," *Physics Reports*, vol. 93, no. 5, pp. 301–396, 1982.

[27] R. T. Sutherland and F. Robicheaux, "Superradiance in inverted multilevel atomic clouds," *Phys. Rev. A*, vol. 95, p. 033839, Mar 2017.

[28] T. Wang, S. F. Yelin, R. Côté, E. E. Eyler, S. M. Farooqi, P. L. Gould, M. Koštrun, D. Tong, and D. Vrinceanu, "Superradiance in ultracold Rydberg gases," *Phys. Rev. A*, vol. 75, p. 033802, Mar 2007.

[29] T. Zhou, B. G. Richards, and R. R. Jones, "Absence of collective decay in a cold Rydberg gas," *Phys. Rev. A*, vol. 93, p. 033407, Mar 2016.

[30] L. Mandel and E. Wolf, *Optical Coherence and Quantum Optics*. Cambridge University Press, 1995.

[31] L. Allen and J. H. Eberly, *Optical resonance and two-level atoms*. Dover Publ., 1975.

[32] H.-P. Breuer and F. Petrucione, *The theory of Open Quantum Systems*. Clarendon Press, 2010.

[33] S. Haroche and J.-M. Raimond, *Exploring the quantum: Atoms, Cavities, and Photons*. Oxford University Press, 2019.

[34] J. D. Jackson, *Classical Electrodynamics*. John Wiley & Sons, 3rd ed., 1999.

[35] J. Gea-Banacloche, Y.-q. Li, S.-z. Jin, and M. Xiao, "Electromagnetically induced transparency in ladder-type inhomogeneously broadened media: Theory and experiment," *Phys. Rev. A*, vol. 51, pp. 576–584, Jan 1995.

[36] E. Brion, L. H. Pedersen, and K. Mølmer, "Adiabatic elimination in a lambda system," *Journal of Physics A: Mathematical and Theoretical*, vol. 40, pp. 1033–1043, Jan 2007.

[37] M. Fleischhauer, A. Imamoglu, and J. P. Marangos, "Electromagnetically induced transparency: Optics in coherent media," *Rev. Mod. Phys.*, vol. 77, pp. 633–673, Jul 2005.

[38] A. Imamoğlu and S. E. Harris, "Lasers without inversion: interference of dressed lifetime-broadened states," *Opt. Lett.*, vol. 14, pp. 1344–1346, Dec 1989.

[39] E. Arimondo, "V Coherent Population Trapping in Laser Spectroscopy," vol. 35 of *Progress in Optics*, pp. 257–354, Elsevier, 1996.

[40] K.-J. Boller, A. Imamoğlu, and S. E. Harris, "Observation of electromagnetically induced transparency," *Phys. Rev. Lett.*, vol. 66, pp. 2593–2596, May 1991.

[41] K. Bergmann, H. Theuer, and B. W. Shore, "Coherent population transfer among quantum states of atoms and molecules," *Rev. Mod. Phys.*, vol. 70, pp. 1003–1025, Jul 1998.

[42] A. V. Gorshkov, A. André, M. D. Lukin, and A. S. Sørensen, "Photon storage in Λ-type optically dense atomic media. I. Cavity model," *Phys. Rev. A*, vol. 76, p. 033804, Sep 2007.

[43] K. Xia and J. Evers, "Ground State Cooling of a Nanomechanical Resonator in the Nonresolved Regime via Quantum Interference," *Phys. Rev. Lett.*, vol. 103, p. 227203, Nov 2009.

[44] M. D. Eisaman, A. André, F. Massou, M. Fleischhauer, A. S. Zibrov, and M. D. Lukin, "Electromagnetically induced transparency with tunable single-photon pulses," *Nature*, vol. 438, no. 7069, pp. 837–841, 2005.

[45] Y.-H. Chen, M.-J. Lee, W. Hung, Y.-C. Chen, Y.-F. Chen, and I. A. Yu, "Demonstration of the Interaction between Two Stopped Light Pulses," *Phys. Rev. Lett.*, vol. 108, p. 173603, Apr 2012.

[46] M. D. Lukin and A. Imamoğlu, "Nonlinear Optics and Quantum Entanglement of Ultraslow Single Photons," *Phys. Rev. Lett.*, vol. 84, pp. 1419–1422, Feb 2000.

[47] X. Lu, X. Miao, J. Bai, L. Pei, M. Wang, Y. Gao, L.-A. Wu, P. Fu, R. Wang, and Z. Zuo, "Transition from Autler–Townes splitting to electromagnetically induced transparency based on the dynamics of decaying dressed states," *Journal of Physics B: Atomic, Molecular and Optical Physics*, vol. 48, p. 055003, feb 2015.

[48] C. Cohen-Tannoudji, J. Dupont-Roc, and G. Grynberg, *Photons and atoms: Introduction to quantum electrodynamics*. John Wiley & Sons, 1997.

[49] E. Jaynes and F. Cummings, "Comparison of quantum and semiclassical radiation theories with application to the beam maser," *Proceedings of the IEEE*, vol. 51, no. 1, pp. 89–109, 1963.

[50] H. Kogelnik and T. Li, "Laser Beams and Resonators," *Appl. Opt.*, vol. 5, pp. 1550–1567, Oct 1966.

[51] Y. Colombe, T. Steinmetz, G. Dubois, F. Linke, D. Hunger, and J. Reichel, "Strong atom–field coupling for Bose–Einstein condensates in an optical cavity on a chip," *Nature*, vol. 450, no. 7167, pp. 272–276, 2007.

[52] J. Gripp, S. L. Mielke, and L. A. Orozco, "Evolution of the vacuum Rabi peaks in a detuned atom-cavity system," *Phys. Rev. A*, vol. 56, pp. 3262–3273, Oct 1997.

[53] J. Sheng, Y. Chao, S. Kumar, H. Fan, J. Sedlacek, and J. P. Shaffer, "Intracavity Rydberg-atom electromagnetically induced transparency using a high-finesse optical cavity," *Phys. Rev. A*, vol. 96, p. 033813, Sep 2017.

[54] Y. Zhu, D. J. Gauthier, S. E. Morin, Q. Wu, H. J. Carmichael, and T. W. Mossberg, "Vacuum Rabi splitting as a feature of linear-dispersion theory: Analysis and experimental observations," *Phys. Rev. Lett.*, vol. 64, pp. 2499–2502, May 1990.

[55] J. Gripp and L. A. Orozco, "Evolution of the vacuum Rabi peaks in a many-atom system," *Quantum and Semiclassical Optics: Journal of the European Optical Society Part B*, vol. 8, pp. 823–836, aug 1996.

[56] M. D. Lukin, M. Fleischhauer, M. O. Scully, and V. L. Velichansky, "Intracavity electromagnetically induced transparency," *Opt. Lett.*, vol. 23, pp. 295–297, Feb 1998.

[57] J. Sheng, H. Wu, M. Mumba, J. Gea-Banacloche, and M. Xiao, "Understanding cavity resonances with intracavity dispersion properties," *Physical Review A*, vol. 83, no. 2, p. 023829, 2011.

[58] J. Ningyuan, A. Georgakopoulos, A. Ryou, N. Schine, A. Sommer, and J. Simon, "Observation and characterization of cavity Rydberg polaritons," *Phys. Rev. A*, vol. 93, p. 041802, Apr 2016.

[59] M. Reitz, C. Sommer, and C. Genes, "Cooperative Quantum Phenomena in Light-Matter Platforms," *PRX Quantum*, vol. 3, p. 010201, Jan 2022.

[60] N. E. Rehler and J. H. Eberly, "Superradiance," *Phys. Rev. A*, vol. 3, pp. 1735–1751, May 1971.

[61] T. F. Gallagher, *Rydberg Atoms*. Cambridge Monographs on Atomic, Molecular and Chemical Physics, Cambridge University Press, 1994.

[62] N. Šibalić, J. Pritchard, C. Adams, and K. Weatherill, "ARC: An open-source library for calculating properties of alkali Rydberg atoms," *Computer Physics Communications*, vol. 220, pp. 319–331, 2017.

[63] L. Moi, P. Goy, M. Gross, J. M. Raimond, C. Fabre, and S. Haroche, "Rydberg-atom masers. I. A theoretical and experimental study of super-radiant systems in the millimeter-wave domain," *Phys. Rev. A*, vol. 27, pp. 2043–2064, Apr 1983.

[64] M. Saffman, T. G. Walker, and K. Mølmer, "Quantum information with Rydberg atoms," *Rev. Mod. Phys.*, vol. 82, pp. 2313–2363, Aug 2010.

[65] S. Ravets, H. Labuhn, D. Barredo, L. Béguin, T. Lahaye, and A. Browaeys, "Coherent dipole–dipole coupling between two single Rydberg atoms at an electrically-tuned Förster resonance," *Nature Physics*, vol. 10, no. 12, pp. 914–917, 2014.

[66] R. Friedberg, S. Hartmann, and J. Manassah, "Frequency shifts in resonant systems," *Physics Letters A*, vol. 35, no. 3, pp. 161–162, 1971.

[67] J. Pellegrino, R. Bourgain, S. Jennewein, Y. R. P. Sortais, A. Browaeys, S. D. Jenkins, and J. Ruostekoski, "Observation of Suppression of Light Scattering Induced by Dipole-Dipole Interactions in a Cold-Atom Ensemble," *Phys. Rev. Lett.*, vol. 113, p. 133602, Sep 2014.

[68] J. Javanainen and J. Ruostekoski, "Light propagation beyond the mean-field theory of standard optics," *Opt. Express*, vol. 24, pp. 993–1001, Jan 2016.

[69] S. D. Jenkins, J. Ruostekoski, J. Javanainen, R. Bourgain, S. Jennewein, Y. R. P. Sortais, and A. Browaeys, "Optical Resonance Shifts in the Fluorescence of Thermal and Cold Atomic Gases," *Phys. Rev. Lett.*, vol. 116, p. 183601, May 2016.

[70] E. A. Goldschmidt, T. Boulier, R. C. Brown, S. B. Koller, J. T. Young, A. V. Gorshkov, S. L. Rolston, and J. V. Porto, "Anomalous Broadening in Driven Dissipative Rydberg Systems," *Phys. Rev. Lett.*, vol. 116, p. 113001, Mar 2016.

[71] T. Boulier, E. Magnan, C. Bracamontes, J. Maslek, E. A. Goldschmidt, J. T. Young, A. V. Gorshkov, S. L. Rolston, and J. V. Porto, "Spontaneous avalanche dephasing in large Rydberg ensembles," *Phys. Rev. A*, vol. 96, p. 053409, Nov 2017.

[72] B. Coffey and R. Friedberg, "Effect of short-range Coulomb interaction on cooperative spontaneous emission," *Phys. Rev. A*, vol. 17, pp. 1033–1048, Mar 1978.

[73] F. Damanet and J. Martin, "Competition between finite-size effects and dipole–dipole interactions in few-atom systems," *Journal of Physics B: Atomic, Molecular and Optical Physics*, vol. 49, p. 225501, oct 2016.

[74] H. Carmichael and K. Kim, "A quantum trajectory unraveling of the superradiance master equation," *Optics Communications*, vol. 179, no. 1, pp. 417–427, 2000.

[75] R. Wiegner, J. von Zanthier, and G. S. Agarwal, "Quantum-interference-initiated superradiant and subradiant emission from entangled atoms," *Phys. Rev. A*, vol. 84, p. 023805, Aug 2011.

[76] F. C. Spano and S. Mukamel, "Superradiance in molecular aggregates," *The Journal of Chemical Physics*, vol. 91, no. 2, pp. 683–700, 1989.

[77] D. Nikogosyan, "Lithium triborate (LBO)," *Applied Physics A*, vol. 58, no. 3, pp. 181–190, 1994.

[78] S. Velsko, M. Webb, L. Davis, and C. Huang, "Phase-matched harmonic generation in lithium triborate (LBO)," *IEEE Journal of Quantum Electronics*, vol. 27, no. 9, pp. 2182–2192, 1991.

[79] D. A. Kleinman, A. Ashkin, and G. D. Boyd, "Second-Harmonic Generation of Light by Focused Laser Beams," *Phys. Rev.*, vol. 145, pp. 338–379, May 1966.

[80] T. Freegarde and C. Zimmermann, "On the design of enhancement cavities for second harmonic generation," *Optics Communications*, vol. 199, no. 5, pp. 435–446, 2001.

[81] G. Boyd and D. Kleinman, "Parametric interaction of focused Gaussian light beams," *Journal of Applied Physics*, vol. 39, no. 8, pp. 3597–3639, 1968.

[82] T. Carmon, L. Yang, and K. J. Vahala, "Dynamical thermal behavior and thermal self-stability of microcavities," *Opt. Express*, vol. 12, pp. 4742–4750, Oct 2004.

[83] M. Mack, F. Karlewski, H. Hattermann, S. Höckh, F. Jessen, D. Cano, and J. Fortágh, "Measurement of absolute transition frequencies of ^{87}Rb to nS and nD Rydberg states by means of electromagnetically induced transparency," *Phys. Rev. A*, vol. 83, p. 052515, May 2011.

[84] R. D. Niederriter, C. Schlupf, and P. Hamilton, "Cavity probe for real-time detection of atom dynamics in an optical lattice," *Phys. Rev. A*, vol. 102, p. 051301, Nov 2020.

[85] J. Zeiher, J. Wolf, J. A. Isaacs, J. Kohler, and D. M. Stamper-Kurn, "Tracking Evaporative Cooling of a Mesoscopic Atomic Quantum Gas in Real Time," *Phys. Rev. X*, vol. 11, p. 041017, Oct 2021.

[86] T. W. Clark, A. Dombi, F. I. B. Williams, A. Kurkó, J. Fortágh, D. Nagy, A. Vukics, and P. Domokos, "Time-resolved observation of a dynamical phase transition with atoms in a cavity," *Phys. Rev. A*, vol. 105, p. 063712, Jun 2022.

[87] B. Huber, T. Baluktsian, M. Schlagmüller, A. Kölle, H. Kübler, R. Löw, and T. Pfau, "GHz Rabi Flopping to Rydberg States in Hot Atomic Vapor Cells," *Phys. Rev. Lett.*, vol. 107, p. 243001, Dec 2011.

[88] T. Baluktsian, B. Huber, R. Löw, and T. Pfau, "Evidence for Strong van der Waals Type Rydberg-Rydberg Interaction in a Thermal Vapor," *Phys. Rev. Lett.*, vol. 110, p. 123001, Mar 2013.

[89] V. V. Temnov and U. Woggon, "Superradiance and Subradiance in an Inhomogeneously Broadened Ensemble of Two-Level Systems Coupled to a Low-Q Cavity," *Phys. Rev. Lett.*, vol. 95, p. 243602, Dec 2005.

[90] G. S. Agarwal, "Master-Equation Approach to Spontaneous Emission. III. Many-Body Aspects of Emission from Two-Level Atoms and the Effect of Inhomogeneous Broadening," *Phys. Rev. A*, vol. 4, pp. 1791–1801, Nov 1971.

[91] R. Jodoin and L. Mandel, "Superradiance in an inhomogeneously broadened atomic system," *Phys. Rev. A*, vol. 9, pp. 873–884, Feb 1974.

[92] E. Suarez, P. Wolf, P. Weiss, and S. Slama, "Superradiance decoherence caused by long-range Rydberg-atom pair interactions," *Phys. Rev. A*, vol. 105, p. L041302, Apr 2022.

[93] K. Baumann, C. Guerlin, F. Brennecke, and T. Esslinger, "Dicke quantum phase transition with a superfluid gas in an optical cavity," *Nature*, vol. 464, no. 7293, pp. 1301–1306, 2010.

[94] A. Piñeiro Orioli, J. K. Thompson, and A. M. Rey, "Emergent Dark States from Superradiant Dynamics in Multilevel Atoms in a Cavity," *Phys. Rev. X*, vol. 12, p. 011054, Mar 2022.

[95] F. Atoneche and A. Kastberg, "Simplified approach for quantitative calculations of optical pumping," *European Journal of Physics*, vol. 38, p. 045703, may 2017.

[96] E. Suarez, F. Carollo, I. Lesanovsky, B. Olmos, P. W. Courteille, and S. Slama, "Collective atom-cavity coupling and nonlinear dynamics with atoms with multilevel ground states," *Phys. Rev. A*, vol. 107, p. 023714, Feb 2023.

Acknowledgments

I would like to give my greatest gratitude to Prof. Claus Zimmermann for giving me the opportunity, in the first place, to come to Tübingen. At the same time, I thank Prof. Sebastian Slama for offering me to be part of his group as a PhD student. I am also grateful with all other students from the other groups that helped or gave me advice when I needed it. In this regard, a special thank you to Patrizia Weiss and Philip Wolf who worked in the lab at the beggining of this project and allowed me to learn from their greater and valuable experience. Finally, to the people at the electronic and mechanical workshop who introduced me to their crafts when I first started.

Besides work, I would like to thank those special people in or outside of Tübingen who were important to me during the realization of this project.